DISSERTATION

CURRENT DISTRIBUTION AND PARTICLE MOTION IN A BARBED PLATE ELECTROSTATIC PRECIPITATOR

Submitted by

Peter J. McKinney

Department of Civil Engineering

In partial fulfillment of the requirements

for the Degree of Doctor of Philosophy

Colorado State University

Fort Collins, Colorado

Fall 1993

COLORADO STATE UNIVERSITY

August 5, 1993

WE HEREBY RECOMMEND THAT THE DISSERTATION PREPARED UNDER OUR SUPERVISION BY PETER J. MCKINNEY ENTITLED CURRENT DISTRIBUTION AND PARTICLE MOTION IN A BARBED PLATE ELECTROSTATIC PRECIPITATOR BE ACCEPTED AS FULFILLING IN PART REQUIREMENTS FOR THE DEGREE OF DOCTOR OF PHILOSOPHY.

Committee on Graduate Work

Adviser

Department Head

ABSTRACT OF DISSERTATION

CURRENT DISTRIBUTION AND PARTICLE MOTION IN A BARBED PLATE ELECTROSTATIC PRECIPITATOR

Electrohydrodynamic theory suggests that a modification in electrode geometry is a method of creating more favorable electrical and flow conditions in electrostatic precipitators. A novel barbed plate precipitator is designed to provide a more uniform current density distribution and electric field in the inter-electrode gap. Ground plate current densities of both a conventional wire-plate precipitator and the optimized barbed plate precipitator are compared. Particle motion is observed via a laser light-sheet and measured with a laser Doppler anemometer. Streamwise and transverse mean and fluctuating particle velocities, particle motion length scales and diffusivities are measured at electrical and flow conditions typical of industrial precipitators. Ground plate particle collection patterns are photographed.

Results show a hexagonal arrangement of barbs provides a more uniform current density distribution and electric field than exist in the wire-plate geometry. Additionally, the barbed plate creates a stronger electric field throughout most of the inter-electrode space and therefore generates higher particle drift velocities. However, the barbed plate increases the magnitude of the electrically generated turbulence. Length scales are of the

same order in the two geometries even though the electrode spacing of the barbed plate is double that of the wire-plate precipitator.

From an electrical standpoint, the barbed plate design is superior to the wire-plate precipitator. The more uniform distribution of current and electric field coupled with higher levels of mixing suggest the barbed plate may be most suitable for use as a precharger in the entrance section of a parallel plate precipitator.

Peter J. McKinney
Civil Engineering Department
Colorado State University
Fort Collins, Colorado 80523
Fall 1993

ACKNOWLEDGEMENTS

I would like to thank Dr. Jane Davidson for her guidance, patience, and support over the duration of time it took me to complete this dissertation. I am fortunate to have had such a dedicated advisor. Thanks are also due to Drs. Gessler, Meroney, and Wilbur for their thoughtful comments and suggestions. I would like to thank my father, John, and my mother, Madeleine, for their encouragement during all of my years in school. Without your example I would never have been able to realize my goal - thank you! I am also indebted to my siblings, Martin, Maureen, and Elizabeth - the diversity of your interests continues to spark new interests within me. Finally, the support of the Environmental Protection Agency through grant number R-815740-01 is gratefully acknowledged.

TABLE OF CONTENTS

TABLE OF CONTENTS (cont.)

LIST OF TABLES

LIST OF FIGURES

LIST OF FIGURES (cont.)

LIST OF FIGURES (cont.)

LIST OF FIGURES (cont.)

Page

LIST OF FIGURES (cont.)

LIST OF FIGURES (cont.)

LIST OF FIGURES (cont.)

LIST OF FIGURES (cont.)

LIST OF FIGURES (cont.)

Page

NOMENCLATURE

A	Total ground plane area (m)
CMD	Count median diameter (m)
C_c	Cunningham slip correction factor
d	Plate-to-plane spacing (m)
d_p	Particle diameter (m)
D	Particle diffusivity (m^2/s)
e	Fundamental unit of charge (1 electron = 1.6×10^{-19}C)
E	Magnitude of electric field (V/m)
$\mathbf{E}$	Electric field (V/m)
F_D	Stokes drag (N)
$\mathbf{F_e}$	Electric body force (N/m^3)
f'_d	Shifted Doppler frequency (Hz)
f_s	Total frequency shift (Hz)
I	Total current (A)
I%	Turbulence intensity (%)
k	Boltzman constant (1.38×10^{-23} J/°K-molecule)
J	Current density (A/m^2)
J_s	Saturation current density (A/m^2)
J_0	Centerline current density (A/m^2)

NOMENCLATURE (cont.)

ℓ	Barb length (m)
ℓ_x, ℓ_y	Integral length scale (m)
L	Barb tip-to-plane distance (m), wire-to-plate distance (m)
m	Exponent in Warburg distribution, maximum lag number
n_{in}	Number of particles into precipitator
n_{out}	Number of particles out of precipitator
N	Number of velocity measurements in time series
N_{EHD}	Dimensionless electric number ($Id/ßA\rho U^2$)
p	Gas pressure (N/m^2)
q_i	Ion charge (C)
q_p	Particle charge (C)
Q_V	Volumetric gas flow rate (m^3/s)
r	Barb tip radius (m), lag number
R	Radial distance from barb (m), autocorrelation coefficient
Re	Reynolds number, Equation 4.3
s	Barb spacing (m)
t	time (s)
T_A	Absolute temperature (^oK)
u, u_i	Eulerian particle velocity (m/s)
u'	Fluctuating Eulerian particle velocity (m/s)
u_{rms}, v_{rms}	Root-mean-square Eulerian particle velocity (m/s)
U	Mean Eulerian particle velocity (m/s)

NOMENCLATURE (cont.)

V	Applied voltage difference (V)
w_e	Effective electric particle migration velocity (m/s)
X,Y,Z	Coordinate directions (m)

Greek Symbols

β	Negative ion mobility (m/V-s)
β_p	particle mobility (m/V-s)
ε	relative dielectric constant of a particle
ε_0	Permittivity of free space (8.854×10^{-12} F/m)
λ	Laser wavelength (m), mean free path (m)
μ	Dynamic viscosity (N-s/m^2)
η	Fractional particle collection efficiency
ρ	Gas density (kg/m^3)
ρ_c	Ionic space charge (C/m^3)
ρ_p	Particulate space charge (C/m^3)
τ	Particle charging time constant
θ	Angle from the centerline (degrees), laser beam crossing angle (degrees)

CHAPTER 1.0

INTRODUCTION

The control and reduction of industrial air pollution has received a great deal of attention in recent years. The Clean Air Act Amendments of 1977 and 1990 provide the United States Environmental Protection Agency with the power to enforce new, more stringent regulations on pollutants such as sulfur oxides, nitrogen oxides, and Total Suspended Particulates (TSP). Particles of particular concern are those less than 10 μm in diameter (PM_{10}), which have the greatest effect on visibility, and particles less than 2.5 μm ($PM_{2.5}$), which have an adverse effect on human health. A major producer of particulate matter in both of these regimes is the coal-burning electric power industry.

At present, the two major technologies used to control particulate emissions of coal-fired burners are bag houses (basically sets of large fabric filters) and electrostatic precipitators (ESPs), which remove particles from the exhaust duct flow under the influence of an electric field. Both methods can have mass collection efficiencies greater than 99 percent. Although baghouses are very efficient at collecting particles of all sizes, once a "floc" has built up on the filter a substantial energy penalty is paid due to the flue gas head loss. Electrostatic precipitators, on the other hand, do not produce the large head loss, but have greater difficulty in collecting the particulate matter smaller than 1 μm in diameter. Because of their more effective collection of fine particulate matter, baghouses are the favored technology under the more stringent air quality standards. However, since electrostatic precipitators do not require large fans to overcome the large pressure drop, the Environmental Protection Agency is interested in ESP modification which may increase fine particle collection efficiency without increasing energy costs.

Ideally, improvement of conventional ESPs would not involve a dramatic redesign of the current hardware. Examination of the gas flow within the conventional wire-plate geometry suggests that improvement in gas flow conditions within the precipitator may enhance particle collection efficiency (Leonard *et al.*, 1980,1982; Larsen and Sorensen, 1984). Poor flow conditions are due in a large part to the electrohydrodynamic (EHD) wind which is a function of the electrode geometry (Leonard *et al.*, 1983; Shaughnessy *et al.*,1985; Davidson and Shaughnessy, 1986; Davidson and McKinney, 1989). A retrofit of the wire-plate geometry in which a barbed plate replaces the wires may improve precipitator performance by reducing turbulence diffusivities as well as corona current and electric field nonuniformities.

Although prior research has been performed on barbed plate geometries (McKinney 1988; Davidson and McKinney, 1989,1990,1991), there is no conclusive evidence that electrode modification alters particle collection efficiency. Earlier work is limited to hot-film measurements of the gas flow downstream of the electrodes, but suggests that the barbed plate reduces turbulent diffusivities. The barbed plate precipitator must be examined further to assess its practicality and effectiveness.

The purpose of this study is to determine particle velocities and collection efficiency for a barbed plate-to-plane precipitator operating in a 15.2 cm by 60.1 cm two-dimensional wind tunnel. Selection of the barbed plate electrode configuration is based on a preliminary optimization study of current distribution at the ground plane. Laser Doppler measurements of particle motion within the laboratory barbed plate-to-plane precipitator are compared to those made in a model wire-plate test section. Additional qualitative evaluation of flow within the precipitators is performed via laser light sheet flow visualization. Particle collection is discussed in terms of particle deposition patterns on the collector plates.

CHAPTER 2.0

MOTIVATION AND BACKGROUND

2.1 The Conventional Electrostatic Precipitator

The typical industrial electrostatic precipitator in use today is the wire-plate precipitator, sketched in Figure 2.1. The precipitator is operated by applying a high negative voltage to wires which are suspended midway between electrically grounded plates. Since the radius of curvature of each wire is very small compared to both the effective radius of curvature of the plates and the distance from the wires to the plates, the electric field strength near the wire is much greater than elsewhere in the inter-electrode gap and an electrical breakdown of the gas in the vicinity of the wires can occur without a complete sparkover to the grounded plates. This local ionization is known as corona discharge. In the case of a negative discharge, the corona appears as bluish glowing tufts on the wire. Industrial precipitators typically use negative corona because the sparkover voltage is much higher than that for positive corona.

The negative corona discharge is sustained by the ejection of free electrons from the wire surface to create electron avalanches. At the beginning of an avalanche, the electric field must be strong enough to accelerate a free electron (generated by cosmic or other radiation) to a velocity sufficiently high so that during a collision with a gas molecule, additional electrons are released. These free electrons move away from the

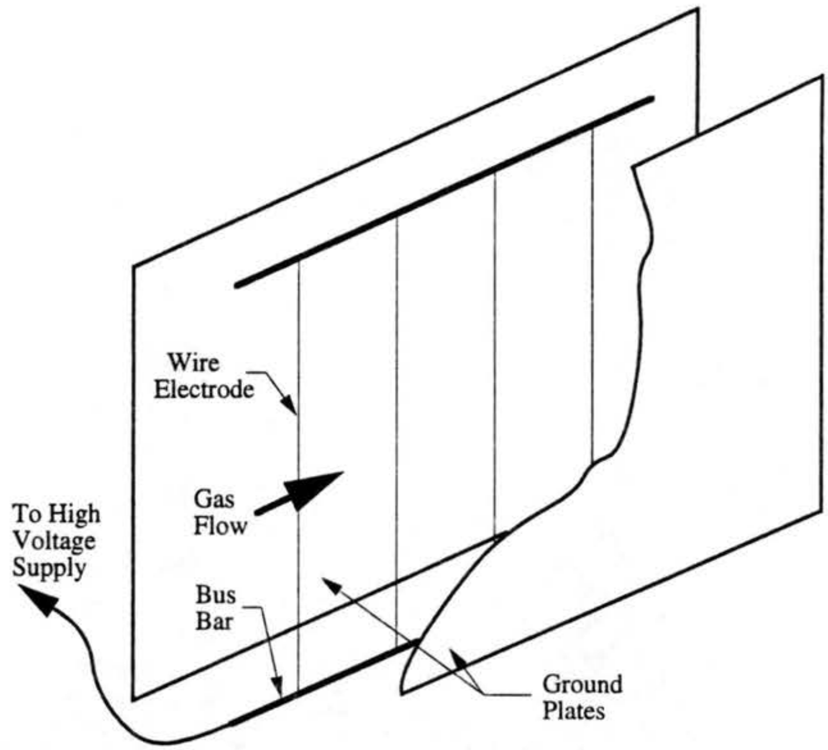

Figure 2.1. Conventional wire-plate precipitator schematic.

cathode toward the ground plane and create an "avalanche" of electrons as they strike additional gas molecules in the corona plasma. At a small distance from the wire surface, the strength of the electric field is reduced below the level necessary to support the avalanche. There, at the edge of the corona sheath, slower moving electrons attach to electronegative gas molecules (such as oxygen) and form ions which drift toward the ground plane, creating a monopolar space charge in the inter-electrode space. Positive ions formed in the plasma region are accelerated toward the cathode. Additional electrons are released as ions strike the wire and the discharge is sustained. The characteristic blue glow observed from a corona discharge in air is the result of molecules excited by collisions giving up energy as photon radiation.

Particle removal is accomplished by forcing the particle-laden gas between the plates. Particles collide with the negative ions moving along electric field lines and acquire a negative charge. After becoming charged, the particles also begin a migration to the ground plate. Mechanical hammers are commonly employed to "rap" the plates and remove the agglomerated particles which fall to hoppers located below the main flow channel. Typical physical parameters of modern industrial precipitators are listed in Table 2.1.

Table 2.1. Industrial electrostatic precipitator characteristics.

	Text Values*	General Electric**	Flakt**
Plate Spacing (cm)	20-38	23-31	30-40
Aspect Ratio (ht./wd.)	30-60	20-50	34-45
Wire Diameter (mm)	2.75-6.4	3-4.75	2.5
Wire Spacing (cm)	10-35	20-25	23
Gas Flow Rate (m/sec)	0.75-4.5	0.9-1.52	1.4
Current Density (mA/m^2)	0.1-1.0	0.05-0.3	0.5-0.7
Sparkover Voltage (kV)	40-65		
Temperature (°C)	100-480	138-166	149-204
Pressure (atm)	1	1	1
Operating Voltage (kV)	40-65	35-55	55-75

* Assimilated from White (1963), Oglesby and Nichols (1978), and McDonald and Dean (1982).

** Based on telephone conversation with the manufacturer.

General Electric Environmental Services, Inc. 200 N. 7th St., Lebanon, PA 17042

Flakt, Inc., Air Pollution Control Group P.O. Box 59018, Knoxville, TN 37950

2.2 Precipitator Efficiency

Traditionally, precipitator design has been based on the empirical Deutsch (1922) efficiency equation,

$$\eta = 1 - \exp\left(\frac{-Aw_e}{Q_V}\right) \tag{2.1}$$

in which η is fractional particle collection efficiency, Q_V is the volumetric gas flow rate, A is the total collection surface area, and w_e is the effective electric migration velocity of the particles ($w_e = \beta_p\mathbf{E}$ where β_p is the electrical mobility of the particle and $\mathbf{E}$ is the electric field). This equation assumes an infinite diffusivity, a single, constant particle migration velocity, a uniform electric field and velocity profile, and complete collection at the ground plate. These assumptions imply a monodisperse particle concentration and a uniform particle concentration profile transverse to the bulk flow. The other extreme is to assume that there is no mixing whatsoever and that laminar flow exists. In such a case, 100 percent efficiency could be achieved. In reality, flow within electrostatic precipitators is highly turbulent with a finite diffusivity resulting in collection efficiencies that can exceed the Deutsch prediction.

In an effort to provide a more realistic, physically-based description of the process taking place within the electrostatic precipitator, a large number of studies have been performed using the convective diffusion equation and a finite diffusivity. Utilizing a numerical solution, Feldman *et al.* (1977) concluded that as diffusive forces become large enough to cause particle migration on the order of the electrical migration, re-entrainment becomes significant, causing a loss in precipitator efficiency. Leonard *et al.* (1980) similarly concluded, through the use of an analytical solution to the diffusion equation, that reductions in gas flow turbulence could improve precipitator efficiency. Larsen and Sorensen (1984) extended the work of previous researchers by numerically imposing an axial roll on the bulk gas velocity in an attempt to imitate experimentally observed large scale secondary flows. They concluded that there is a decrease in precipitator efficiency with an increase in roll strength, even for an imposed diffusivity of zero.

It is apparent from these studies that a reduction in turbulent diffusion within the electrostatic precipitator may enhance particle collection efficiencies. This is particularly true for smaller particles that closely follow the gas motions and do not acquire as much charge. Although turbulence may enhance particle charging in the entrance region, Self *et al.* (1987,1988) conclude that the benefits of decreased turbulent mixing throughout the precipitator far outweigh those of enhanced charging at the inlet.

2.3 Electrohydrodynamic Turbulence

A major source of turbulence in electrostatic precipitators is the disruption of the bulk gas flow by the electric wind. It is well documented (as early as 1709 by Francis Hauksbee) that a corona discharge creates a corona "wind" due to momentum transfer from the ions to the neutral gas molecules. The strength and direction of this wind depends upon the physical and electrical geometry of the corona discharge system.

Earlier experimental studies of EHD flows in laboratory wire-to-plate precipitators (Masuda *et al.*, 1979; Ushimaru *et al.*, 1982; Leonard *et al.*, 1982,1983; Davidson and Shaughnessy, 1984a,b, 1986; Self *et al.*, 1987; McKinney, 1988; Davidson and McKinney, 1989,1990,1991; Riehle and Loffler, 1990; Kallio and Stock, 1990,1992) indicate that the tuft-like negative corona discharge typical of industrial precipitators generates substantial increases in free stream turbulence and diffusivity levels. An ordered secondary flow, like that numerically predicted and experimentally determined for a uniform positive discharge (Ramadan and Soo, 1969; Robinson, 1975; Yabe *et al.*, 1978; Berstein and Crowe, 1981; Yamamoto and Velkoff, 1981; Leonard *et al.*, 1983, Kallio and Stock, 1992) and sketched in Figure 2.2(a) for a very low bulk flow rate, may be superimposed on the turbulent flow in a negative corona. Davidson and Shaughnessy (1986) speculate that once the current level is sufficiently high to create a closely spaced and uniform distribution of corona tufts along the wires, a similar flow pattern is established in a negative discharge precipitator. Larsen and Christensen's (1986) laser Doppler measurements of particle velocities in a small-scale barbed-wire precipitator reveal a pair of highly structured recirculating vortices moving transverse to the bulk flow at each discharge point. As depicted in Figure 2.2(b), the structure of this secondary flow is determined by the barb spacing and the effect is reinforced by the regular barb pattern on multiple wires. Ushimaru and co-workers (1982) observed a similar, although less ordered, flow pattern with a randomly distributed spotty discharge along smooth wires. Yamamoto and Sparks (1986) speculate that with multiple tuft wire discharges, each discharge spot creates an elliptically shaped vortex as sketched in Figure 2.2(c). Flow visualization by Kallio and Stock (1990) in a negative polarity wire-plate precipitator shows recirculating patterns similar to those observed with a positive corona discharge. The difficulty of solving the three-dimensional fluid dynamics equations has precluded a numerical prediction of the flow resulting from tuft discharges along the wires. Although they acknowledge that their 2-dimensional simulation is inadequate, Kallio and Stock (1992) argue that a 2-dimensional solution to the governing turbulent flow equations in the wire-plate precipitator may be used in a negative corona if the tufts are closely spaced (tufts become closer at higher voltage levels). It is certainly not clear that this is true given the measured differences in turbulence intensity in positive and negative coronas (Kallio and Stock, 1992).

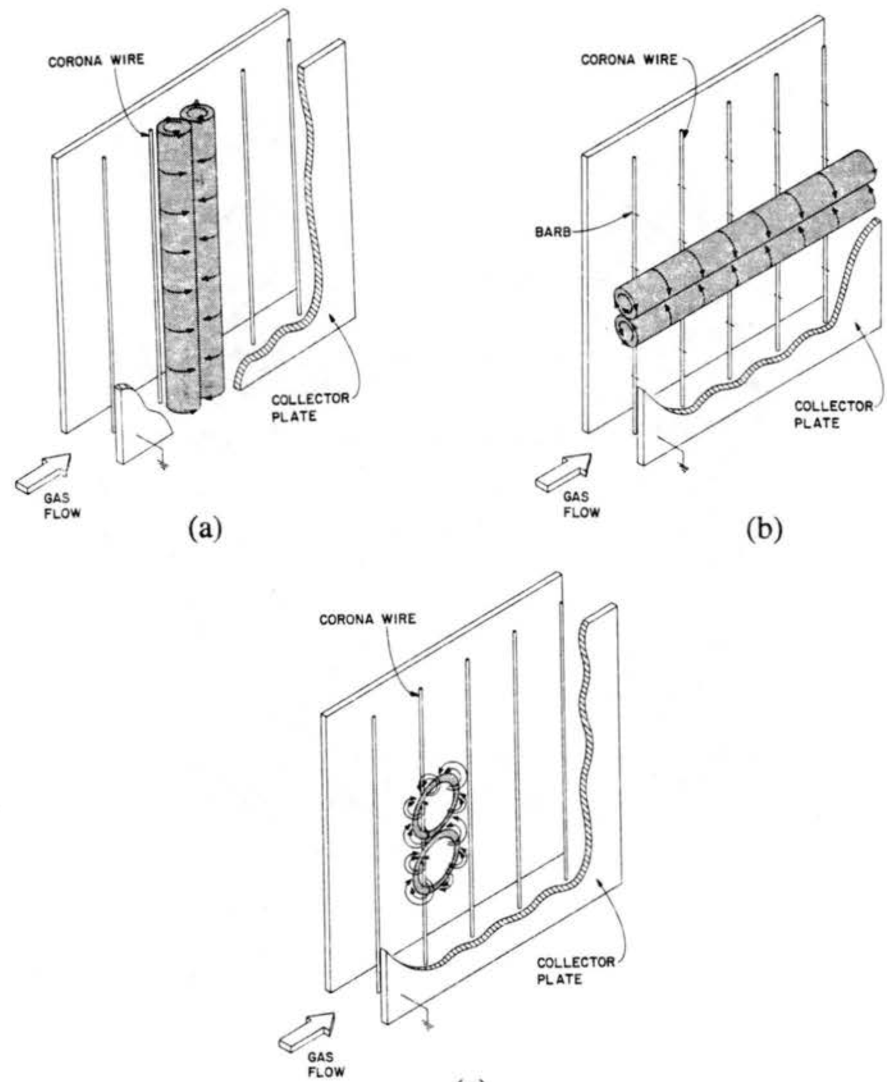

Figure 2.2. Secondary flows in the wire plate precipitator: (a) Positive corona with smooth wires (based on numerical calculations of Yamamoto and Velkoff, 1981); (b) Negative corona with barbed wires (based on particle velocity measurements of Larsen and Christensen, 1986); (c) Negative tuft discharge (speculation by Yamamoto and Sparks, 1986, after numerical calculations).

Control of the electrically generated flow is theoretically possible by altering the structure of the rotational electric body force acting on the gas field,

$$\mathbf{F_e} = (\rho_c + \rho_p)\mathbf{E}, \tag{2.2}$$

with a modification in electrode geometry (Davidson and Shaughnessy, 1986; Shaughnessy *et al.*, 1985). Here, ρ_c is the ionic space charge, ρ_p is the particulate space charge, and $\mathbf{E}$ is the electric field. Since turbulent diffusion and particle transport are dominated by large scale turbulent eddies, the detrimental EHD effects may be reduced by decreasing the length scale of the induced fluid motions. Atten *et al.* (1985, 1987) suggest that in the presence of charged particles, no significant reduction in the EHD flow disturbances can be expected by controlling only the ionic component of the body force. This statement does not appear reasonable in view of the magnitude of the known ionic flow modifications. The relative magnitudes of the ionic and particulate space charge depend on several factors including electrical operating level, and particle loading and size distribution. Shaughnessy and Solomon (1991) point out that the velocity scaling used by Atten *et al.* appears to be incorrect for gases because of the low electrokinetic conversion efficiency (Robinson, 1961) in gases and because the electric body force is left unbalanced in the scaled Navier-Stokes equations. In an experimental study, Peterson (1993) did not detect any modification in a turbulent duct flow caused by charged particles of the size and concentration typically found at the exit of industrial precipitators.

The relative magnitude of the electric body force to the viscous forces acting on the gas is given by the dimensionless electrohydrodynamic number N_{EHD} defined as

$$N_{EHD} = \left(\frac{Id}{\beta A \rho U^2} \right), \tag{2.3}$$

where I is the total current, d is the channel width, ß is the ionic mobility, A is the ground plate area, ρ is the gas density, and U is the bulk gas velocity. A typical average N_{EHD} value in an industrial ESP is 1.0. Local values may vary substantially and depend upon the current density.

Theoretically, there are three electrode geometries in which the electric body force may be irrotational and produces no flow disturbance (Flippen, 1982). A symmetric positive corona discharge on a clean smooth discharge surface in concentric spheres, concentric cylinders, and parallel plates affects only the pressure distribution of the gas. Clearly, the wire-to-plate precipitator, in which the discharge and current distribution are inhomogeneous in both the longitudinal and axial directions, is disadvantageous from a gas flow standpoint. An electrode design which reduces the length scale of the discharge nonuniformity should theoretically reduce the scale of the induced flow.

Of the three special geometries, the parallel plate geometry is the most promising in terms of retrofit applications. Unfortunately a uniform sheet discharge is not physically possible without an external source of ions. However, a discharge may be established along a plate at raised points or barbs. Several patents (Blier, 1971; Bridge, 1906; Fortescue, 1922; Robertson, 1974; Shively, 1940; Steuernagel, 1969) suggest variations of the barbed plate electrode, but none mentions the fluid dynamics of such a design.

The barbed plate design does not produce a uniform discharge but may reduce the scale of the electrical nonuniformity within the precipitator flow channel. Figure 2.3 is a sketch of the design. In this geometry, the EHD flow is envisioned as closely spaced corona wind jets originating at the individual barbs. Although such an electrode design cannot eliminate electrohydrodynamic flow disturbances, it does offer the possibility of reducing scales of current inhomogeneities and of electrically generated secondary flows and turbulence.

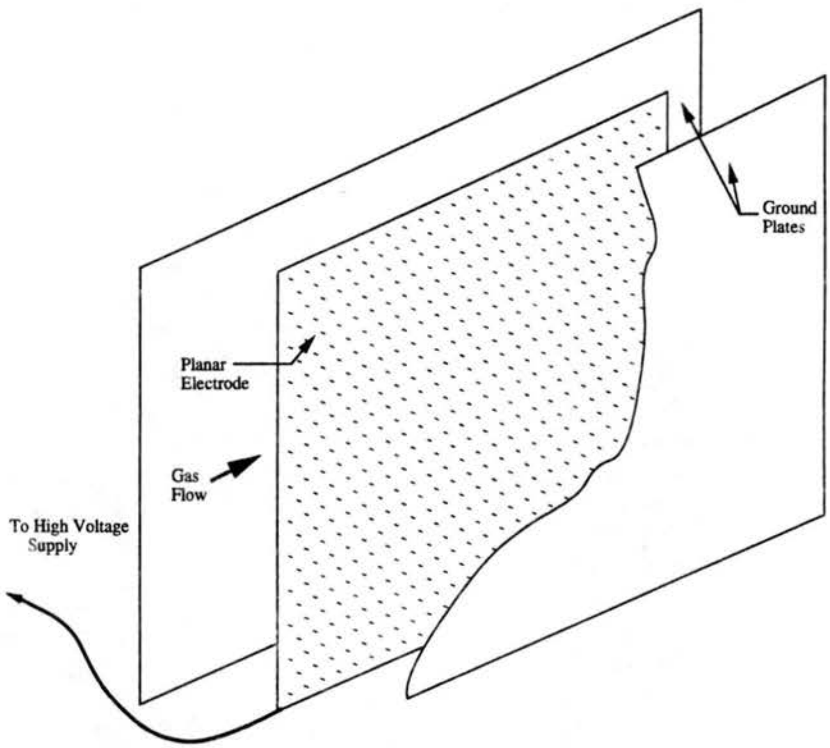

Figure 2.3. Barbed plate precipitator schematic.

In prior studies of the fluid mechanics of barbed plate precipitators (McKinney, 1988; Davidson and McKinney, 1989,1990,1991) turbulence intensities and diffusivities were measured in the flow downstream of the active electrode section using hot-film anemometry. The data show modest reductions in turbulent diffusivities at bulk gas speeds less than 1.0 m/s when compared to data for the wire-plate geometry, particularly for current densities greater than 1.0 mA/m^2. However, the lack of information on the flow in the inter-electrode space is a serious limitation in comparing performance of this design to that of the conventional wire-plate geometry. The objectives of the this research are to characterize current distribution and particle velocities in a barbed-plate precipitator. Results are compared to similar data obtained in a conventional wire-plate geometry.

CHAPTER 3.0

EXPERIMENTAL METHOD

The experimental research is divided into five phases. The first and second phases are selection of an optimal barb pattern based on uniformity of the corona current distribution at the ground plane and comparison of electrical characteristics of the optimized barbed plate to the conventional wire-plate geometry. The second and third phases consist of laser Doppler anemometer (LDA) measurements of axial and transverse particle velocities within laboratory scale barbed plate and wire-plate electrostatic precipitators and visualization of the flows using a laser light sheet. The final phase is observation of particle deposition on the collector plates. The effectiveness of the barbed plate design is assessed by comparing current distributions, particle velocities and particle deposition patterns of the barbed plate precipitator to those of the conventional wire-plate geometry.

3.1 Electrical Characteristics and Barb Optimization

3.1.1 Current Distribution Measurements

The principal aim of using the barbed plate is to create as uniform a current density distribution as possible. The optimal barb pattern is the one that creates the most uniform current density in the inter-electrode space while allowing minimal gas flow in the low current areas between the barb tips and the high voltage plate. Measurement of space charge and current is difficult in a three-dimensional electrode configuration, such as the barbed-plate, since introduction of a probe into the region distorts the field and produces erroneous results. Therefore, uniformity of current is assessed by comparing ground plane current distributions for various barbed-plate configurations. Current distributions are measured over a segmented ground plane mounted in the precipitator test section of the wind tunnel (described in Section 3.2 of this Chapter) as well as along an *X-Y* traversing ground plane external to the tunnel.

As shown in Figure 3.1, the ground plane corona current distribution from a barbed plate electrode depends on the geometric parameters barb length (ℓ), barb tip-to-plane spacing (L), plate-to-plane spacing ($d = \ell + L$), barb-to-barb spacing (s), barb radius of curvature (r) and barb arrangement as well as applied voltage (V).

The *X-Y* traversing plane shown in Figure 3.2 is used to obtain detailed ground plane current distributions external to the tunnel. The center of the ground plane contains a 2.5 mm diameter probe that is electrically isolated from and physically flush with the plane. The plane and the probe area are tied to ground through a microammeter and a nanoammeter, respectively. Discharge electrodes are suspended above the ground plane and may be moved vertically. Current density distributions are obtained by traversing the ground plane beneath a discharging electrode and measuring the current to the probe. Negative dc voltages are supplied with a low ripple (maximum 2%) high voltage power supply.

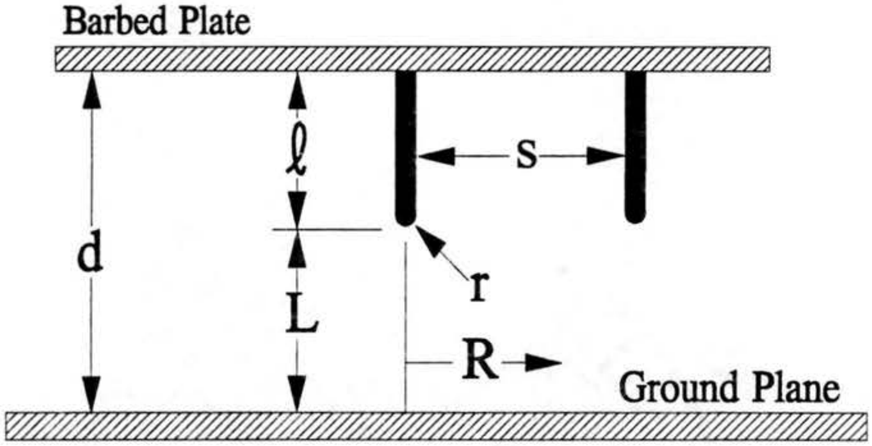

Figure 3.1. Diagram of dimensional variables in the barbed plate-to-plane.

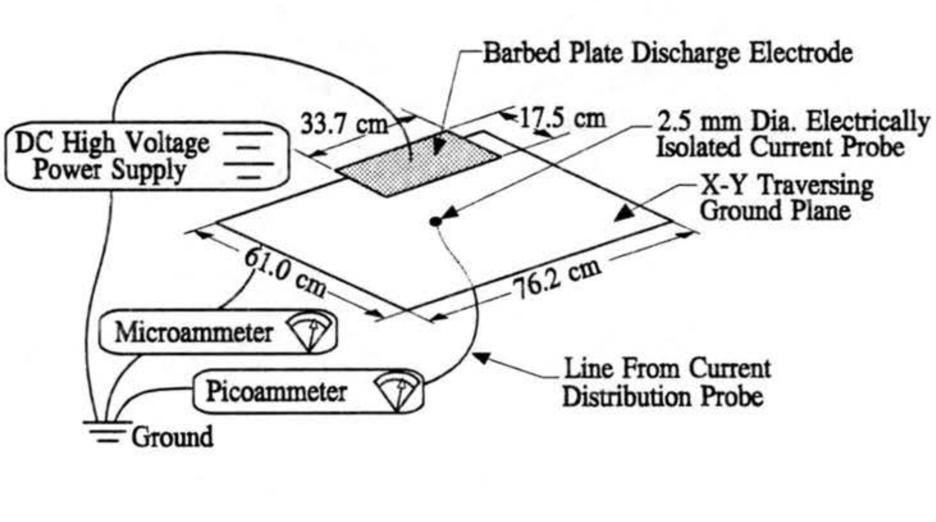

Figure 3.2. Schematic of corona current test apparatus.

3.1.2 Current Density Visualization

A second method of obtaining information about current density patterns on the ground plane is through visualization. Two methods are developed. One takes advantage of back corona and the second of oxidation of the ground plate. The back corona method involves placing a sheet of paper on the ground plane directly beneath the discharging barbs. By using a relatively thin, fibrous paper (regular copy paper or thin tissue paper works well), the fibers of the paper glow with a "back corona" at any location to which current is flowing. A single spike, for instance, creates a small glowing disk on the paper. The "disk" is really a region of many discharges on the paper fibers. The glow does not occur in the absence of an ion source bombarding it from the negative electrode. Although this method provides a quick and easy way of visualizing the current distribution, it is difficult to produce a good "hard copy" to take away and examine. Commercial photographic paper contains an emulsion which is not conducive to the back corona, and using a camera is difficult because of the angle at which one must view the back corona. Use of a "conductive glass" or a glass coated with a thin metal film for either the discharge or the ground plane may be a solution to this problem. A second problem with the technique is the fact the corona discharge occurring on the paper fibers creates a space charge opposite to the polarity of the normal corona discharge and therefore changes the electrical conditions of the experiment. This problem does not appear to have a pronounced effect on the resulting visual pattern, however.

A second method for recording the current density distribution is to place a clean copper plate on the ground plane beneath the discharge electrode. Over a period of 24 to 48 hours, ion bombardment of the copper surface oxidizes the copper in any region to which current is flowing. While this method is not good for immediate visualization, it is an extremely useful way of recording a current density image. A plate sanded with fine wet sandpaper seems to work well and is easily photographed after being removed from the test facility. This technique has the added benefit of not producing the positive ions that the paper procedure produces (if the corona is negative) so that electrical conditions are not disturbed.

3.2 Laboratory Precipitator

3.2.1 EHD Wind Tunnel

Precipitator particle velocities are measured in a precipitator test section installed in a two-dimensional wind tunnel in the Electrohydrodynamic Lab (EHD Lab), which is part of the Fluid Dynamics and Diffusion Laboratory (FDDL) at Colorado State University.

The EHD wind tunnel, shown in Figure 3.3, is a vertical loop tunnel which can be operated as a closed loop tunnel or may be configured to allow air to enter from and exit to the exterior atmosphere. The 122 cm diameter vaneaxial fan is manufactured by the Buffalo Forge Company (490 Broadway, Buffalo, NY 14204). The fan is controlled by a Louis Allis (16555 W. Ryerson Road, New Berlin, WI 53151) Saber 3300 3-phase, non-regenerative, DC static drive. The motor is a Louis-Allis Flexitoro 20 H.P. type GPNR motor (model 718336G001).

The tunnel has two test sections, one in the upper portion of the loop and the other in the lower. The upper test section is 122 cm square and 9.8 meters in length. The lower section is 61 cm square and is 4.6 meters in length. The vertical channel serves as a

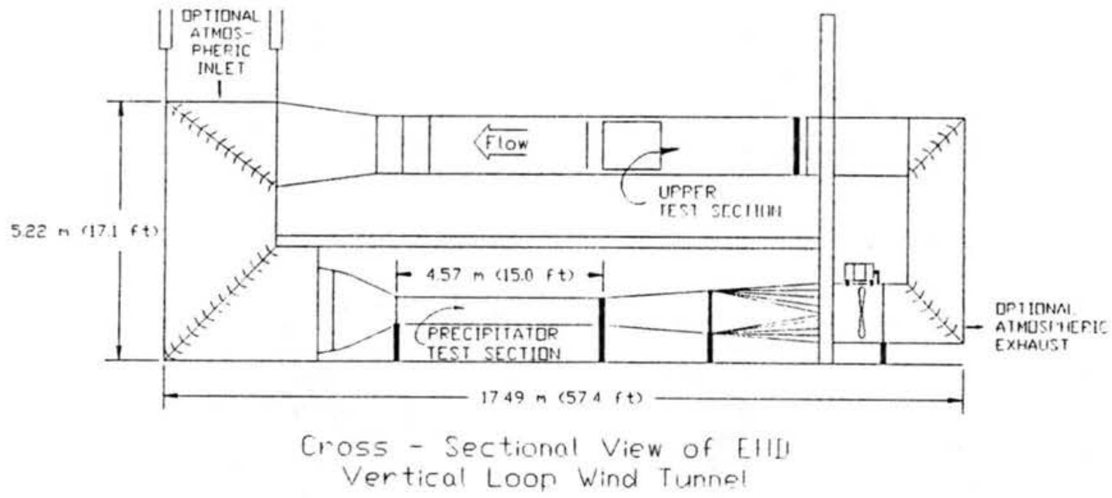

Figure 3.3. EHD wind tunnel schematic.

large manifold for the lower test section. There is a smooth contraction preceding the lower test section and a divergence following it to bring the tunnel diameter to 122 cm at the fan. The fan and controller system are capable of providing velocities from 0 to 52 m/s in the lower test section.

The model precipitator test channel is built into the lower test section as shown in Figure 3.4. Air enters the channel through a 7.5 cm thick aluminum honeycomb flow straightener with 10.0 mm cells and passes through a contraction that reduces the 61 cm square cross section to a rectangular section 61 cm high and 15.25 cm wide. A second 5.0 cm thick flow straightener with 2.5 mm cells is placed at the end of the contraction. The 61 cm by 15.25 cm test channel is constructed of ten removable panels to facilitate tunnel entry and electrode replacement and modification. The panels are constructed with

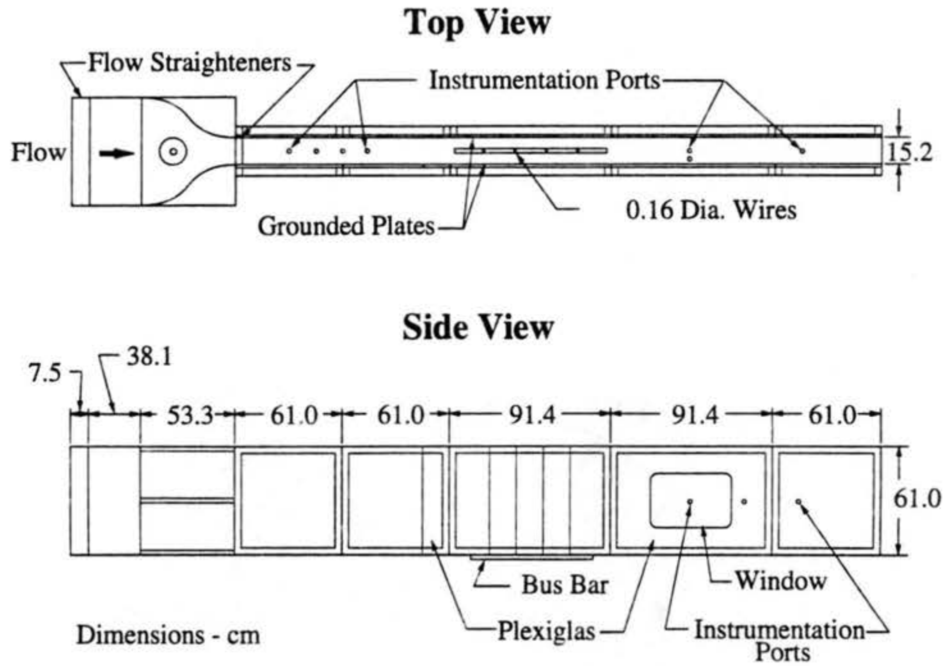

Figure 3.4. Model precipitator test section in EHD wind tunnel.

frames of standard 2 by 4 inch lumber (5 cm by 10 cm) which support 2 cm thick plywood and/or Plexiglas panels to form the wall of the flow channel. Each panel is bolted to both the floor and the roof of the tunnel. One Plexiglas panel contains a 30.5 cm by 45.7 cm window to permit easy access to the tunnel. The 91.4 cm long precipitator model begins 121.9 cm downstream of the second contraction and flow straightener. The section of the tunnel ceiling at the test section is removable to provide access and facilitate different electrode configurations and may be replaced with new Plexiglas to provide a clear optical path for the laser Doppler system.

The two-dimensional test channel exits into the center 7.6 cm by 61.0 cm section of a 29.2 cm deep 61 cm square Astrocel Superinterception absolute air filter manufactured by American Air Filter (215 Central Avenue, Louisville, Kentucky 40208).

The filter provides a large pressure drop that facilitates better control at low flow speeds. The background turbulence intensity in the test channel is 5% (McKinney, 1988).

3.2.2 Wire-Plate Precipitator Test Section

The wire-plate configuration is shown in Figure 3.5. Two special wind tunnel wall panels are constructed using 1.0 cm thick aluminum as facing. The aluminum plates are attached to plywood panels via five threaded holes in the back of each aluminum plate. The collector plates are electrically grounded to a common ground on the electrical "low side" of the power supply by 2 cm wide braided tinned copper cable. The discharge wires are mounted vertically along the centerline of the tunnel, between the plates. Four 1.6 mm diameter stainless steel wires are mounted at 15.2 cm intervals, 7.6 cm from each collector plate. High voltage is supplied to the wires by means of a "bus bar" mounted in the Plexiglas floor of the tunnel. The wires are connected to the bus bar using set screws to hold them into specially drilled holes. Small holes are drilled through the tunnel floor to permit the wire electrodes to be attached to the bus bar. Similar holes are drilled through the 1 cm thick removable Plexiglas tunnel ceiling panel. The tops of the wires are threaded and secured at the top of the tunnel with nuts. Silicone high voltage insulating putty is used to cover the nuts and any other nearby metal tunnel parts to prevent extraneous corona. To facilitate laser beam entry during laser Doppler measurements, the bus bar is placed on the top of the tunnel and the threaded end of the wires on the bottom. A second set of longer wires is used that are bent just outside the top of the tunnel so that the bus barb is shifted 3.8 cm off of the centerline of the tunnel.

When measuring current densities, one smooth collector plate is replaced by a segmented copper plate designed to allow measurement of current flowing to 36 separate

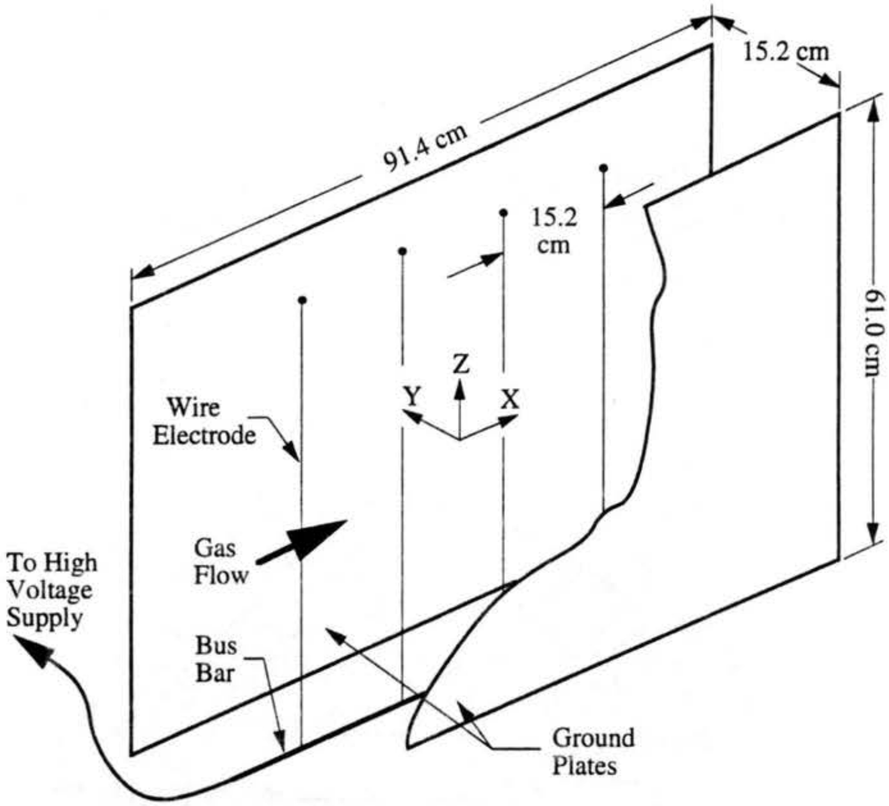

Figure 3.5. Wire-plate model precipitator configuration.

sections of the ground plate. The segmented ground plate is a 0.8 mm thick copper plate bonded with epoxy to a 7.9 mm thick fiberglass laminate board (the material used in printed circuit boards). The copper is cut into 5.08 cm by 5.08 cm sections with a 0.8 mm thick saw, resulting in a grid of 18 by 12 electrically isolated panels. A wire is soldered to the back of each panel through a pre-drilled hole in the fiberglass laminate. All wires are tied to ground though a switching junction box which allows for one wire (panel) at a time to be routed to ground though a microammeter.

3.2.3 Barbed Plate

In the planar electrode configuration illustrated in Figure 3.6, the barbed plate is mounted on one side of the test section channel and a ground plate on the other. In retrofit applications, this design requires removal of the wires and replacement of alternate collector plates with a two-sided barbed plate electrode. A wall panel made entirely of 2 cm thick Plexiglas is installed on the high voltage side of the tunnel to provide adequate insulation. To facilitate replacement and modification of the electrode, the planer electrode is attached to the Plexiglas wall using clear plastic tape. The high voltage power is supplied to the rear of the electrode though a small opening in the Plexiglas wall.

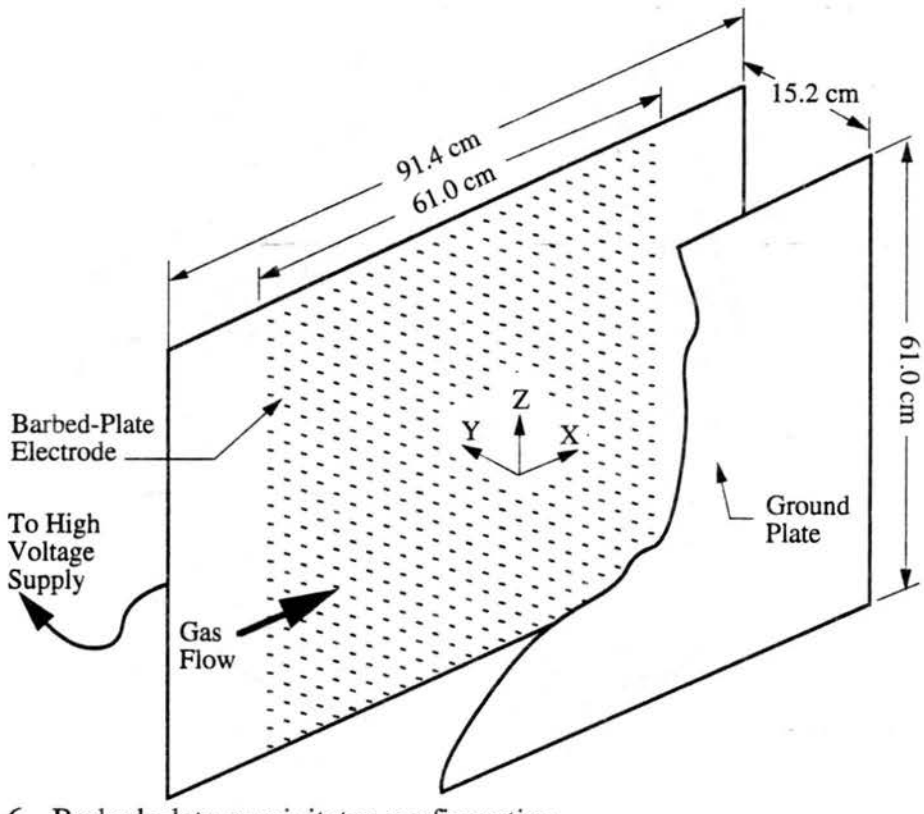

Figure 3.6. Barbed plate precipitator configuration.

The barbed plate is a 61.0 cm by 91.4 cm, 9.5 mm thick aluminum plate with 572 brass barbs set in the center 61.0 cm by 61.0 cm section of the plate with conductive epoxy. Each barb is an 1.5 mm diameter brass rod with a machined tip radius of 0.07 mm. Barbs are arranged as shown in Figure 3.7 in an hexagonal pattern with 27.0 mm barb-to-barb spacings. Length of the barbs is 15.9 mm except in rows nearest the up- and down-stream edges of the plate. Barb length is reduced in these rows to minimize preferential discharging of the edge barbs. The edge rows contain 9.5 mm long barbs and the rows adjacent to the edge contain 13.5 mm long barbs. Visual observation of the corona discharge indicates this slight reduction in barb length forces barbs at the edges of the plate to discharge with the same intensity as those in the interior. Selection of this pattern, length and spacing was made after performing the series of experiments described in Chapter 4.

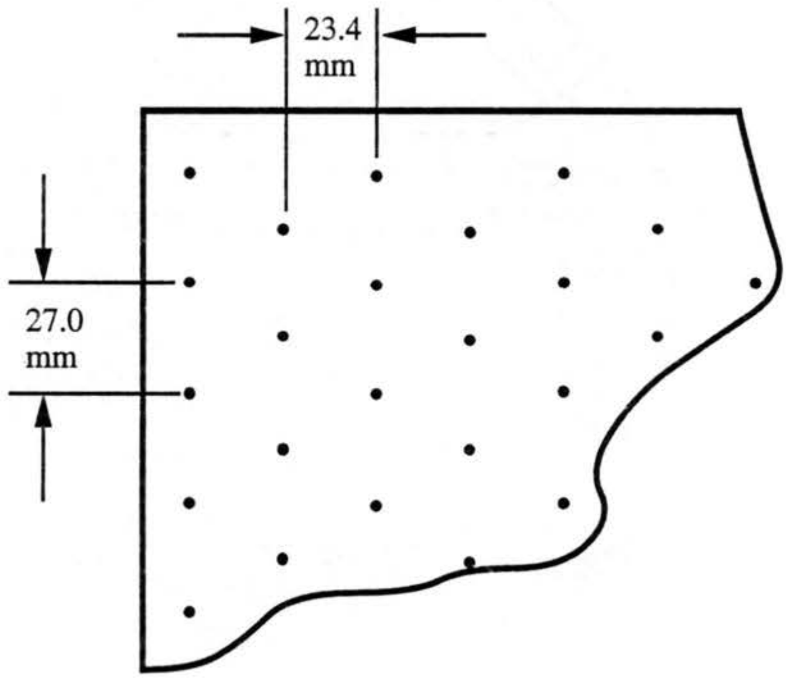

Figure 3.7. Hexagonal pattern barbed plate.

3.3 Particle Production and Sizing

3.3.1 Particle Production Instrumentation

Particles must be introduced into the precipitator test section for three of the major phases of the study: LDA measurements of particle velocities, flow visualization and particle deposition. LDA measurements are attempted with several different particles.

A Thermo Systems, Inc. (TSI) (500 Cardigan Road St. Paul, MN 55164) model 9306 six-jet atomizer capable of output particle concentrations as high as 4.3×10^6 particles/cm^3 at a volumetric flow rate of up to 12.0 liters/min is used to generate liquid droplets from oleic acid and solid particles from an aqueous solution of polystyrene latex (PSL) spheres. The PSL spheres adequately scatter light, but cannot be produced in high enough concentrations in the wind tunnel to obtain an adequate LDA data rate. The best approach is to use solid particles produced in a BGI (58 Guinan St. Waltham, MA 02154) Wright Dust Feeder which feeds packed powders or dusts into a flow stream. The output rate and size distribution are highly dependant upon the dust used and may be as high as 1.02 cm^3/min with variable flow rates from 10 to 40 liters/min.

3.3.2 Particle Selection

Selection of particle type and concentration is difficult since experimental requirements for simulating the industrial precipitator environment are not necessarily the same as the requirements for particle seeding for LDA measurements. To simulate PM_{10} conditions, the particles of interest in this study are less than 10 μm in diameter. A "good" precipitator particle has neither a very high electrical resistivity or a very low resistivity. Both conditions limit collection efficiency, the former by the retention of charge at the ground plane and hence the reduction of the electric field in the inter-electrode space, and the latter by the loss of charge and eventual re-entrainment of the particles. In order to simulate realistic precipitator operating conditions, particle resistivity should be similar to that of an average precipitable fly ash (1×10^8 to 1×10^{10} ohm-cm), while concentrations are to be on the same order as concentrations near the exit section of conventional ESP's (1.14×10^{-8} g/cm^3).

The requirements of the LDA system further restrict particle choices. The signal-to-noise ratio (SNR) is highly dependent upon the index of refraction and size of the particle. In general, larger particles, with diameters as large as the fringe spacing, produce a larger SNR, but the relationship is not linear. A high index of refraction is beneficial. Particle concentration must be adjusted so that enough particles pass through the probe volume to get a valid measurement but the SNR is not degraded by the recurring presence of more than one particle at a time in the probe volume. Particle requirements for flow visualization are similar to those for the LDA measurements in that a high index of refraction is helpful. Particle concentrations need to be increased, however, to provide a good view of particle motion.

Table 3.1 is a list of potential precipitator seed particles along with relevant parameters. Aluminum oxide is selected as laser Doppler and dust pattern seed particle for this study because it can be distributed reasonably well using the Wright Dust Feeder, has a fairly high index of refraction, and has a resistivity in the same range as fly ash.

The Wright Dust Feeder is mounted 1.7 m above the floor of the vertical "manifold" section of the EHD wind tunnel. A small aluminum plate is mounted at a 45 degree angle just below the downward particle output stream to help scatter particles in the manifold. This procedure produces mass concentrations of 3×10^{-7} g/cm^3 in the precipitator test section when the wind tunnel is operating at 1.0 m/s. The measured size distribution is shown in Figure 3.8. Count median diameter (CMD) of the particles is 0.7 μm.

Table 3.1. Seed particle characteristics.

Particle	Chemical Name	Size (μm)	Size Range or St. Deviation (μm)	Color	Index of Refraction	Form	Resistivity (ohm-cm)	Specific Gravity	Dielectric Constant	Source*
Fly Ash	Var., Major Comp.: SiO_2 17.3-63.6% Al_2O_3 9.8-58.4% Fe_2O_3 2.0-26.8% CaO 0.1-14.7%	Var.	Variable	Tan/ Gray	Variable	Dry	$1x10^8$ - $2x10^{12}$	0.7-2.6		
Aluminum Dioxide (Alumina)	Al_2O_3	~ 0.8	1.5	White	1.77	Dry	$1x10^{11}$ - $1x10^{16}$	3.965	4.5 - 9.5	1
Silicon Dioxide (Silica)	SiO_2	1.6		White	1.46	Wet	$1x10^{15}$		4 - 12 (for glass)	2
"	SiO_2	0.007	0.005-0.0013	White	1.46	Dry	$1x10^{15}$	2.2	4 - 12	3
"	SiO_2	4	1 - 9	White	1.46	Dry	$1x10^{15}$	2.2	4 - 12	3
Silicon Carbide	SiC	0.8	3% > 2.4 50% > 0.8 94% > 0.17	Gray	2.65	Dry	$1x10^2$ - $2x10^2$	3.2	40	4
"	SiC	1.7	3% > 4.7 50% > 1.7 94% > 0.5	Gray	2.65	Dry	$1x10^2$ - $2x10^2$	3.2	40	4
"	SiC	5.5	3% > 19.0 50% > 5.5 80% > 1.0	Gray	2.65	Dry	$1x10^2$ - $2x10^2$	3.2	40	4
Polystyrene Latex (PSL)	Polystyrene and Divinyl Benzene (8% by Weight)	1.11	0.011	White	1.55 - 1.6	Wet	$1x10^{15}$ - $1x10^{19}$	1.05	2.4 - 4.8	2
Polystyrene Latex (PSL)	"	3.09	0.089	White	1.55 - 1.6	Wet	$1x10^{15}$ - $1x10^{19}$	1.05	2.4 - 4.8	2
Polystyrene Latex (PSL)	"	8.0	0.4	White	1.55 - 1.6	Wet	$1x10^{15}$ - $1x10^{19}$	1.05	2.4 - 4.8	2
Glycerol (Glycerine)	$C_3H_5(OH)_3$	0.7 -1.1	± 1.3	Clear	1.55 (Glycerol)	Liquid				
Arizona Road Dust	S_iO_2 65-76% Al_2 11-17% FeO_3 2.3-5% Other 0-6%	CMD: 3 MMD: 4.5	38% < 5.5 54% < 11.0 71% < 22.0 89% < 44.0 100% < 176.0	Tan		Dry		2.3		5
Distilled Water	H_2O	0.8 - 1.1	± 1.3	Clear	1.33	Liquid		1.0		
Oleic Acid	$C_{18}H_{34}O_2$	~ 0.6		Brown (Clear)		Liquid		0.98		
Titanium Dioxide (from titanium tetrachloride)	TiO_2	CMD: 0.6		White	2.6 - 2.9	Solid		4.26		6

*1. Davison Chemical, Division of Grace Corp., Chattanooga, TN 37406

2. Duke Scientific Corp., 1135 D San Antonio Rd., P.O. Box 50005, Palo Alto, CA 94303

3. Degussa Corp., Pigments Division, 425 Metro Place North, Suite 450, Dublin, OH 43017

4. Washington Mills, Electro Minerals Corp., Niagra Falls, NY 14302

5. AC Spark Plug, Division of General Motors Corp., Flint, MI

6. Fisher Scientific Company, Chemical Mfg. Division, Fair Lawn, NJ 07401

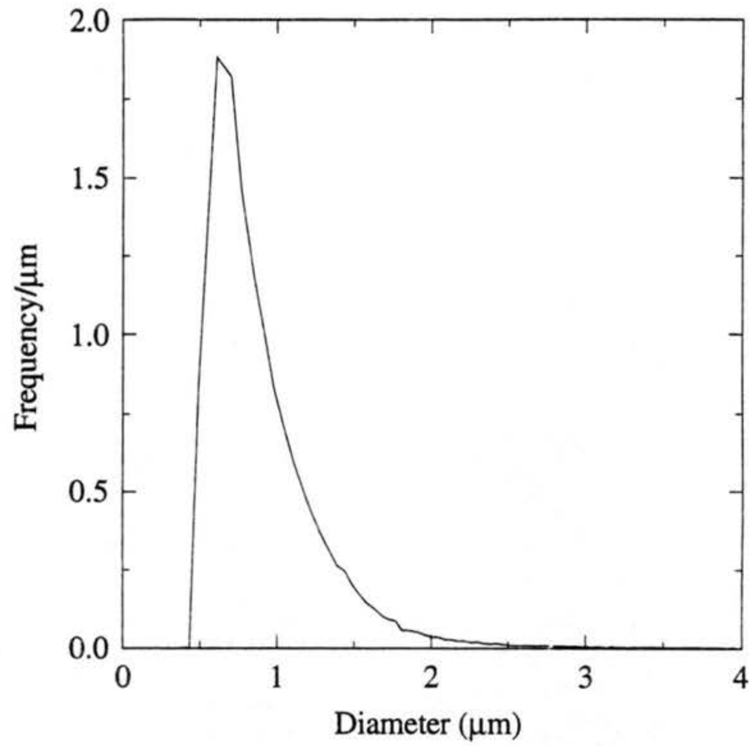

Figure 3.8. Particle size distribution for aluminum oxide particles.

3.3.3 Particle Sizing and Concentration Instrumentation

A Climet Instruments Company (1620 West Colton Ave., Redlands, CA 97243) model 208-A optical particle analyzer and a Tracor Northern (2551 West Beltline Highway, Middltown, WI 53562) model TN-1705 pulse height analyzer are used to obtain particle size and concentration distributions. The Climet particle analyzer is an optical system capable of measuring particles from 0.3 to 10.0 μm in diameter in concentrations up to 1400 particles/cm^3 by drawing particles from the flow via a sampling probe. Flow rate into the machine is 7.1 liters/minute and isokinetic sampling is achieved by using a 11.0 mm diameter probe for the bulk tunnel velocity of 1.0 m/s. The sampling probe is mounted through a threaded port on the side of the wind tunnel 122 cm downstream of the middle of the precipitator test section and situated so that the inlet is on the tunnel centerline.

The maximum particle concentration measurable by the climet is 1400 particles/cm^3 and the wind tunnel particle concentrations are on the order of 118,000 particles/cm^3. To resolve this problem, a metered portion of the air from the sampling probe is passed through a hepa filter system to dilute the sample concentration. The Climet analyzer produces an analog output signal of voltage pulses proportional to the optical size of particles present in its sampling volume. The non-linear calibration relationship is determined by the manufacturer.

The Tracor Northern pulse height analyzer digitizes pulse heights and builds a 512 interval histogram of pulse heights over the 0 to 10 volt input range, resulting in a resolution of 19.5 mV/bin. Due to the nonlinearity of the Climet output pulses, the particle size resolution ranges from 0.08 μm/segment for 0.3 μm particles to 0.02 μm/segment for the 10 μm particles. The data are dumped to the microcomputer via a standard 1200 baud serial link after sampling is complete.

Acquisition of particle size data from the pulse height analyzer is performed using a specially written ASYST-based (Keithly/Asyst, 440 Myles Standish Blvd., Taunton, MA 02780) program. Correction is made for any coincidence loss that may occur in the concentration measurements (from more than one particle being present in the sampling volume). The data is converted from a simple histogram to a size frequency distribution curve by dividing by the interval widths and the total number of particles.

3.4 Particle Motion

To assess the effect of electrode geometry on particle motion within the precipitator, streamwise and transverse (X and Y in Figures 3.5 and 3.6) particle velocities are measured in both the barbed plate and conventional wire-plate precipitators using a 4 Watt laser Doppler anemometer system. Particle velocities in an X-Y plane at a Z value corresponding to barb locations are measured for a control N_{EHD} value of 0.0 and operating values of $N_{EHD} = 1$ and $N_{EHD} = 2$, all at a bulk gas speed of 1.0 m/sec.

3.4.1 Measurement Technique

Laser Doppler anemometry has been used in prior studies of both gas flow fields and particle velocities in wire-plate electrostatic precipitators. The LDA is superior to hot-wire anemometry in this application because it is non-intrusive and not affected by the high voltage field. The difficulty with its use arises from the fact that particle velocities are affected by the Coulombic force and do not necessarily follow the gas motion. Previous studies have generally used small particles and assumed Coulomb drift (β_p**E**) to be negligible (Larsen and Christensen, 1986; Leonard *et al.*, 1983). This assumption is valid only if β_p**E** is much less than **u**, the local gas velocity. In some regions of the precipitator, where the magnitude of the electric field is small, this assumption may be valid, but since the electric field is highly nonuniform, great care must be made in interpreting LDA measurements as gas velocities. The best approach to determining the particle drift velocity is measurement of β_p and **E** at the points of interest. This approach is unrealistic. An alternative is to estimate the drift velocity from numerical solutions to the governing electrodynamic equations (Maxwell's equations and

Ohm's law). A good review of LDA studies in wire-plate precipitators is given by Kallio and Stock (1992).

The primary approach taken in this study is to recognize that particle velocities, rather than gas velocities, are measured. Additionally, particle drift velocities are estimated using the numerical solution to the electrodynamic equations by Linnebur (1993). The Coulomb drift velocity,

$$w_e = \beta_p E \tag{3.1}$$

is estimated using local computed values for the magnitude of the electric field, E, and an average particle mobility, β_p. The local values for the electric field are gathered from the data of Linnebur (1993) presented in Figures 4.38, 4.40, B.2, and B.4, by estimating the transverse component of the gradient of the electric potential at each desired location. Electrical particle mobility is defined by equating the electrostatic force to Stokes drag ($F_D = 3\pi\mu U d_p$), resulting in

$$\beta_p = \frac{q_p C_c}{3\pi\mu d_p}, \tag{3.2}$$

where q_p is the particle charge, d_p is particle diameter, μ is dynamic viscosity of the gas, and C_c is the Cunningham slip correction factor (Hinds, 1982). The Cunningham correction factor is a correction to Stokes' law for particles less than 1.0 μm in diameter and is empirically defined as

$$C_c = 1 + \frac{\lambda}{d_p}\left[2.514 + 0.800\, e^{\left(-0.55\frac{d_p}{\lambda}\right)}\right], \tag{3.3}$$

where λ is the mean free path of the air molecules. It can also be written dimensionally for air as

$$C_c = 1 + \frac{2}{Pd_p}\left[6.32 + 2.01\ e^{\left(-0.1095\ Pd_p\right)}\right], \tag{3.4}$$

where P is absolute pressure expressed in cm Hg, and d_p is in μm (Hinds, 1982). An average particle mobility is determined by using the count median particle diameter (0.7 μm for the alumina) and by assuming that all particles have reached saturation charge.

Charging of particles of the 1.0 micron size range in an ESP is the result of two phenomena, diffusion charging and field charging. Diffusion charging is the result of the interaction of a particle with a field of unipolar ions in Brownian motion and is written as

$$q_p(t) = \frac{4\pi\varepsilon_o\ d_p k\ T_A}{q_i}\ \ln\left(\frac{d_p\ \rho_c\ q_i^2\ \bar{c}_i}{4\varepsilon_o\ k\ T_A} + 1\right), \tag{3.5}$$

where ε_o is the permittivity of free space, k is the Boltzman constant, T_A is the absolute temperature, q_i is the charge of the ions, ρ_c is the space charge density, $\bar{c}_i$ is the mean speed of the ions, and t is the elapsed time (White, 1963; Robinson, 1973).

There is some confusion in the literature about the appropriate value to use for the speed of the ions, $\bar{c}_i$. White's (1963) original presentation calls for the use of the rms molecular speed based on the Maxwell-Boltzmann velocity distribution. Hinds (1982) suggests the use of the arithmetic mean based on the same distribution. Robinson (1973) presents a simpler formulation by Bernoulli while Liu *et al.* (1967) determined experimentally that the value of 118 m/s works well for corona ions and small particles (see Reist, 1984). The latter value is used in this study.

Field charging is particle charge acquired due to ions colliding with the particle while moving under the influence of the electric field, and is written as

$$q_p(t) = 4\pi\varepsilon_o \, p \, d_p^2 \, E \left(\frac{t}{t + \tau}\right), \tag{3.6}$$

where t is the elapsed time, τ is a particle charging time constant,

$$\tau = \frac{4\varepsilon_o}{\rho_c q_i \beta}, \tag{3.7}$$

and p is

$$p = 2\left(\frac{\varepsilon - 1}{\varepsilon + 2}\right) + 1, \tag{3.8}$$

where ε is the relative dielectric constant of the particle. The maximum charge to which the electric field can charge a particle occurs when the particle has gained enough charge to direct all electric field lines around the particle instead of through it. This condition is known as the saturation charge and it is at this charge that particles are generally regarded as "fully" charged. Saturation charge is represented in Equation (3.6) as t becomes large compared to τ. Particles may still gather a slight bit more charge due to diffusion charge, however.

For the purposes of this study, particles are assumed to be fully charged when they reach saturation charge through combined diffusion and field charging. The electric field used in the charging equations is the average electric field defined as E = V/L, where V is the voltage applied across the precipitator and L is the electrode spacing. The average space charge is determined by applying the nominal current density and average electric field to Ohm's Law ($J = \beta v \,|\rho_c|\, E$). Ions are assumed to be singly charged so that q_i = e, the charge of an electron.

3.4.2 Instrumentation

Particle motion within the ESP test sections is characterized with laser Doppler anemometer measurements of particle velocities in the X-Y plane. Figure 3.9 illustrates the hardware setup of the LDA system. The LDA is a one-dimensional dual-beam system operated in a forward scatter configuration. The 4 Watt argon-ion laser, its power supply, and the LDA optics are mounted on a traverse capable of movement in three directions. The 514.5 nm green line of the laser is directed down through the vertically aligned optics and into the precipitator test section via a mirror. The Dantec (6 Pearl Court, Allendale, NJ 07401) model 55X LDA optics consist of a ¼ wave plate, a beam waist adjuster, a beam splitter, a Bragg cell to shift the frequency of one beam, a beam displacer, a backscatter section to which the photomultiplier tube may be attached, and a 600 mm focal length front lens. A 40 MHz excitation signal is supplied to the Bragg cell by the Dantec model 55N10 LDA frequency shifter to provide the optical shifting of one of the two laser beams. The shifting of one beam permits the measurement of both the forward and reverse flows.

The photomultiplier tube and receiving optics are mounted below the tunnel and approximately 10 degrees off of the optical axis. Power is supplied to the photomultiplier tube with a Pacific Photometric Instruments (5675 Landregan St., Emeryville, CA 94608) model 204 negative high voltage power supply, capable of providing 2000 volts. Light scattered to the photomultiplier tube optics by a particle in the beam crossing is reflected through a pinhole into the photomultiplier tube where the light energy is converted to electrical current. The photomultiplier tube output is mixed with a signal of a user selected frequency between 31 MHz and 49 MHz in the frequency shifter to provide the

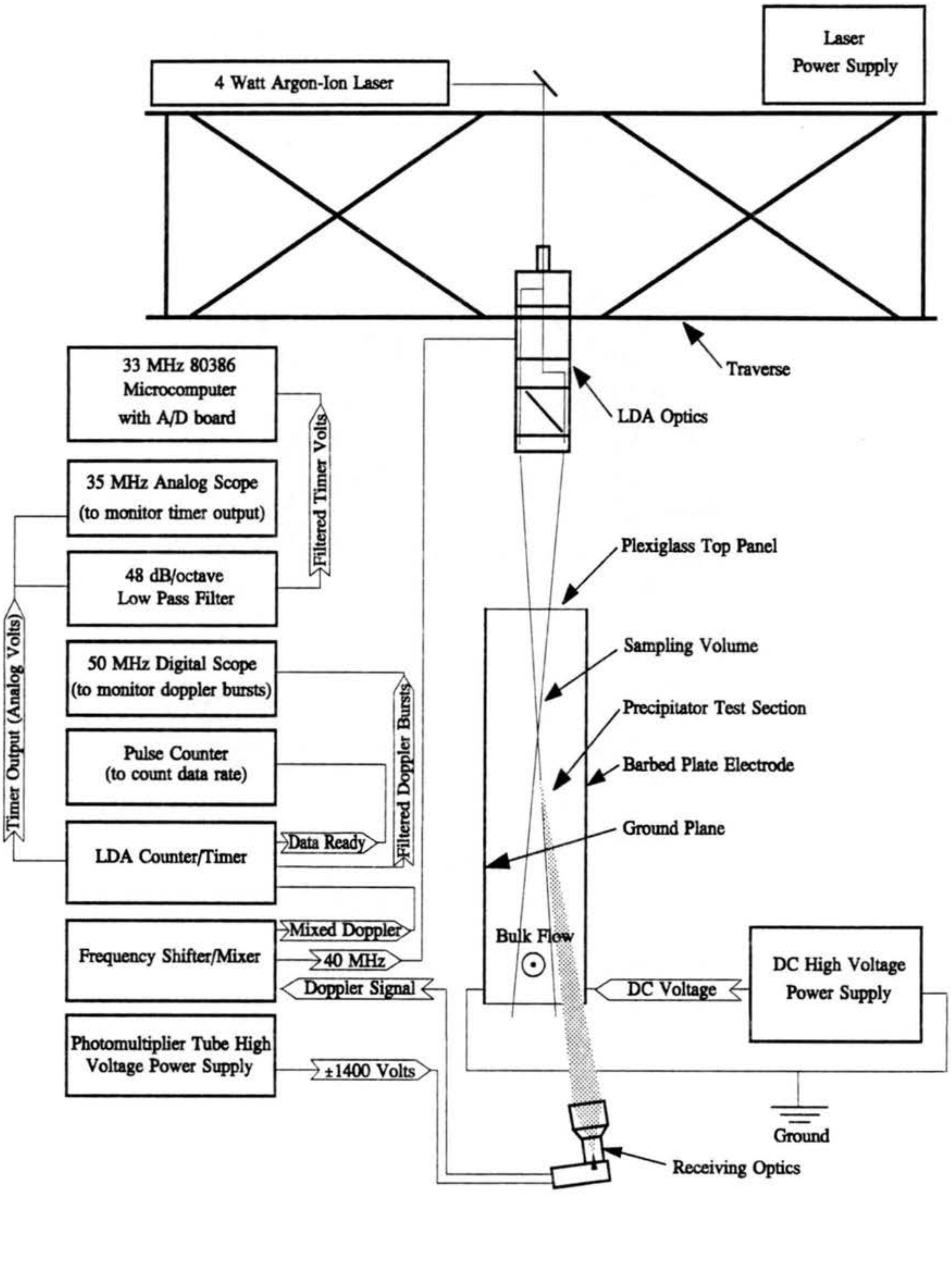

Figure 3.9. Laser Doppler setup and instrumentation.

final shifted Doppler signal. Detection of the Doppler frequencies is performed with a TSI model 1980B counter-type signal processor. A Tektronix (P.O. Box 500, Beaverton, OR 97077) model 2210 100 MHz digital oscilloscope is used to monitor the Doppler bursts after band pass filtering in the counter. The analog output of the counter's timer module is sent to a Tektronix model T932A 35 MHz oscilloscope for monitoring and to an A/D board through a Rockland (Rockleigh Industrial Park, Rockleigh, NJ 07647) model 2382 dual channel 48 dB/octave low pass filter to prevent aliasing. The 12-bit A/D board is a Metrabyte (Keithley/Metrabyte, 440 Myles Standish Blvd., Taunton, MA 07280) DASH16F and is located in a 33 MHz 80386-based IBM-compatible personal computer. A Hewlett-Packard (3495 Deer Creek Rd., Palo Alto, CA 97304) model 5233L electronic counter is used to monitor the "data ready" signal on the TSI counter-timer module and obtain an estimate of the Doppler burst data rate.

Placement of the receiving optics in backward scatter configurations (both on- and off-axis) is attempted before placement in the off-axis forward scatter position. A backscatter configuration is much more convenient than forward scatter because the receiving optics move with the transmitting optics, eliminating the need for an extensive traverse or optical re-alignment at each desired measurement location. Unfortunately particles near 1.0 μm in size scatter light preferentially in a forward direction, making backscatter measurements difficult without very short focal length receiving optics. Because of this problem the forward scatter configuration is used with the penalty (for this experimental set-up) that traverse motion is extremely limited due to the long focal length of the receiving optics lens and cramped space below the wind tunnel.

3.4.3 Data Sampling and Calculations

Output of the LDA counter-timer is sampled at regular time intervals with the A/D board and is in the form of a voltage representing the time for **n** fringe crossings, or **n** cycles in the Doppler burst. The voltage available at the counter-timer module analog output is the value for the last burst recognized by the counter. Since the burst rate is not steady and cannot be predicted, the A/D sample rate must be somewhat slower than the average burst rate measured at the "data ready" output. The maximum data rate is determined by studying the LDA timer voltage output signal on an oscilloscope and finding the longest time between new data points from the LDA timer. This time is the maximum sample rate that can be used in order to avoid sampling the same data twice.

Mean and root-mean-square (rms) particle velocity measurements are made using the program REALFLEX, written in the ASYST 4.0 language. REALFLEX employs the direct memory access feature of the PC to compute and update mean and rms values while new data is being acquired. Digitized 512 point time series of voltages are converted into fringe crossing times and then into mean and rms velocities and averaged with any previous mean and rms results to give the updated values. The 512 point segments are sections of a continuous time series that may be sampled for as long as necessary. All raw data is saved to disk for computation of the autocorrelation and integral length scales.

For an argon-ion laser green line at 514.5 nm, a beam spacing of 60 mm, and a front lens focal length of 600 mm, the resultant fringe spacing is 5.148 μm. After introduction of the 40 MHz optical shift to the downstream beam and an electronic shift of the Doppler signal between 31 MHz and 40 MHz, the resultant expression for velocity in terms of Doppler frequency is

$$u = \frac{\left(f_d' - f_s\right)\lambda}{2\sin\left(\frac{\theta}{2}\right)} = 5.15\times10^{-6}\left(f_d' - f_s\right), \tag{3.9}$$

where f_d' is the shifted Doppler frequency, f_s is the frequency shift, λ is the laser wavelength, and θ is the beam crossing angle. The equations for the mean and rms particle velocities are

$$U = \frac{1}{N}\sum_{i=1}^{N} u_i, \tag{3.10}$$

and

$$u_{rms} = \left(\frac{1}{N}\sum_{i=1}^{N}\left(u_i - U\right)^2\right)^{\frac{1}{2}}, \tag{3.11}$$

respectively, where u_i is the time series of instantaneous particle velocities. Both quantities are calculated for the streamwise and transverse flow directions (u and v). Rms velocities are also computed as the vector sum of the streamwise (u_{rms}) and transverse (v_{rms}) rms velocities. Local turbulence intensities are computed as:

$$I\% = \frac{\sqrt{\left(u_{rms}^2 + v_{rms}^2\right)}}{\sqrt{\left(U^2 + V^2\right)}} \times 100. \tag{3.12}$$

Estimates of the streamwise integral length scale, ℓ_x, are made by first computing the direct autocorrelation coefficient,

$$R(r\Delta t) = \frac{1}{(u_{rms})^2(N-r)}\sum_{n=1}^{N-r} u_i u_{i+r} \qquad r = 0,\ 1,\ 2\ \ldots\ m, \tag{3.13}$$

where r is the lag number, Δt is the inverse of the sample frequency, N is the total number of samples, and m is the maximum lag number. Here the maximum lag is the lag at which $R \rightarrow 0$. The correlation coefficient is integrated numerically from r = 0 to the point that the curve drops to r = 0.2. The resulting time scale is multiplied by the mean velocity to obtain an estimate of the length scale. The time scale is defined by integrating only to the time τ at which r = 0.2 in order to avoid unrealistically large time scales. The transverse integral length scale, ℓ_y, is computed in the same manner but with transverse velocities (v_i,v_{rms}) substituted into Equation 3.13.

Streamwise diffusivities can be estimated as

$$D_x \propto u_{rms}\, \ell_x \tag{3.14a}$$

and transverse diffusivities as

$$D_y \propto v_{rms}\, \ell_y. \tag{3.14b}$$

3.5 Flow Visualization

Laser light sheet flow visualization in planes perpendicular to and parallel to the flow direction provide a more global view of particle motion within the precipitator. All lines of the 4 Watt argon-ion laser are directed through a glass rod used as a cylindrical lens to create a light sheet. The glass rod and a small mirror are placed in the wind tunnel downstream of the test section and oriented so that the sheet forms a horizontal plane in the test section. The vertical position of the plane matches the vertical position of the LDA measurements. Titanium tetrachloride is introduced into the test section by moistening a paper towel with the solution and placing it on a small ring stand in the contraction of the wind tunnel (between the two flow straighteners). Solid titanium dioxide particles are formed as the liquid reacts with moisture in the air. Any resulting titanium dioxide (TiO_2) particles that are in the plane of light are illuminated and reveal motion in that plane. Particle size distribution of TiO_2 particles in the tunnel are shown in Figure 3.10. The CMD of the titanium dioxide is 0.6 μm. Both 35 mm slide and 35 mm black-and-white photographs are taken.

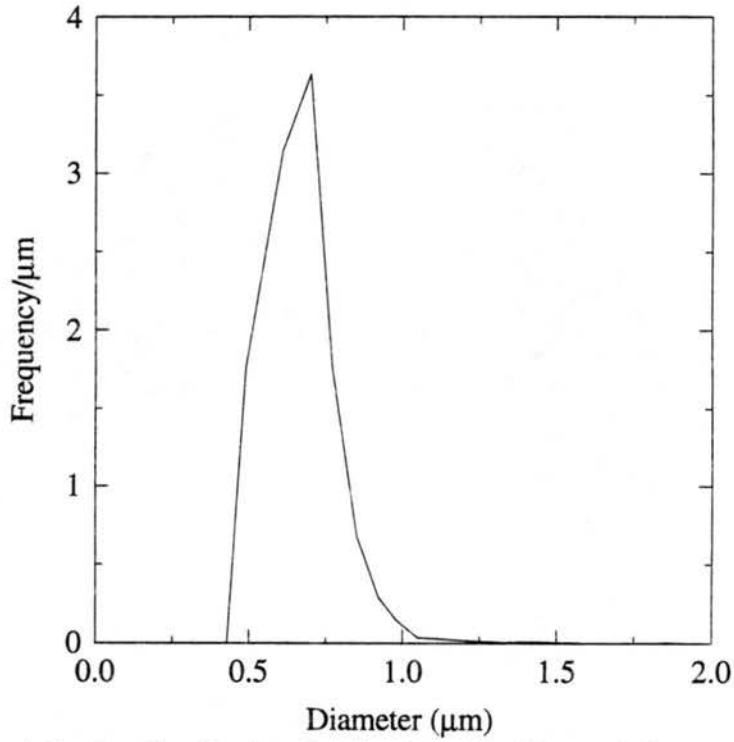

Figure 3.10. Particle size distribution for titanium dioxide particles.

3.6 Dust Collection

Particle collection is evaluated by examining the ground plate dust collection pattern for both electrode geometries. Each precipitator is operated at $N_{EHD} = 2$ for 1¼ hours with an inlet dust supply of 3.0×10^{-7} g/cm^3 of aluminum oxide. The resulting ground plate dust patterns are photographed with 35 mm slide and black-and-white film.

CHAPTER 4.0

RESULTS

Results of the experiments described in Chapter 3 are presented here. Ground plane current density measurements and oxidation pattern visualizations are presented for various barbed plate geometries in Section 4.1. Section 4.2 contains similar data comparing the optimized barbed plate to the wire-plate geometry. Sections 4.3 and 4.4 present the flow visualization and laser Doppler velocimeter results, and Section 4.5 contains photographs of ground plate dust collection patterns.

4.1 Current Density Distribution of Barbed Plates

Past research on point discharges has focused on the isolated point-to-plane. In 1899 Warburg found that the current distribution at the plane of a point-to-plane corona follows the empirical formula

$$J(\theta) = J_0 \cos^m \theta \quad \begin{cases} m = 4.82 & \text{Pos. corona} \\ m = 4.65 & \text{Neg. corona}\ , \\ \theta < 60^\circ \end{cases} \tag{4.1}$$

where J_0 is the centerline current density and θ is the angle from the centerline. Subsequent research has confirmed the *Warburg distribution* (Chattock, 1899; Tassicker, 1972; Kondo and Miyoshi, 1978; Goldman *et al.*, 1978; Boulloud and Charrier, 1980). Chattock (1899) measured current distributions in a single-barb, barbed plate-to-plane geometry and found that, for a fixed total current, the current density profile of the barbed plate was flatter and wider than that of an isolated point. A survey of analytical models of the point-to-plane corona current distribution has been compiled by Sigmond (1986).

More recently, Collins *et al.* (1978) predicted current distributions from a point electrode in a uniform external field and verified their analytical model with measured distributions in a triode electrode geometry. Other work on multi-point corona discharges (Tassicker, 1972; Self *et al.*, 1981) considered only the resulting current distribution on the collector plates and electro-mechanical clamping of the precipitated dust layer.

No data are available on the effects of barb placement, barb length, barb radius of curvature, plate-to-plane spacing or applied voltage on the current distribution in the barbed plate-to-plane geometry. As a first step in the design of a barbed plate for study in the wind tunnel, measurements of ground plane current distributions for four barb patterns with 1 to 9 barbs, barb tip curvature radii from 0.073 mm to 0.567 mm, barb lengths from 5.5 mm to 25.5 mm, and barbed plate-to-plane spacings of 7.62 cm to 12.75 cm are obtained. Spatial distributions of current at the ground plane are visualized through oxidation of the ground plates. Current measurements are compared to those obtained in an isolated point-to-plane geometry. These data are used to select the best barb configuration for final measurements in the wind tunnel. Additional measurements of ground plane current distribution are presented for the final geometry. Appendix A contains a brief discussion of a barbed screen that is also considered a potentially improved electrode.

Results are discussed in terms of applied voltage (V), barb length (ℓ), barb tip-to-plane spacing (L), plate-to-plane spacing ($d = \ell+L$), barb-to-barb spacing (s), barb radius of curvature (r) and barb arrangement as illustrated in Figure 3.1.

4.1.1 Single Barb

Current-voltage (I-V) curves of four barbed plates with a single brass barb (r=0.073 mm) are plotted in Figure 4.1 for a fixed plate-to-plane spacing (d) of 7.62 cm and variable barb lengths (ℓ). As ℓ is increased from 5.5 mm to 20.5 mm, and, consequently, the tip-to-plane spacing (L) is decreased from 7.07 cm to 5.57 cm, current at a given voltage increases.

The effect of the high voltage plate on barb current is shown in the I-V curves of Figure 4.2 taken with barb tip-to-plane spacing (L) fixed at 7.07 cm. Both an isolated point-to-plane and four barbed plates with barb lengths (ℓ) from 5.5 mm to 25.5 mm are shown. The proximity of the high voltage plate to the barb tip limits total current at a given voltage. At 40 kV, for example, the isolated point draws 110 μA. The barbed plate with a 25.5 mm long barb draws 92 μA, but with a shorter 5.5 mm barb draws only 10 μA.

Although the total current is limited by the high voltage plate, the current density distributions plotted in Figure 4.3 show that maximum current (J_0) is unaffected by barb length for a fixed tip-to-plane spacing. Distributions for the isolated point-to-plane and barbed plates are compared to the Warburg distribution with V = 50 kV, L = 7.07 cm and ℓ from 5.5 mm to 25.5 mm. The point-to-plane distribution is the Warburg distribution. In the barbed plate geometries, the tail of the empirical distribution is cut-off at increasingly smaller radii as ℓ is decreased. This effect has also been observed for

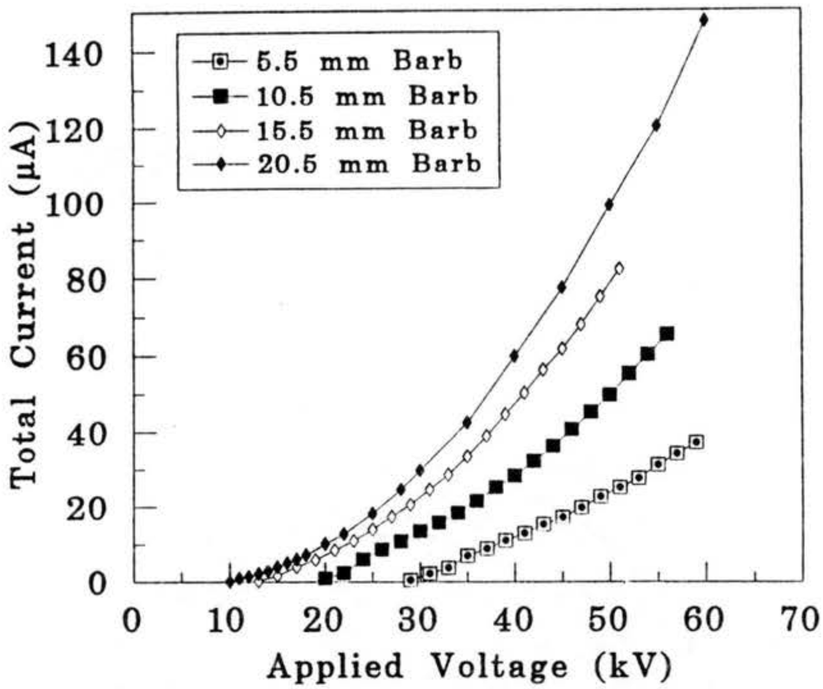

Figure 4.1. Single brass-barb, barbed plate-to-plane I-V curves with r = 0.073 mm, d = 7.62 cm, and ℓ from 5.5 mm to 20.5 mm.

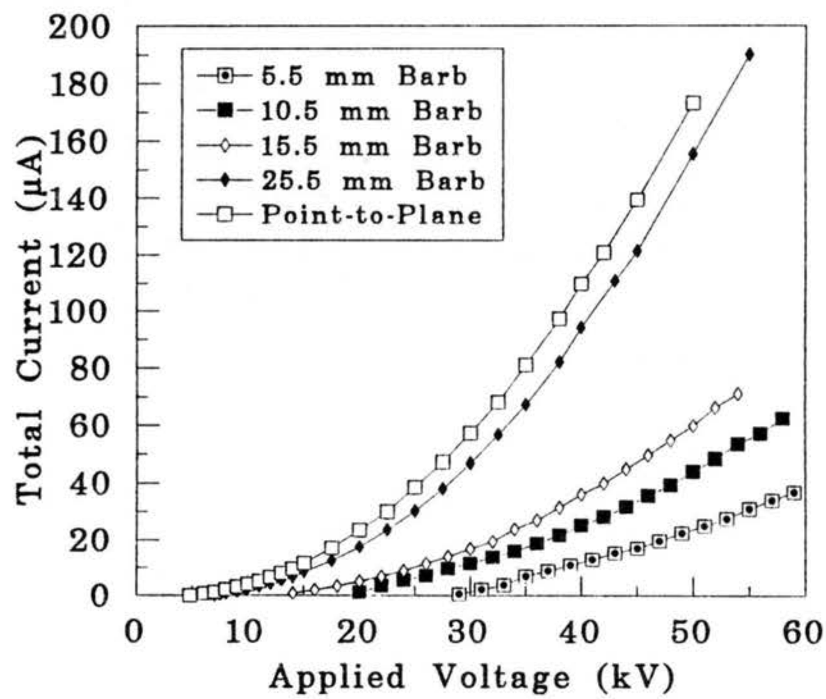

Figure 4.2. Comparison of I-V curves of single brass-barb, barbed plate-to-plane geometries with r = 0.073 mm, L = 7.07 cm, and ℓ from 5.5 mm to 25.5 mm to an isolated point-to-plane with r = 0.073 mm and L = 7.07 cm.

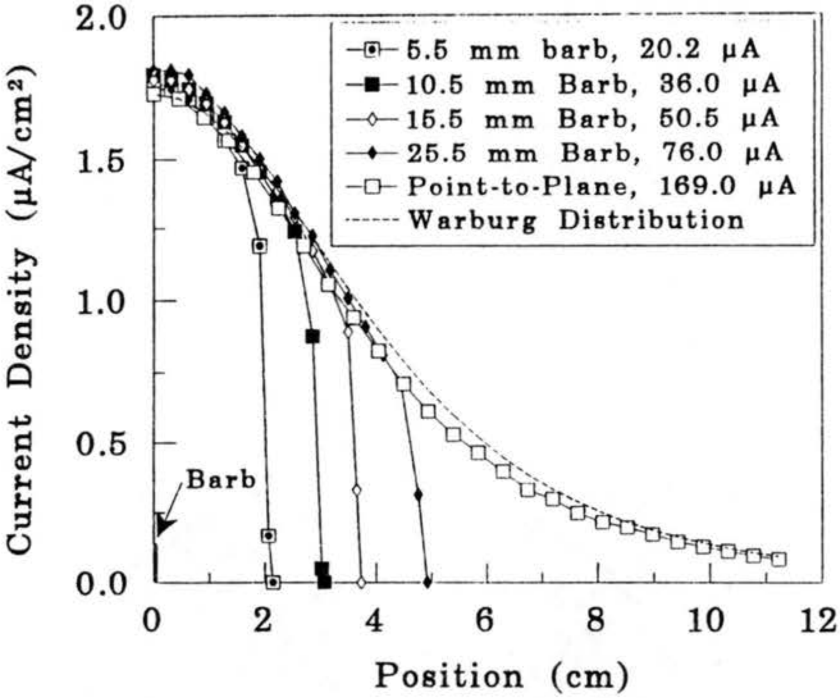

Figure 4.3. Ground plane current density profiles for isolated point-to-plane and single brass-barb, barbed plates with $V = 50$ kV, $r = 0.073$ cm, $L = 7.07$ cm, and ℓ from 5.5 mm to 25.5 mm.

micropoints on a wire where the tuft current distribution area is reduced by the presence of the wire (Lawless *et al.*, 1986; McLean *et al.*, 1986).

Figure 4.4 compares a plot of measured centerline current densities (J_0) obtained in a barbed plate with an ordinary thumb tack barb ($r \approx 0.11$ mm, $\ell = 5.5$ mm) to the saturation current densities (J_s) predicted by Sigmond (1982) as

$$J_s = \beta \varepsilon_0 \frac{V^2}{L^3} . \tag{4.2}$$

Voltage is varied from 34 kV to 55 kV and ß is adjusted for an altitude of 1600 m (determined using the method suggested by Robinson (1973) to be 2.638×10^{-4} m^2/V-s). The plot shows that J_s gives a reasonable estimate of J_0.

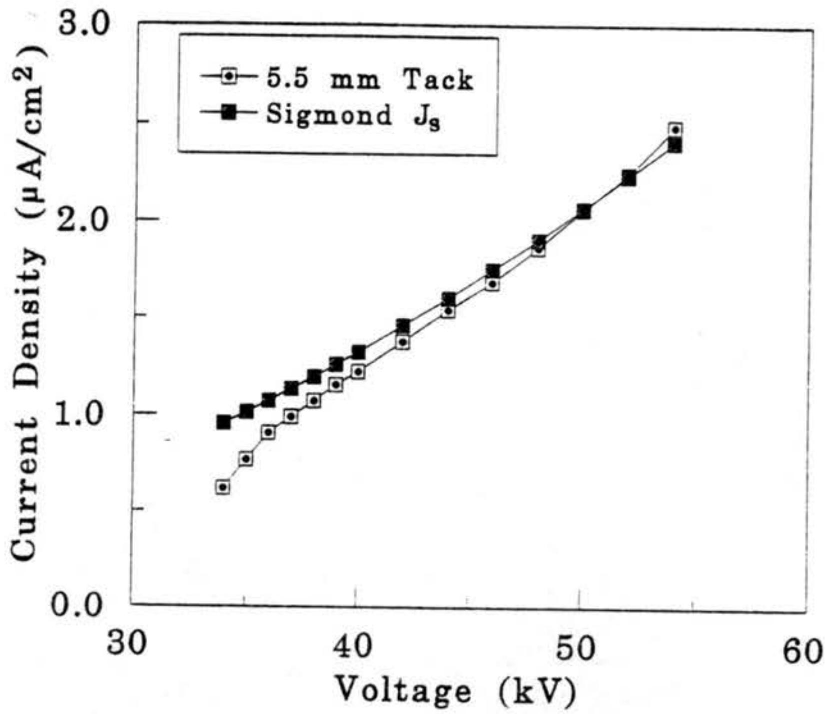

Figure 4.4. J_0 and J_s plotted as functions of V for a thumb tack, barbed plate ($r \approx 0.11$ mm, $\ell = 5.5$ mm) with d = 7.62 cm.

Current density profiles for a barbed plate with a single brass barb (r=0.073 mm) and a plate-to-plane spacing (d) of 7.62 cm are plotted for varying barb lengths (ℓ) in Figure 4.5. The longer barbs draw the highest J_0 (since L is shortest) and produce the widest distribution profile. Figure 4.6 contains the same data but with J normalized by J_0 and position R normalized by L. All profiles fall close to the normalized Warburg distribution up to the "cut-off" radius.

The effect of barb radius of curvature (r) on the current density profiles is shown in Figure 4.7 for a barbed plate with V = 60 kV, d = 7.62 cm, and $\ell = 5.5$ mm. For r from 0.073 mm to 0.269 mm, tip radius has little effect on either J_0 or the "cut-off" radius. A corona discharge could not be initiated with r > 0.567 mm. Sharper barbs draw slightly more current to a wider area. Although the tack radius of curvature is

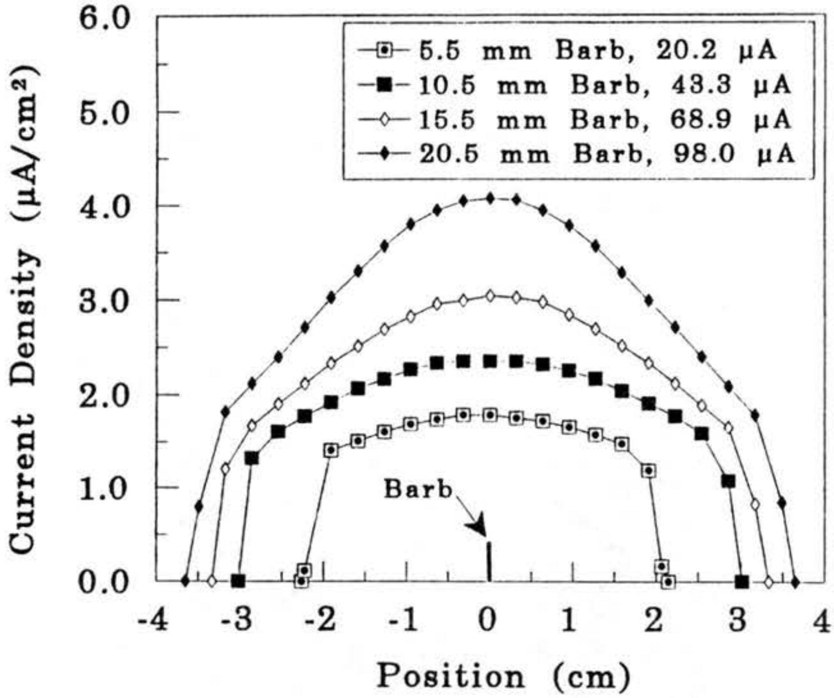

Figure 4.5. Ground plane current density profiles for single brass-barb, barbed plates with V = 50 kV, r = 0.073 mm, d = 7.62 cm and ℓ from 5.5 mm to 20.5 mm.

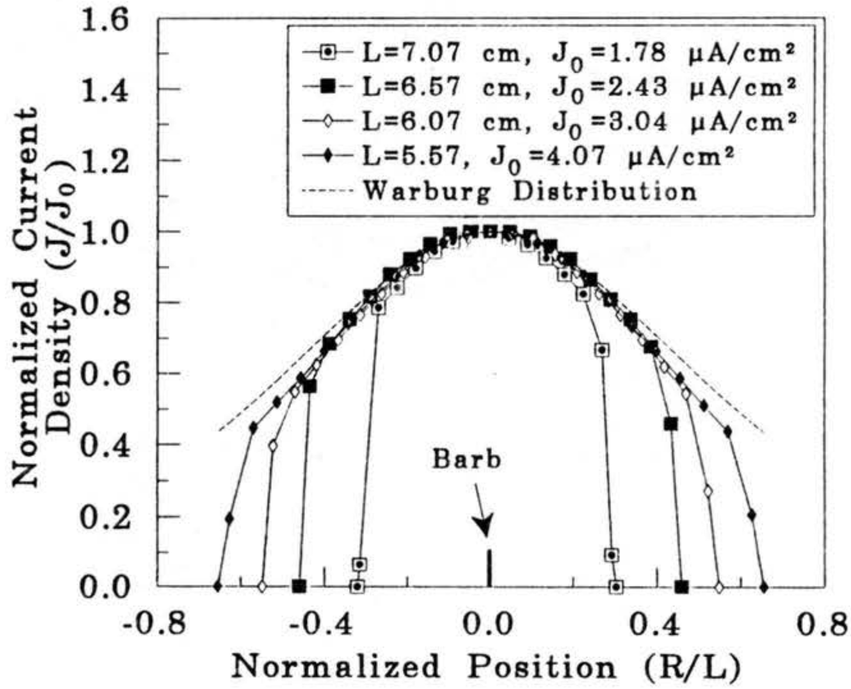

Figure 4.6. Normalized Warburg distribution and ground plane current density profiles for single brass-barb, barbed plates with V = 50 kV, r = 0.073 mm, and d = 7.62 cm.

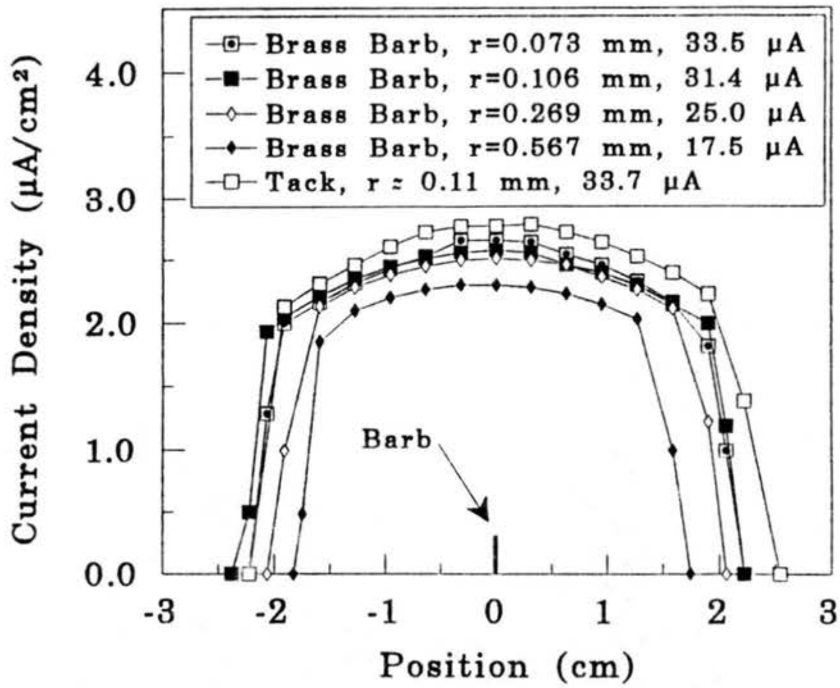

Figure 4.7. Ground plane current density profiles for single-barb, barbed plates with V = 60 kV, d = 7.62 cm, L = 7.07 cm, ℓ = 5.5 mm and r from 0.073 mm to 0.567 mm.

larger than that of the sharpest brass barb, its faceted edges have smaller effective radii and it draws the highest current.

Plots of current density distribution diameter as a function of V and ℓ at a plate-to-plane spacing (d) of 7.62 cm shown in Figure 4.8 reinforce the fact that distribution diameter increases with barb length. The diameter is a weak function of V. As shown in Figure 4.9, the distribution diameter also increases with tip-to-plane spacing (L). The decrease in current with increasing L is therefore due to a decrease in J_0.

4.1.2 Two Barbs

The effect of a nearby barb on discharge distribution is examined by measuring current density profiles of pairs of barbs. Figure 4.10 shows current density profiles beneath the line connecting two barbs (r = 0.073 mm) separated by 2.54 cm at

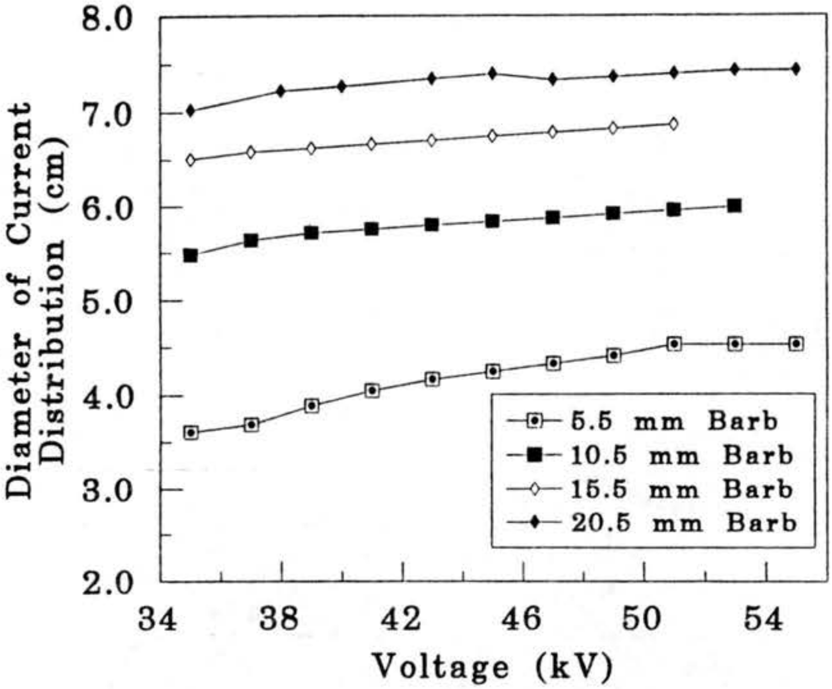

Figure 4.8. Diameter of current density distribution as a function of V for single brass-barb with r = 0.073 mm, d = 7.62 cm and ℓ from 5.5 mm to 20.5 mm.

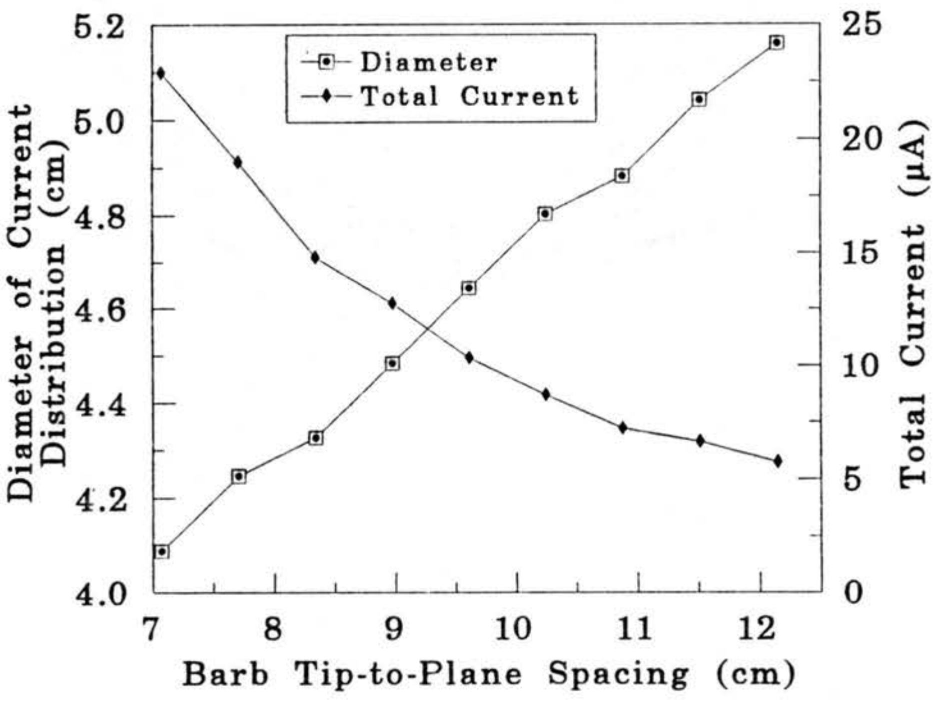

Figure 4.9. Diameter of current density distribution and total current as functions of L for a thumb tack, barbed plate ($r \approx 0.11$ mm, $\ell = 5.5$ mm) with V = 50 kV.

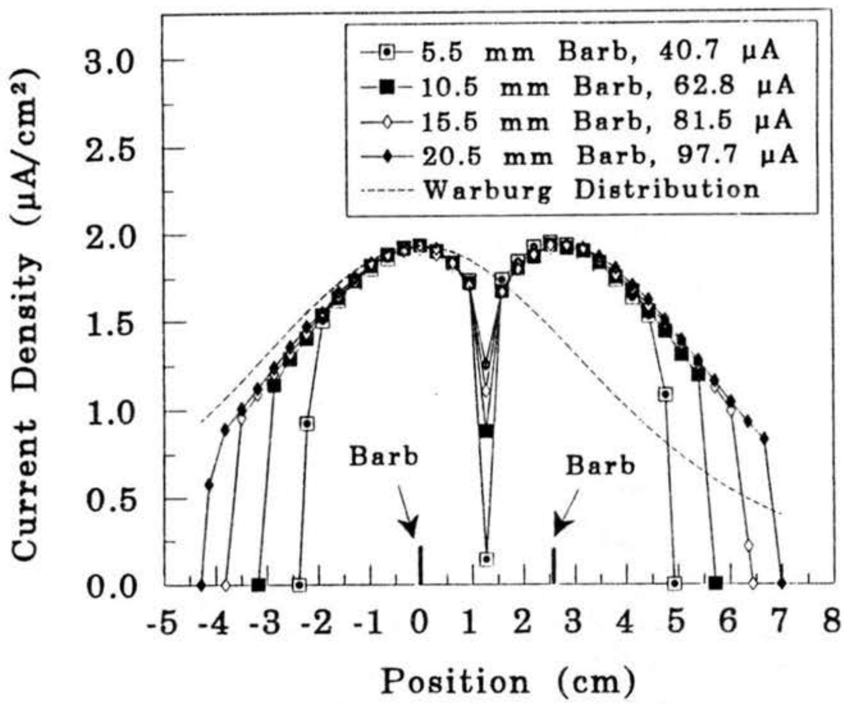

Figure 4.10. Warburg distribution and ground plane current density profiles for two brass-barb, barbed plates with V = 50 kV, r = 0.073 mm, L = 7.07 cm, s = 2.54 cm and ℓ from 5.5 mm to 20.5 mm.

V = 50 kV, L = 7.07 cm and ℓ from 5.5 mm to 20.5 mm. The presence of a nearby barb does not influence J_0 but does limit the radial distance over which the current densities match the Warburg distribution. These data show no discontinuity in current densities between barbs and suggest that the low current region midway between barbs may be raised by increasing barb length. However, since the probe area limits spatial resolution to 6.2 mm^2, smaller areas of zero current cannot be detected.

A striking difference in the shapes of the current distribution areas of single and two-barb geometries is illustrated by comparing the oxidation patterns of Figures 4.11 and 4.12 both obtained with V = 50 kV, r = 0.073 mm, ℓ = 5.5 mm, and L = 7.07 cm. With a single barb, the oxidation pattern shown in Figure 4.11 is circular with a 4 cm diameter.

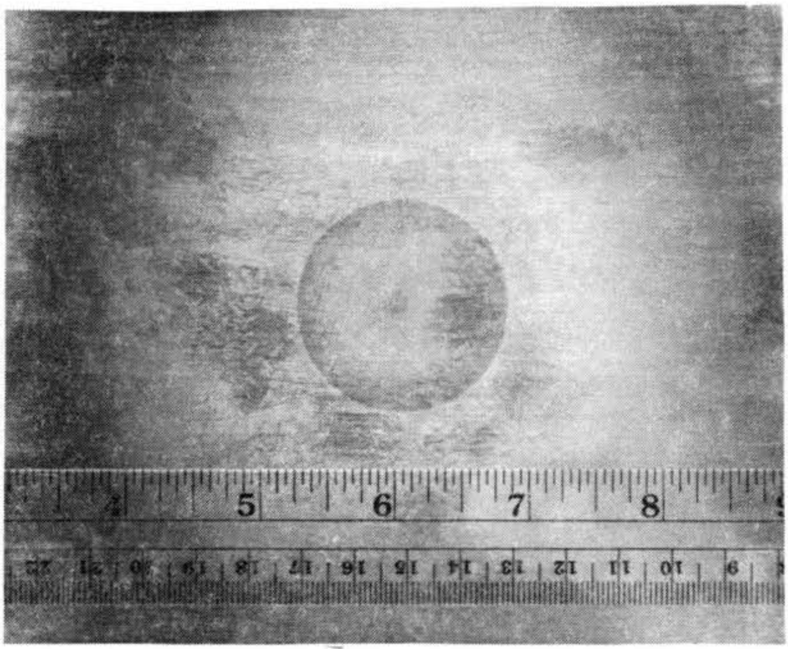

Figure 4.11. Oxidation pattern of single brass-barb, barbed plate with V = 50 kV, r = 0.073 mm, ℓ = 5.5 mm and L = 7.07 cm.

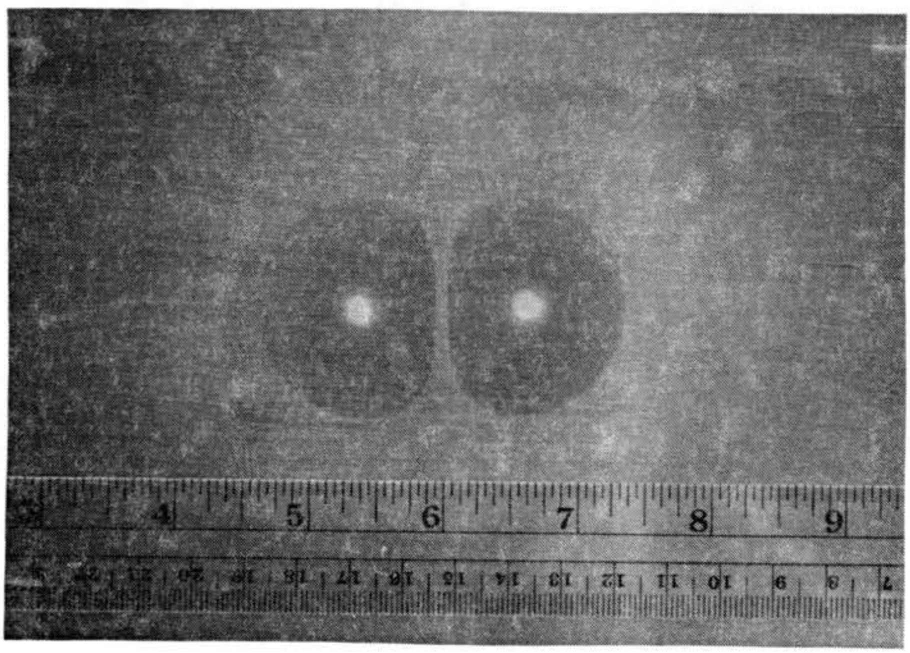

Figure 4.12. Oxidation pattern of two brass-barb, barbed plate with V = 50 kV, r = 0.073, ℓ = 5.5 mm, L = 7.07 cm, and s = 2.54 cm.

With two barbs separated by 2.54 cm, the oxidation pattern of each barb is asymmetrical with a flat edge between barbs. No current is drawn in the 3 mm separation between patterns. The effect of barb length on oxidation pattern is illustrated by comparing the two-barb patterns in Figures 4.12 and 4.13 for $\ell = 5.5$ mm and 20.5 mm, respectively. With a longer barb, the area with current increases and the area without current between barbs narrows.

The current density profiles of Figure 4.14 indicate that reducing the spacing between barbs from $s = 2.54$ cm to $s = 0.635$ cm also reduces the low current area between barbs. There is however a limit to how close barbs can be placed and still discharge (Malik *et al.*, 1983).

4.1.3 Multiple Barb Patterns

Two possible barb arrangements for a barbed plate are examined. In both cases, the barbs are ordinary thumb tacks ($r \approx 0.11$ mm and $\ell = 5.5$ mm). Figure 4.15 is a three-dimensional plot of the current distribution pattern for nine barbs arranged in a square grid at 2.54 cm intervals and operated at $V = 50$ kV ($I = 97.0$ μA). Each line-crossing represents a measured current density. Figure 4.16 is the oxidation pattern obtained under the same conditions. Both figures indicate clearly the regions of no current between barbs and show sharp transitions from zones with current to those without. Again, the maximum current density (J_0) of an individual barb is not affected by the presence of surrounding barbs and J_0 for all barbs ≈ 1.9 μA/cm^2. However, the shrinkage of current density distribution area noted with two barbs is even more evident in the relatively small diameter oxidation pattern of the center barb as compared to those

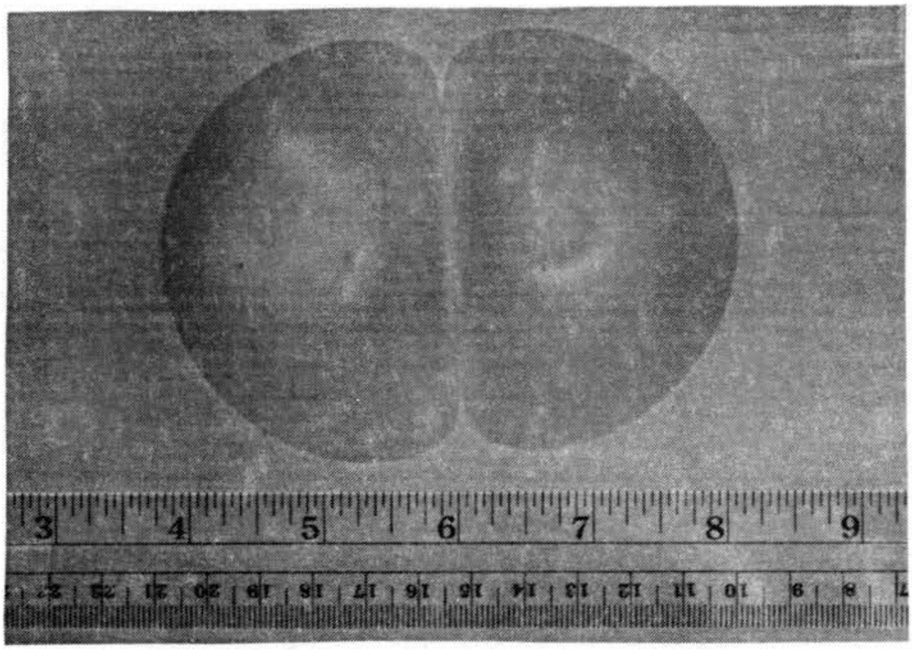

Figure 4.13. Oxidation pattern of two brass-barb, barbed plate with V = 50 kV, r = 0.073 mm, ℓ = 20.5 mm, L = 7.07 cm, and s = 2.54 cm.

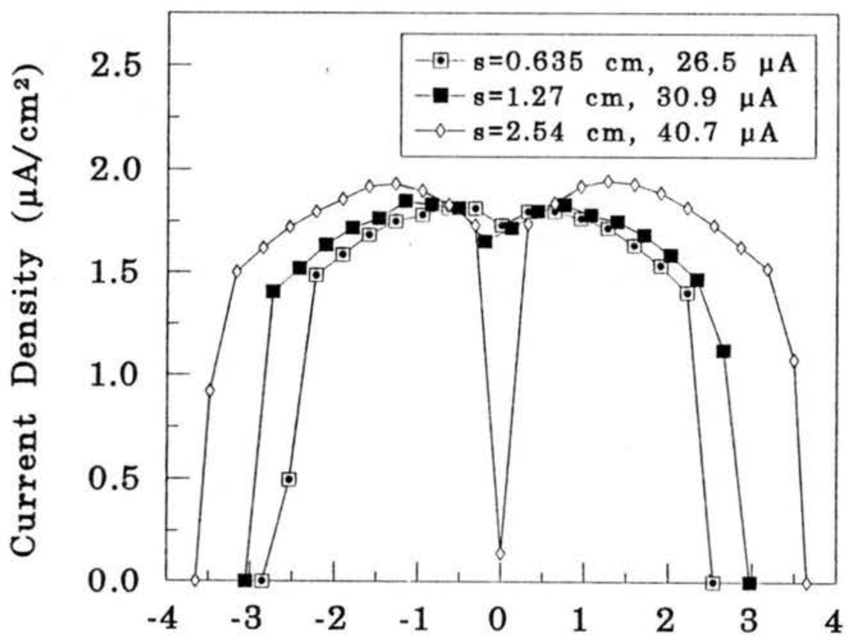

Figure 4.14. Ground plane current density profiles for two brass-barb, barbed plates with V = 50 kV, r = 0.073 mm, ℓ = 5.5 mm, L = 7.07 cm, and s = 0.635 cm to 2.54 cm.

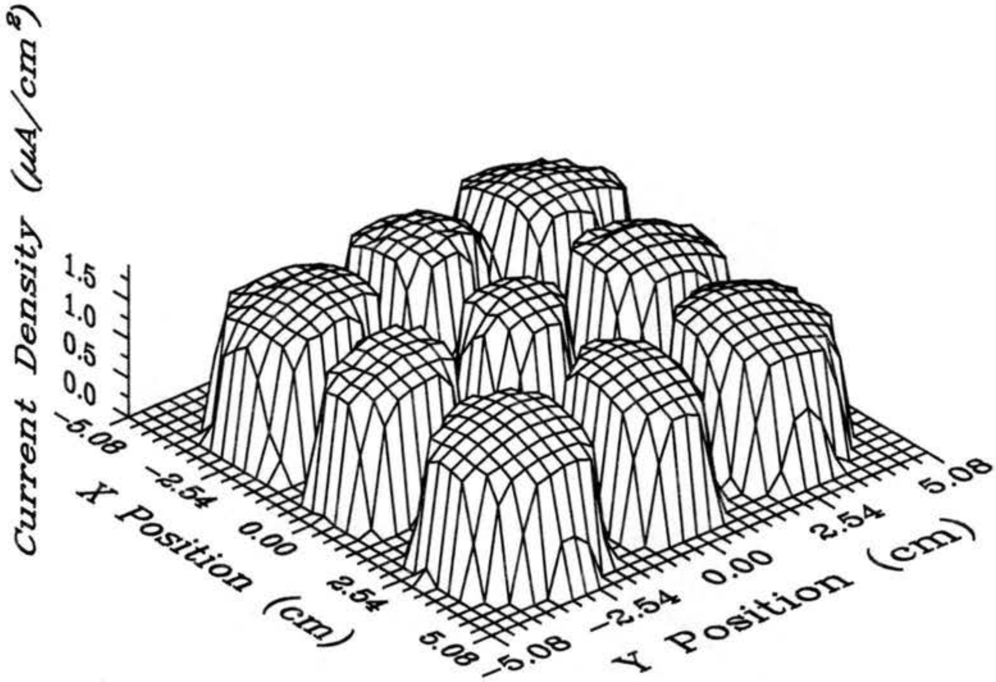

Figure 4.15. Ground plane current density distribution pattern for the nine-barb, square grid, barbed plate, with V = 50 kV, r ≈ 0.11 mm, ℓ = 5.5 mm, L = 7.07 cm, and s = 0.635 cm to 2.54 cm.

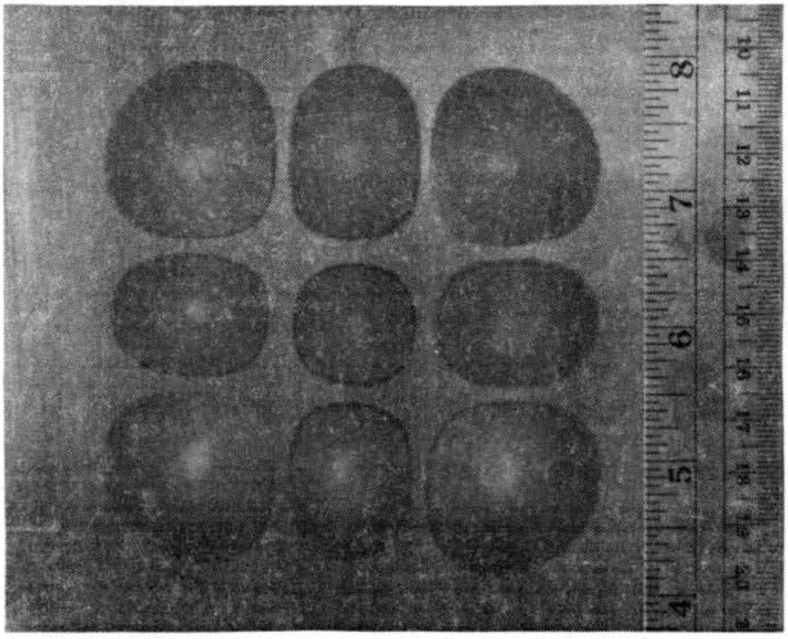

Figure 4.16. Oxidation pattern of the nine-barb, square grid, barbed plate, with V = 50 kV, r ≈ 0.11 mm, ℓ = 5.5 mm, L = 7.07 cm, and s = 2.54 cm.

of the 8 edge barbs. The diameter of the oxidized area associated with the center barb is 2.4 cm compared to 3.0 cm for the single-barb shown in Figure 4.11.

Figures 4.17 and 4.18 are analogous to Figures 4.15 and 4.16, but for a seven-barb, hexagonal-grid with s = 2.70 cm. The data show the same overall trends: zones with no current exist between barbs; J_0 is constant at ≈ 1.9 μA/cm2 (although with 7 barbs total current is reduced to 83.0 μA); and the central barb draws current to the smallest area, 2.5 cm in diameter compared to 2.4 cm in the square-grid.

To assess the effectiveness of these geometries in reducing current nonuniformities in precipitators, only the center barb need be considered since with a repeated pattern, edge barbs would have little effect on overall performance. Table 4.1 compares electrical characteristics of the central barb in the multiple-barb plates. The effective area of the central barb in each grid is depicted by the hatched areas in Figure 4.19, and is 6.45 cm^2 for the square-grid and 6.31 cm^2 for the hexagonal-grid. The total current drawn by the central barb divided by the effective area gives an estimate of the average current density in a large array and is 1.11 $\mu A/cm^2$ in the square-grid compared to 1.18 $\mu A/cm^2$ in the hexagonal-grid.

Numerical integration of the data in Figures 4.15 and 4.17 shows that the square-grid center barb produces current densities ≥ $^1/_{10}$ of J_0 over 81.4% of the effective area and ≥ $^1/_2$ of J_0 over 59.2% of the area. In comparison, the hexagonal-grid center barb covers 87.3% of its effective area with current densities ≥ $^1/_{10}$ of J_0 and covers 62.8% of the area with current densities ≥ $^1/_2$ of J_0. The superior current uniformity of the hexagonal-grid is underscored by the fact that only 60.9% of the square-grid hatched area is oxidized while 70.3% of the hexagonal-grid hatched area is oxidized.

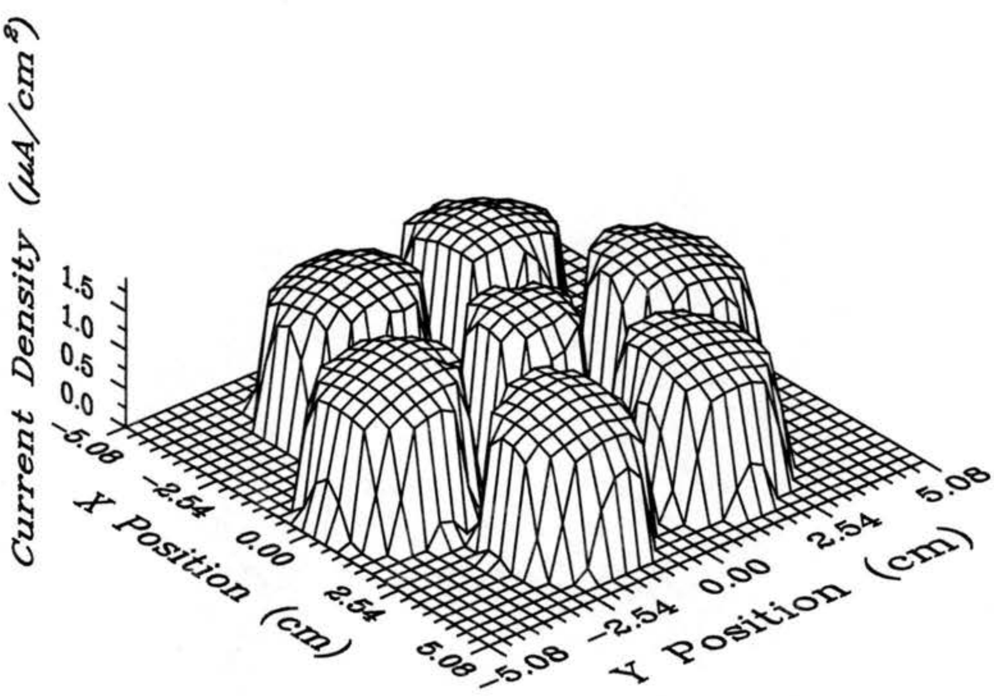

Figure 4.17. Ground plane current density distribution pattern for the seven-barb, hexagonal grid, barbed plate, with V = 50 kV, r ≈ 0.11 mm, ℓ = 5.5 mm, L = 7.07 cm, and s = 2.70 cm.

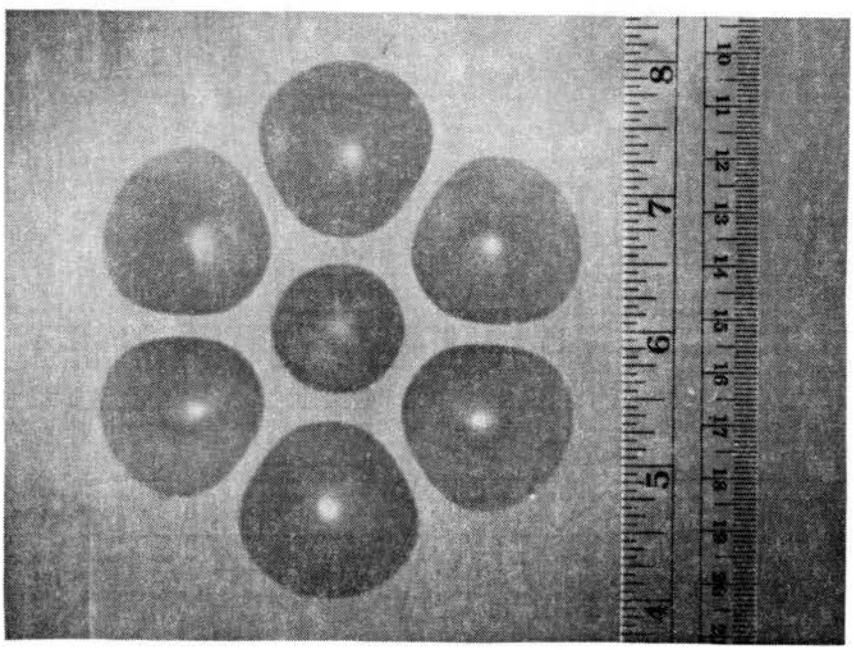

Figure 4.18. Oxidation pattern of the seven-barb, hexagonal grid, barbed plate, with V = 50 kV, r ≈ 0.11 mm, ℓ = 5.5 mm, L = 7.07 cm, and s = 2.70 cm.

Table 4.1. Comparison of multiple-barb grids.

	Square Grid	Hexagonal Grid
J_0 (μA/cm^2)	1.91	1.88
Effective Area (cm^2)	6.45	6.31
I/Barb (μA)	7.16	7.43
Average J (μA/cm^2)	1.11	1.18
Percent of Effective Area With $J \geq 0.1 \times J_0$	81.4%	87.3%
Percent of Effective Area With $J \geq 0.5 \times J_0$	59.2%	62.8%
Percent of Effective Area Oxidized	60.9%	70.3%

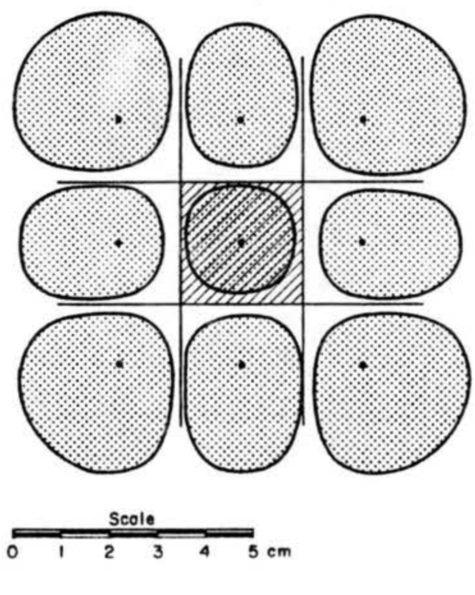

(a)

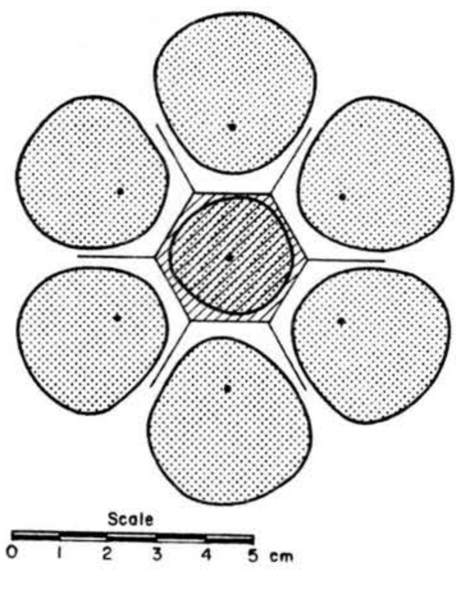

(b)

Figure 4.19. Sketch of current density distribution with overlay of center barb effective area; (a) nine-barb, square grid, s = 2.54 cm; (b) seven-barb, hexagonal grid, s = 2.70 cm: V = 50 kV, r ≈ 0.11 mm, ℓ = 5.5 mm, and L = 7.07 cm.

4.1.4 Summary of Preliminary Barbed Plate Design Measurements

Measurements at the ground plane of barbed plate-to-plane electrode geometries show that with a single barb, barb length and barb tip-to-plane distance are the controlling geometric factors in establishing current density distribution. As expected, centerline current density is solely a function of barb tip-to-plane distance and applied voltage. Barb tip radius has little effect on the centerline current density or current spread. Current density distributions follow the classic point-to-plane Warburg distribution except that the presence of a high voltage plate behind the barb limits the total current by truncating the tail. This reduction in distribution area is probably due to a compression of the electric field lines that would exist in an isolated point discharge. For a fixed barb tip-to-plane spacing, distribution area increases and maximum current density remains constant when the barb length is increased by increasing the plate-to-plane spacing. For a given barb length, discharge area increases but maximum current density and total current decrease with increasing tip-to-plane spacing. However, if the plate-to-plane distance is fixed, any increase in the barb length increases the area with current even though the tip-to-plane distance is reduced. In this case, maximum current density goes up.

In multiple barb geometries, current distributions are limited in area by the presence of neighboring barbs but centerline current densities are constant for all barbs regardless of barb spacing. Longer barbs and closer barb spacings reduce the regions of zero current between barbs. In precipitators, long barbs may, however, contribute to gas sneakage along the high voltage plate. Both square and hexagonal barb arrangements are considered as retrofit geometries for industrial precipitators. Based on visual oxidation patterns and a comparison of current coverage on the ground plane, the hexagonal pattern is preferable.

4.1.5 Final Design of Barbed Plate

Having concluded that the hexagonal barb pattern is the preferable barb arrangement and that barb tip radius and applied voltage have little effect on the current distribution, a series of experiments are performed to select the proper barb spacing and length. A special high voltage test plate is constructed for the *X-Y* traverse and mounted 15.24 cm from the ground plane (the wind tunnel test section width). The plate contains a series of holes which accommodate 7 barbs of any length in a hexagonal pattern at spacings from 5 mm to 30 mm. Ground plate current density profiles are measured for twenty different barb length and spacing combinations for barb lengths from 5.5 to 25.5 mm and barb spacings from 10 to 30 mm. Barb tip radius is 0.073 mm and voltage is 80 kV. Each profile is measured across a line directly below three barbs.

Figure 4.20 is a three-dimensional plot of the minimum current density measured between the barbs for each configuration. Because the probe has a finite radius of 2.5 mm, an average current density greater than zero is almost always measured between the barbs. A high "minimum" value provides an indication of a very narrow region of no current between the barbs and therefore a more uniform overall current distribution. The data of Figure 4.20 indicate that longer barbs and more closely spaced barbs promote a more uniform current distribution at the ground plane. However, as barbs are moved closer together, not all barbs discharge. This phenomenon is particularly true for shorter barbs (e.g. 5.5 mm barbs at the 10 mm spacing). Figure 4.21 is a plot of the maximum current density, J_0, (directly below the center barb) corresponding to the data of Figure

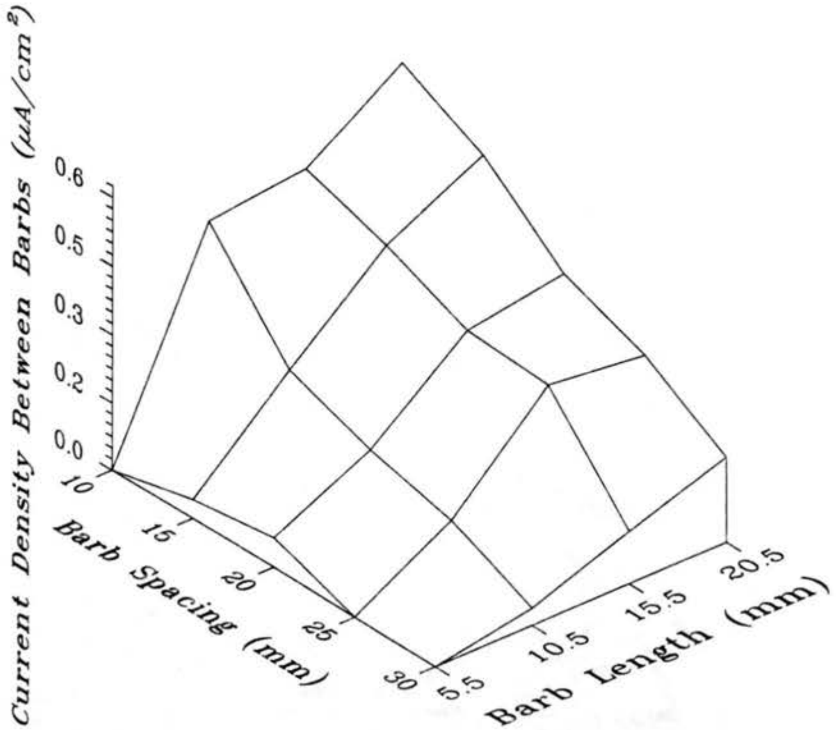

Figure 4.20. Barbed plate minimum ground plate current density measured between barbs, with V = 80 kV, d = 15.24 cm, and r = 0.073 mm.

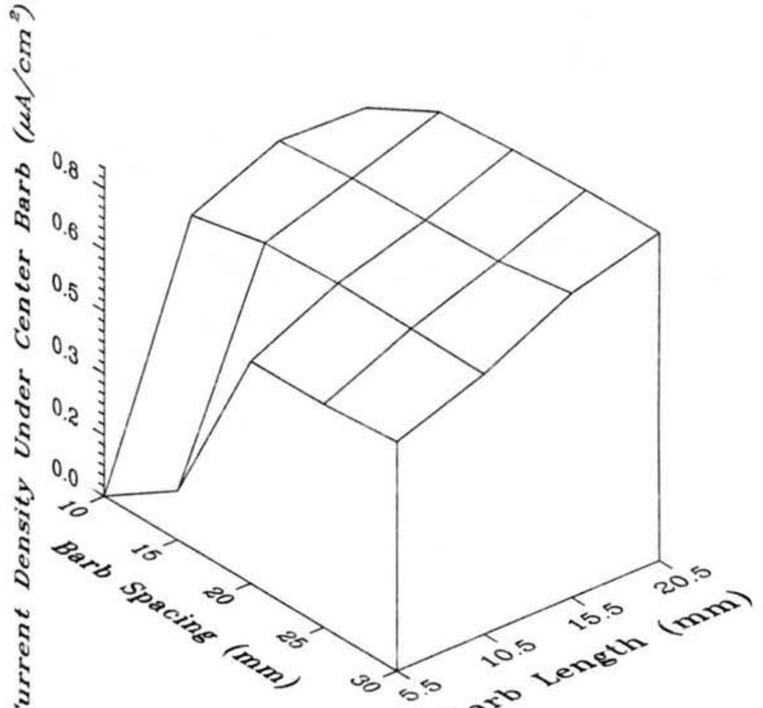

Figure 4.21. Barbed plate maximum ground plate current density measured across from barb tip.

4.21 and shows that 5.5 mm barbs at spacings of 10 and 15 mm do not fully discharge. Additionally, overly long barbs may promote gas sneakage in the precipitator because of the lack of ions behind the barb tips. Earlier work by Davidson and McKinney (1989) indicates that a hexagonal pattern of 3.2 mm barbs spaced at 27.0 mm discharges well for a 7.62 plate-plate spacing. This is supported by the data of Figures 4.20 and 4.21 and is the basis for the design barb spacing of 27.0 mm. A barb length of 15.9 mm is selected so that a reasonably uniform current density may be maintained without using overly long barbs.

4.2 Comparison of Current Densities in the Barbed Plate-to-Plate and Wire-Plate Geometries

Differences in electrical characteristics of barbed plate-to-plate and wire-plate precipitators are presented in terms of measured current-voltage curves and spatial distributions of current at the collection plate. Data are obtained in both the *X-Y* traversing plane and in the 61.0 cm by 61.0 cm by 15.2 cm laboratory precipitator operating at a Reynolds number,

$$\mathrm{Re} = \frac{\rho U d}{\mu}, \tag{4.3}$$

and electrohydrodynamic number,

$$N_{EHD} = \frac{I d}{\beta \rho U^2 A}\ , \tag{4.4}$$

typical of industrial precipitators. Using values representative of fly ash wire-plate precipitators operated at 300 ^{o}C at sea level as shown in Table 4.2, Re = 7400 and

$N_{EHD} = 1$. At environmental conditions in the laboratory (also shown in Table 4.2), equivalent values of Re and N_{EHD} are obtained with an average current density of 1.6 mA/m^2 and an air speed of 1 m/s. Since only the interior portion of the laboratory precipitator is equivalent to a full-scale precipitator (in which edge effects are negligible), operating points are chosen to approximate this average current density over the center section of the ground plates. In the wire-plate precipitator, V = 34 kV and I = 1.2 mA. In the barbed plate precipitator, V = 56 kV and I = 0.6 mA. Both voltages are negative. The differences in operating points result from the difference in electrode-to-ground plate spacing and number of collection plates. To operate the barbed plate with nearly all of the barbs discharging, additional data are obtained at twice the nominal current density (3.2 mA/m^2), yielding $N_{EHD} = 2$.

Table 4.2. Dimensionless parameters for industrial and laboratory precipitators.

Name	Units	Industrial Precipitator	Lab (N_{EHD}≈1)	Lab (N_{EHD}≈2)
Pressure	Pa = N/m^2	101,000	80,800	80,800
Air Temperature	degrees C	275	22.5	22.5
Current Density	mA/m^2	0.7	1.6	3.2
Plate Spacing	m	0.35	0.15	0.15
Gas Velocity	m/s	1	1	1
Gas Viscosity	N-s/m^2	2.80e-05	1.81e-05	1.81e-05
Gas Density	kg/m^3	0.64	0.95	0.95
Ion Mobility	m^2/V-s	3.9e-04	2.64e-04	2.64e-04
Reynolds Number		8027	8021	8021
N_{EHD} Number		0.97	0.97	1.94

4.2.1 Current-voltage curves

Negative corona current-voltage characteristics of the two geometries are compared in Figure 4.22. Onset voltages for the wire-plate and barbed plate are approximately 20 kV. At $N_{EHD} = 1$ in the wire-plate precipitator, I = 1.2 mA, V = 34 kV and E = 4.5

kV/cm. At $N_{EHD} = 2$, I = 2.4 mA, V = 40 kV and E = 5.3 kV/cm. In the barbed plate-to-plate precipitator, at $N_{EHD} = 1$, I = 0.6 mA, V = 56 kV and E = 4.1 kV/cm. At $N_{EHD} = 2$, I = 1.2 mA, V = 68 kV and E = 5.0 kV/cm. Visually, the discharge along the wires consists of individual corona tufts. Thus, in addition to large scale current inhomogeneities due to the spacing between wires, a smaller scale nonuniformity exists along the wires. The barbed plate has some degree of nonuniformity due to barb spacing and unequal current flow from the barbs. Some of the difference in current level is attributed to slight differences in barb length and the condition of the tips. With a barb-to-barb spacing of 27 mm, not all of barbs have a visible discharge. At $N_{EHD} = 1$, approximately 1/2 of the barbs appear to discharge. At $N_{EHD} = 2$, the number of discharging barbs increases to 3/4 of the total.

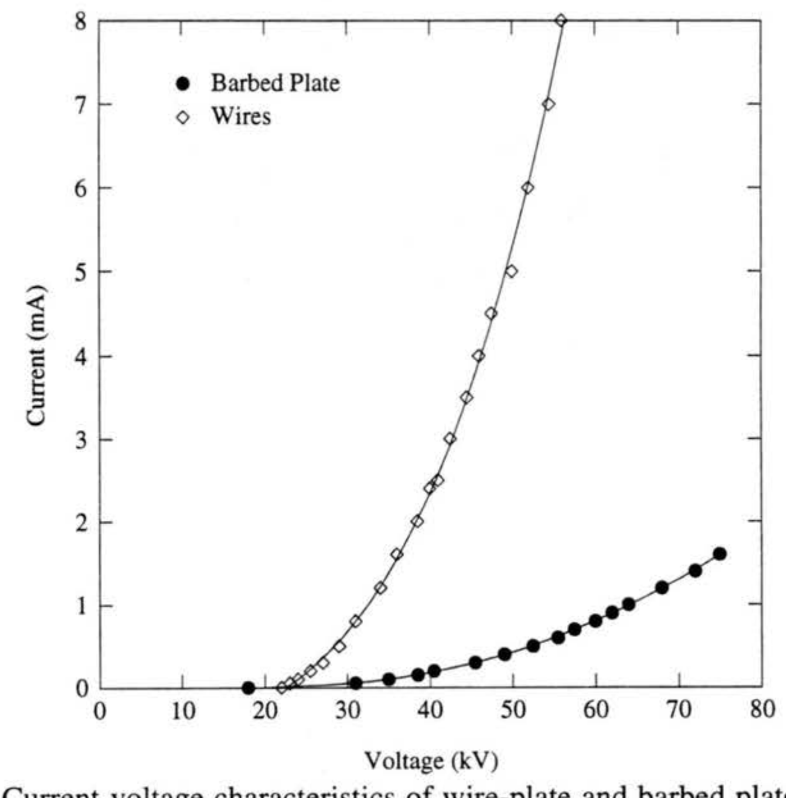

Figure 4.22. Current-voltage characteristics of wire-plate and barbed plate precipitators.

4.2.2 High Resolution Current Density Distributions

Current density measurements obtained with the *X-Y* traversing plane are presented in Figures 4.23 through 4.28. Figures 4.23 and 4.24 show only the current density along the portion of the ground plate affected by the middle wire in the 3-wire arrangement (normal to the wire extending 7.6 cm to either side of it) and a corresponding area under 5 interior barbs. To illustrate the variability of the current density along the wire, two profiles under the wire are shown. Current density in the wire-plate geometry varies both spatially and temporally. Corona tufts change position along the wire, resulting in a continuously changing current distribution. The temporal variation of current density in the wire-plate geometry obscures regions of zero current at the ground plane which must exist between wires and tufts.

Data in Figure 4.23 are measured at 34 kV in the wire-plate geometry and at 56 kV in the barbed plate geometry (these operating conditions correspond to $N_{EHD} = 1$ in the wind tunnel). Although the discharge in the barbed plate geometry is stable, one barb discharges at a lower current than the surrounding barbs. This result confirms visual observations in the wind tunnel that not all barbs discharge. Although barb tip radius and applied voltage have little effect on the spatial distribution of current from a discharging barb, both can affect the onset of corona. The absence of a discharge on every barb has a negative impact on the uniformity of current distribution. However, even with one barb discharging at a lower current, the barbs appear to produce a larger region of uniform current density along the ground plate than do the wires.

Data in Figure 4.24 are acquired at 40 kV in the wire-plate geometry and 68 kV in the barbed plate geometry (corresponding to $N_{EHD} = 2$ in the wind tunnel). At the

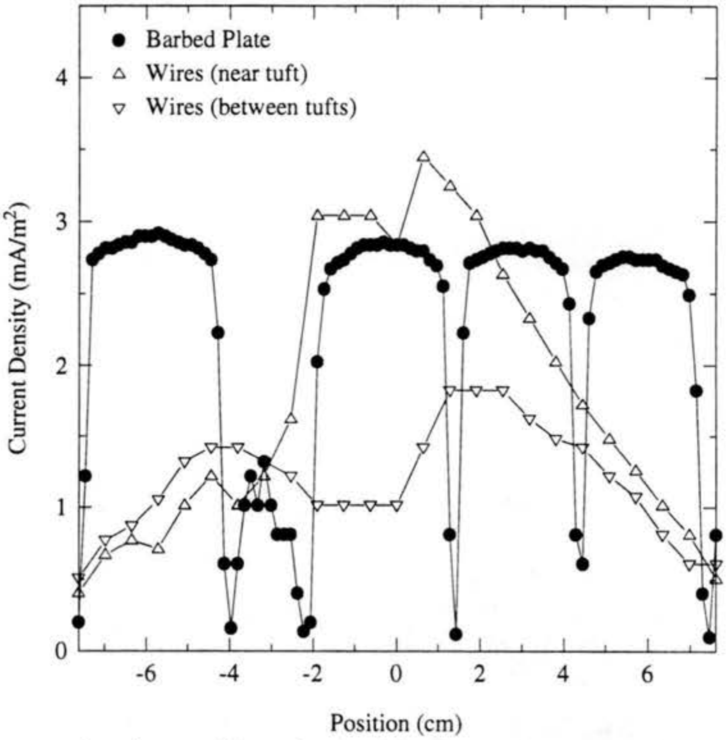

Figure 4.23. Current density profiles obtained in the *X-Y* traverse for the wire-plate and barbed plate geometries at $N_{EHD} = 1$.

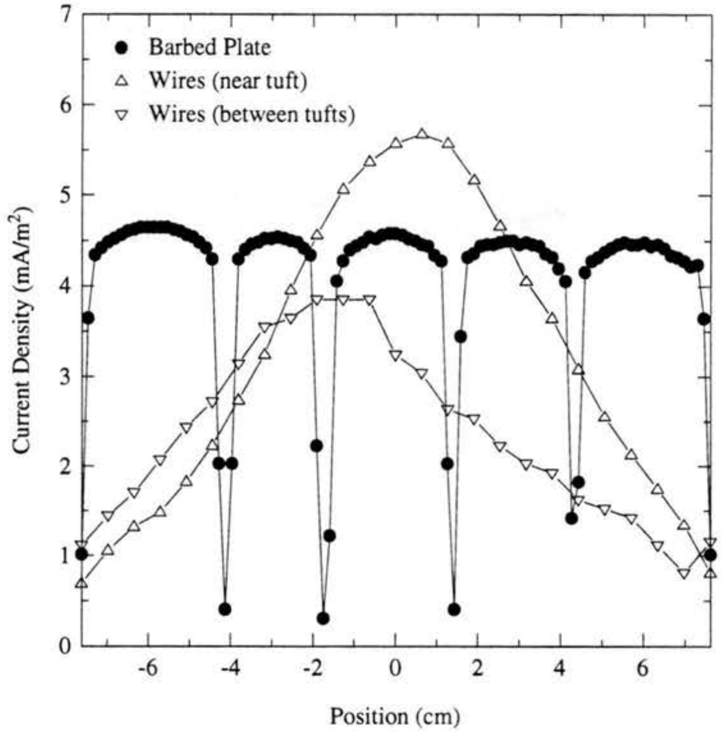

Figure 4.24. Current density profiles obtained in the *X-Y* traverse for the wire-plate and barbed plate geometries at $N_{EHD} = 2$.

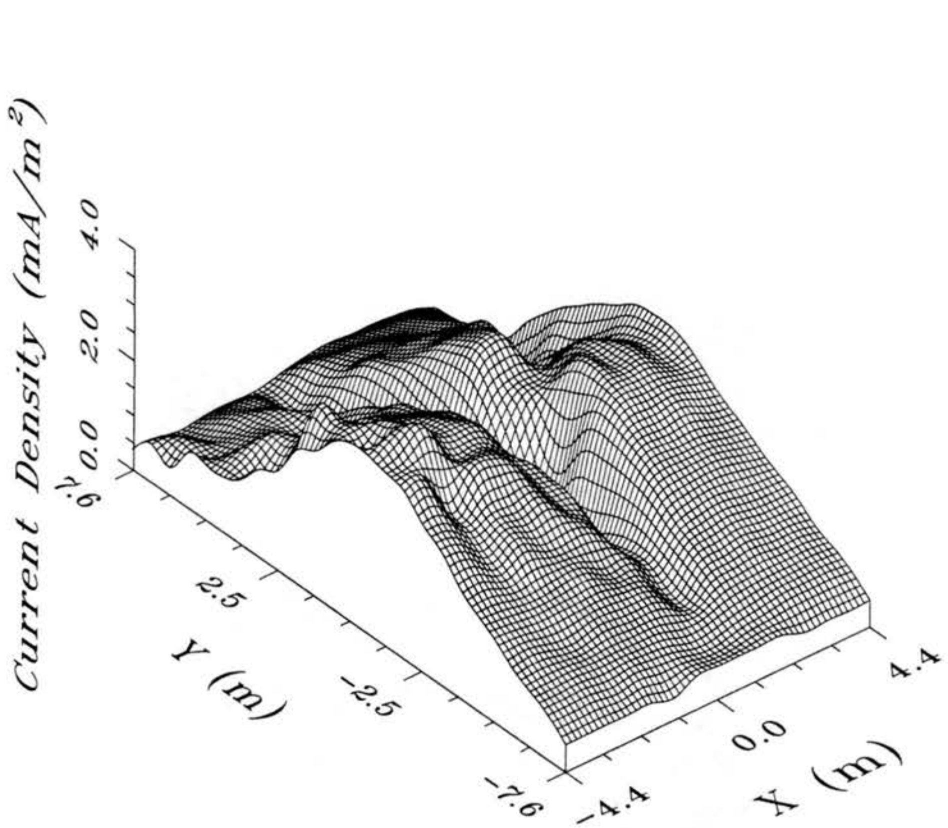

Figure 4.25. Current density distribution obtained in the *X-Y* traverse for the wire-plate geometry at N_{EHD} = 1.

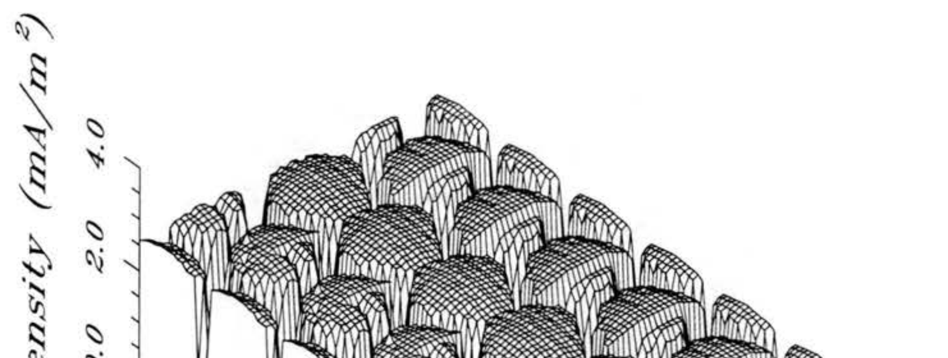

Figure 4.26. Current density distribution obtained in the *X-Y* traverse for the barbed plate geometry at N_{EHD} = 1.

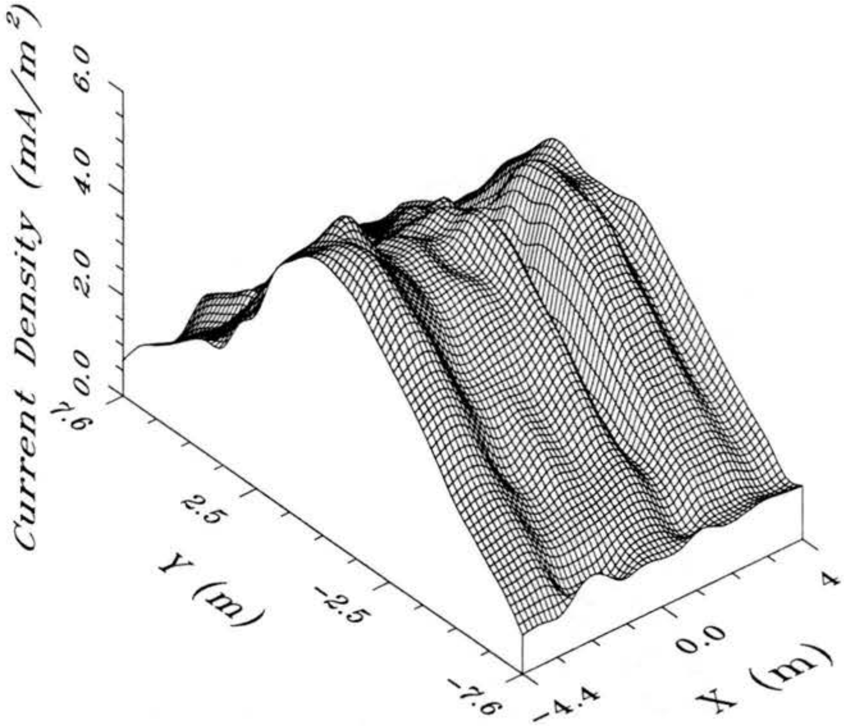

Figure 4.27. Current density distribution obtained in the *X-Y* traverse for the wire-plate geometry at $N_{EHD} = 2$.

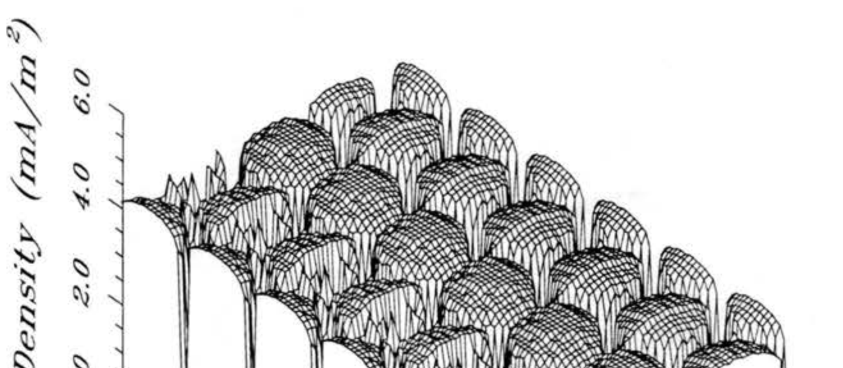

Figure 4.28. Current density distribution obtained in the *X-Y* traverse for the barbed plate geometry at $N_{EHD} = 2$.

higher voltage, the barb at -3 cm discharges with almost the same strength as the surrounding barbs. As in Figure 4.23, it appears that the barbs produce a more uniform distribution.

Figures 4.25 through 4.28 are 3-dimensional plots of the current density obtained at voltages equal to those used to obtain the data plotted in Figures 4.23 and 4.24. Data of Figures 4.25 and 4.27 and are obtained at 6.4 mm intervals and are fit with splines to estimate values at 1.6-mm intervals. The plots clearly show the variation in current density along the length of the wire (which runs in the X-direction). Current density measurements in the barbed plate geometry are taken over a 2.7 cm by 9.4 cm area in 1.6 mm intervals. To provide an image of similar size to that of Figures 4.25 and 4.27, the data are duplicated 5 times in the Y-direction and plotted in Figures 4.26 and 4.28. Comparison of Figures 4.25 and 4.27 to Figures 4.26 and 4.28 provides dramatic evidence that current density distribution in the barbed plate geometry is more uniform than in the conventional wire-plate geometry.

Table 4.3 lists statistics of the data shown in Figures 4.25 through 4.28. The mean, root-mean-square (rms), minimum and maximum values of current density, rms as a percentage of the mean, and percentages of the ground plate area which receive within ±10%, ±20%, ±30%, ±40%, and ±50% of the mean current density are computed. Although rms current density of the barbed plate is greater than the rms value of the wire-plate geometry, portions of the ground plate area over which current densities are within ±40% and ±50% of the mean are greater for the barbed plate at $N_{EHD} = 1$ than for the wire-plate. At $N_{EHD} = 2$, current densities within ±30%, ±40%, and ±50% of the mean cover at least twice the ground plate area in the barbed plate geometry. This analysis confirms the visual impression of Figures 4.23 through 4.28 that current distribution in the barbed-plate geometry is uniform over a much larger area than that in the wire-plate geometry.

Table 4.3. Current distributions obtained with the *X-Y* traverse.

	$N_{EHD} = 1$ Barbed Plate	$N_{EHD} = 1$ Wires	$N_{EHD} = 2$ Barbed Plate	$N_{EHD} = 2$ Wires
Operating Parameters:				
Applied Voltage (kV)	56	34	68	40
Mean Electric Field (kV/cm)	4.1	4.5	5.0	5.2
Current Density Statistics (mA/m^2):				
Mean	2.0	1.6	3.4	2.9
rms	1.0	0.8	1.4	1.3
Min	0.0	0.3	0.1	0.7
Max	2.8	3.4	4.5	5.7
rms/mean*100 (%)	50	50	41	45
Percent of ground plate area with current density within given percent of mean:				
±10%	6	11	9	12
±20%	12	24	20	24
±30%	33	37	69	37
±40%	77	51	81	53
±50%	79	64	84	69

4.2.3 Oxidation Patterns on the *X-Y* Traverse

A visual comparison of ground plane current density distribution is made by creating a copper plate oxidation pattern for each electrode as was done in the barbed plate design phase, reported in Section 4.1. In this case, a 61.0 by 61.0 cm copper plate is placed on the *X-Y* traversing ground plate and allowed to oxidize for approximately 24 hours under each of the two operating conditions ($N_{EHD} = 1$ and $N_{EHD} = 2$). Figures 4.29 through 4.32 are photographs of the results. Figure 4.29 is the pattern created by

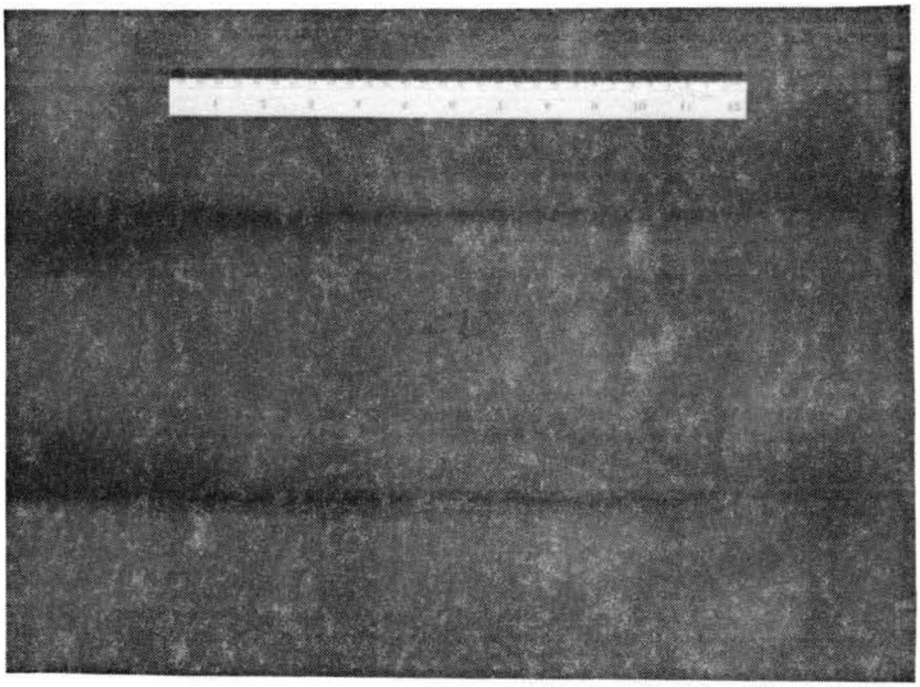

Figure 4.29. Oxidation pattern for wire-plate precipitator operating at $N_{EHD} = 1$.

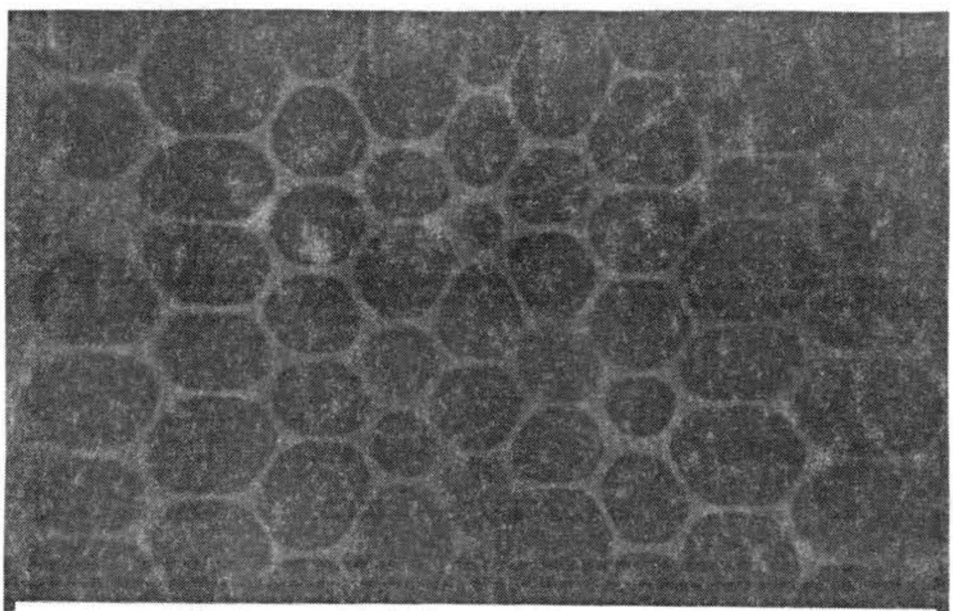

Figure 4.30. Oxidation pattern for barbed plate precipitator operating at $N_{EHD} = 1$.

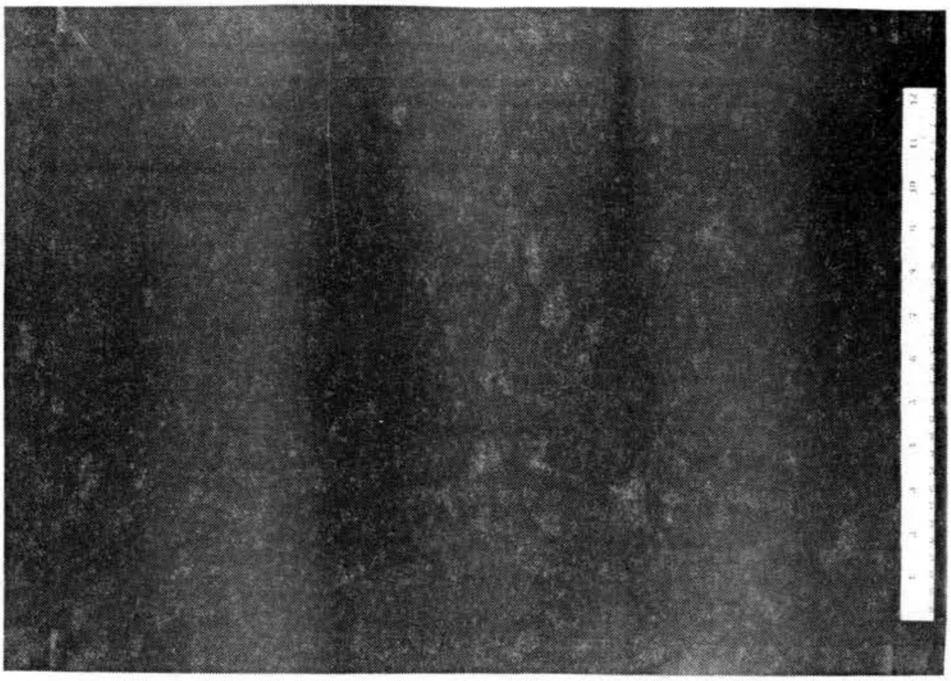

Figure 4.31. Oxidation pattern for wire-plate precipitator operating at $N_{EHD} = 2$.

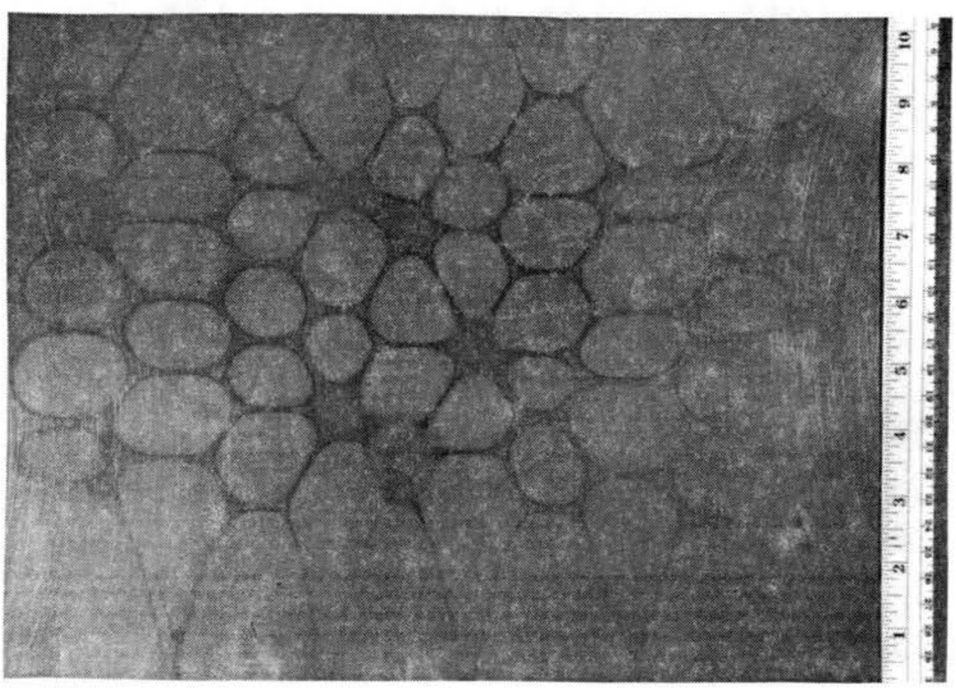

Figure 4.32. Oxidation pattern for barbed plate precipitator operating at $N_{EHD} = 2$.

the wire-plate geometry at 34 kV ($N_{EHD} = 1$) and shows clearly the three oxidized strips under the three wires as well as lines of no current that exist between wires. Additionally, zones of zero current between corona tufts can be seen as the shorter curving lines that appear along the length of each of the three oxidized strips. These zones are not as clearly defined because corona tufts are not stable. Figure 4.30 is an oxidation pattern analogous to that of the wire-plate but for the barbed plate geometry. This figure shows defined regions of current for each barb. These patterns are similar to those observed in earlier oxidation studies of smaller plates. Is also clear that some barbs do not fully discharge. This result agrees with the current density data.

Figures 4.31 and 4.32 are similar to Figures 4.29 and 4.30 but for current densities corresponding to $N_{EHD} = 2$. Figure 4.32, for the barbed plate, shows some overlapping zones of current from the barbs. Since field lines cannot cross, there must have been a shift in the discharge pattern over time, with some barbs discharging less and others more.

4.2.4 Current Distributions in the Wind Tunnel

Current density distribution at the ground plate of the wire-plate precipitator operating at $N_{EHD} = 1$ is shown in Figure 4.33. This plot shows only current densities measured on the center 30.5 cm by 30.5 cm section of the ground plate. Comparable data obtained in the barbed plate-to-plate precipitator at $N_{EHD} = 1$ are shown in Figure 4.34. Data measured at $N_{EHD} = 2$ are plotted in Figures 4.35 and 4.36 for the wire-plate and barbed plate-to-plate precipitators, respectively. Comparative statistics on the data are given in Table 4.4. Two data sets at each operating point are taken to ensure repeatability. The average of the two sets are reported in Figures 4.33 through 4.36 and Table 4.4. Splines are fitted through data grids in Figures 4.33 through 4.36 to increase

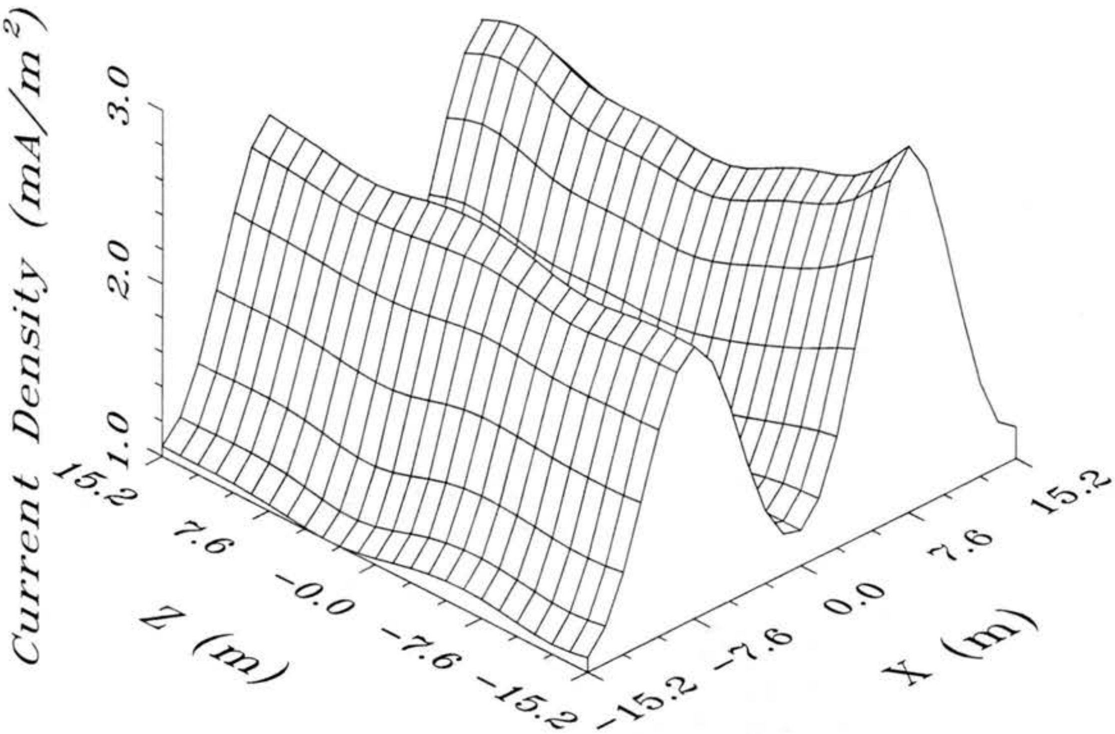

Figure 4.33. Ground plate current density distribution in the wire-plate precipitator at $N_{EHD} = 1$.

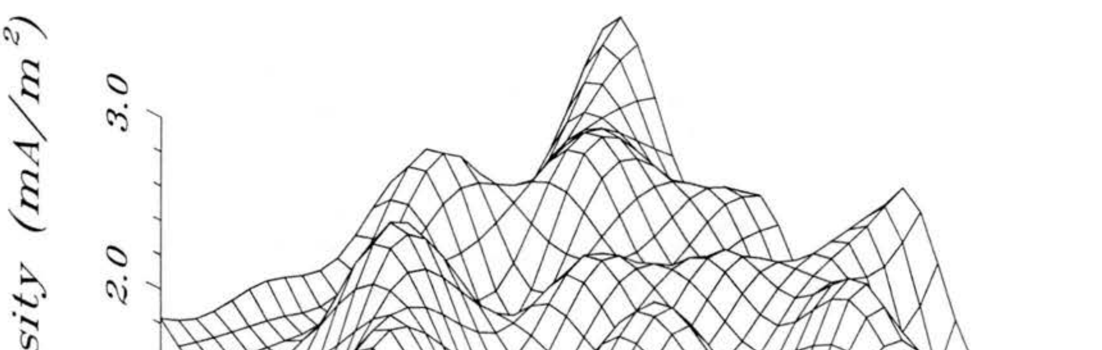

Figure 4.34. Ground plate current density distribution in barbed plate-to-late precipitator at $N_{EHD} = 1$.

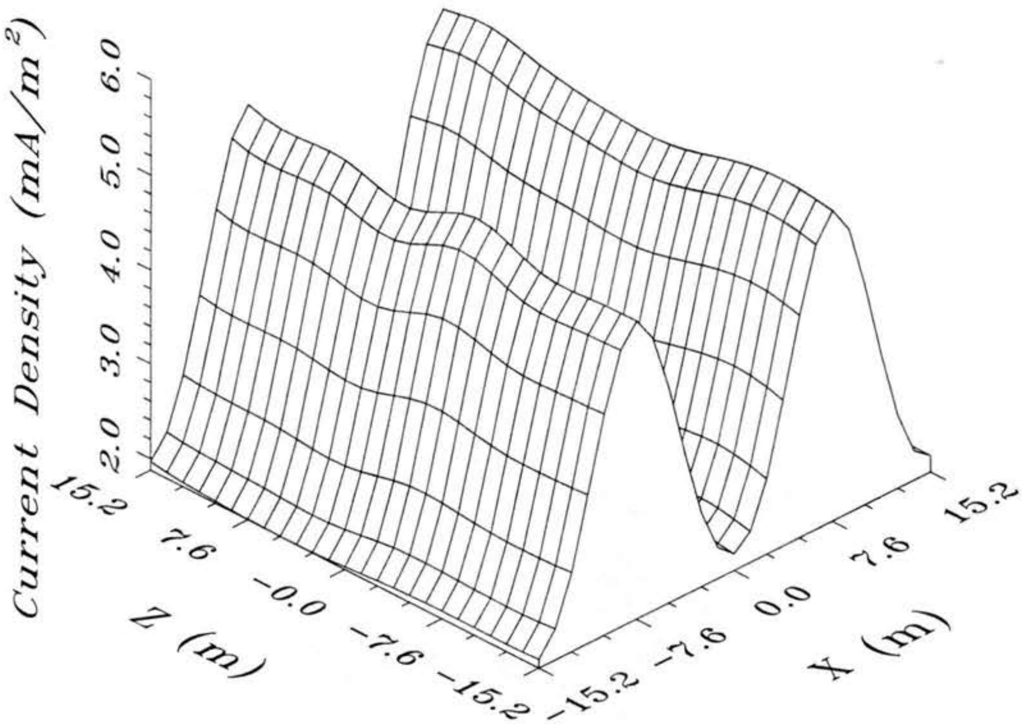

Figure 4.35. Ground plate current density distribution in the wire-plate precipitator at $N_{EHD} = 2$.

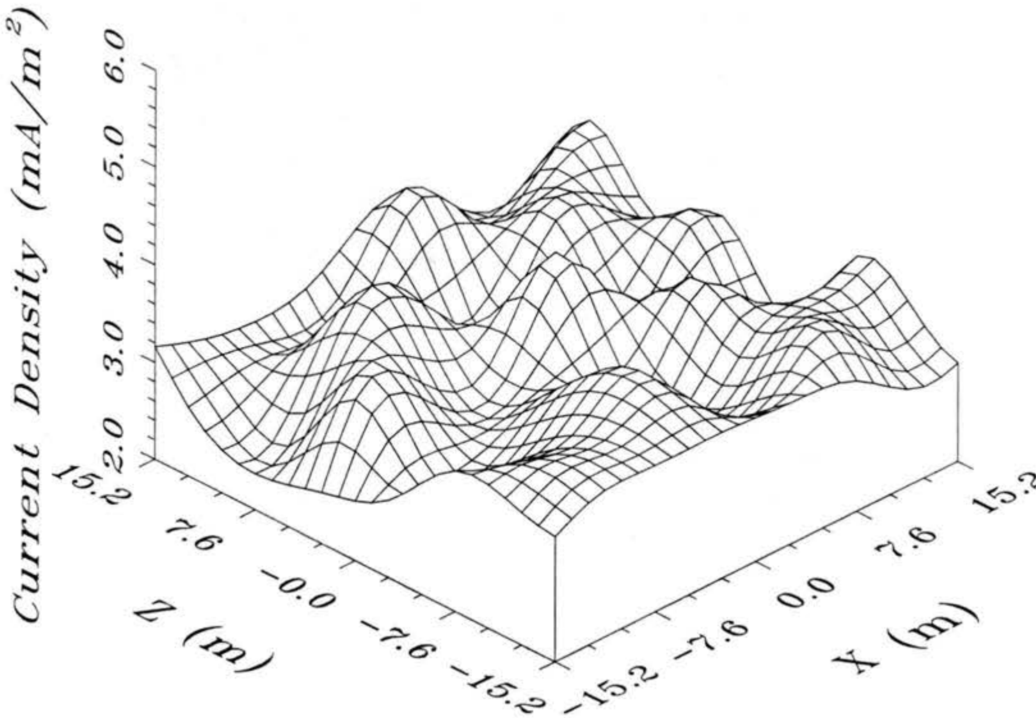

Figure 4.36. Ground plate current density distribution in the barbed plate-to-plate precipitator at $N_{EHD} = 2$.

Table 4.4. Current distributions obtained in the wind tunnel.

	$N_{EHD} = 1$ Barbed Plate	$N_{EHD} = 1$ Wires	$N_{EHD} = 2$ Barbed Plate	$N_{EHD} = 2$ Wires
Operating Parameters:				
Applied Voltage (kV)	56	34	68	40
Mean Electric Field (kV/cm)	4.1	4.5	5.0	5.2
Current Density Statistics (mA/m^2):				
Mean	1.8	1.8	3.2	3.5
rms	0.3	0.6	0.4	1.2
Min	1.1	1.4	2.5	2.6
Max	2.3	2.9	3.8	5.3
rms/mean*100 (%)	16	31	11	33
Percent of ground plate area with current density within given percent of mean:				
±10%	54	16	67	15
±20%	91	33	98	30
±30%	99	55	100	50
±40%	100	91	100	81
±50%	100	99	100	100

the line density and give a more realistic representation of the actual current density distribution. Because the ground plate segments are larger than the regions of zero current between wires, barbs, and corona tufts, measured current density never drops to zero.

At the lower current values where $N_{EHD} = 1$, mean current densities are equivalent in the two precipitators; however, rms current density in the wire-plate precipitator is 0.6 mA/m^2 as compared to 0.3 mA/m^2 in the barbed plate precipitator. At $N_{EHD} = 2$, mean current densities are once again similar in the two precipitators. The discrepancy in rms current density is greater than at the lower nominal current levels. In the wire-plate geometry, rms current density is 1.2 mA/m^2 as compared to 0.4 mA/m^2 in the barbed plate. Note that rms values in the barbed plate are relatively insensitive to operating voltage.

As observed in the smaller-scale data in Table 4.3, the barbed plate precipitator distributes current density near the mean current density to a larger portion of the ground plate than does the wire-plate precipitator. At $N_{EHD} = 1$, 99% of the ground plane receives current within ±30% of the mean, while only 55% of the ground plane in the wire-plate precipitator receives current within ±30% of the mean current density. As before, this difference is enhanced at higher voltages. At $N_{EHD} = 2$, 98% of the ground plane receives current within ±20% of the mean, while only 30% of the ground plane in the wire-plate precipitator receives current within ±20% of the mean.

4.2.5 Computed Estimates of Inter-Electrode Potential and Current Density

Presented in this section are plots of inter-electrode electric potential, electric field, and current density. The plots are computed by Linnebur (1993) using the method of characteristics with a finite element code to solve the governing electrodynamic equations at operating conditions identical to those used in the wind tunnel. Figure 4.37 is a surface plot of the inter-electrode current density in the wire-plate precipitator operating at $N_{EHD} = 1$. The plane plotted is normal to the wire, the wire being at X,Y coordinate 0,0. The ground plate is at Y = 7.62 cm (along the X axis) and the Z coordinate of the plot is current density in mA/m^2. The extra curve along the X axis of the plot is the measured current density distribution at the ground plate shown in Figures 4.23 and 4.24. The numerical solution matches the experimental data quite well at the ground plane and indicates that current density is highly variable in the inter-electrode space of the wire-plate precipitator. Figure 4.38 is a similar plot for the barbed plate electrode operating

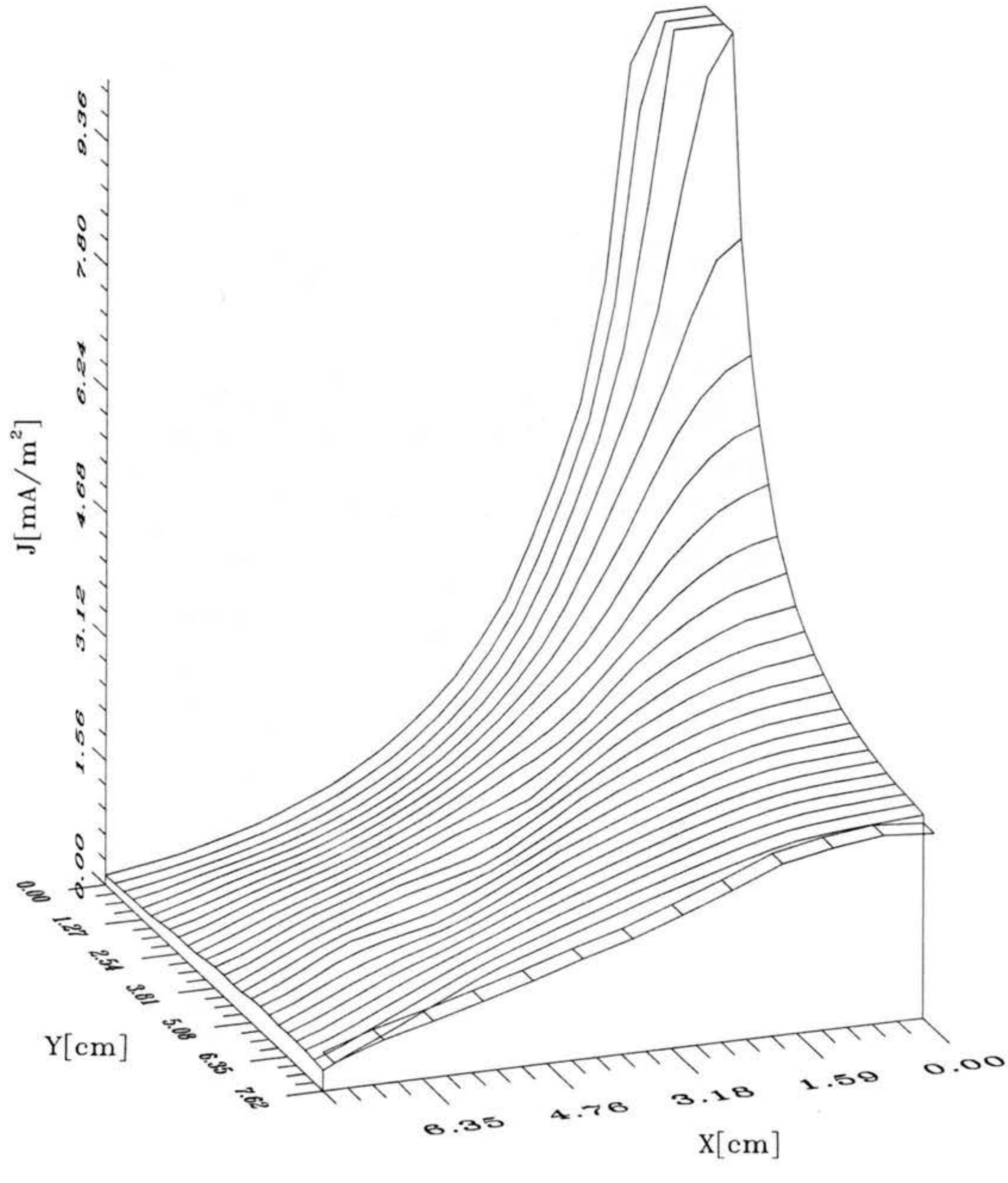

Figure 4.37. Calculated current density distribution across the inter-electrode space in the wire-plate configuration for N_{EHD} = 1. Peak current density at wire is 111 mA/m^2.

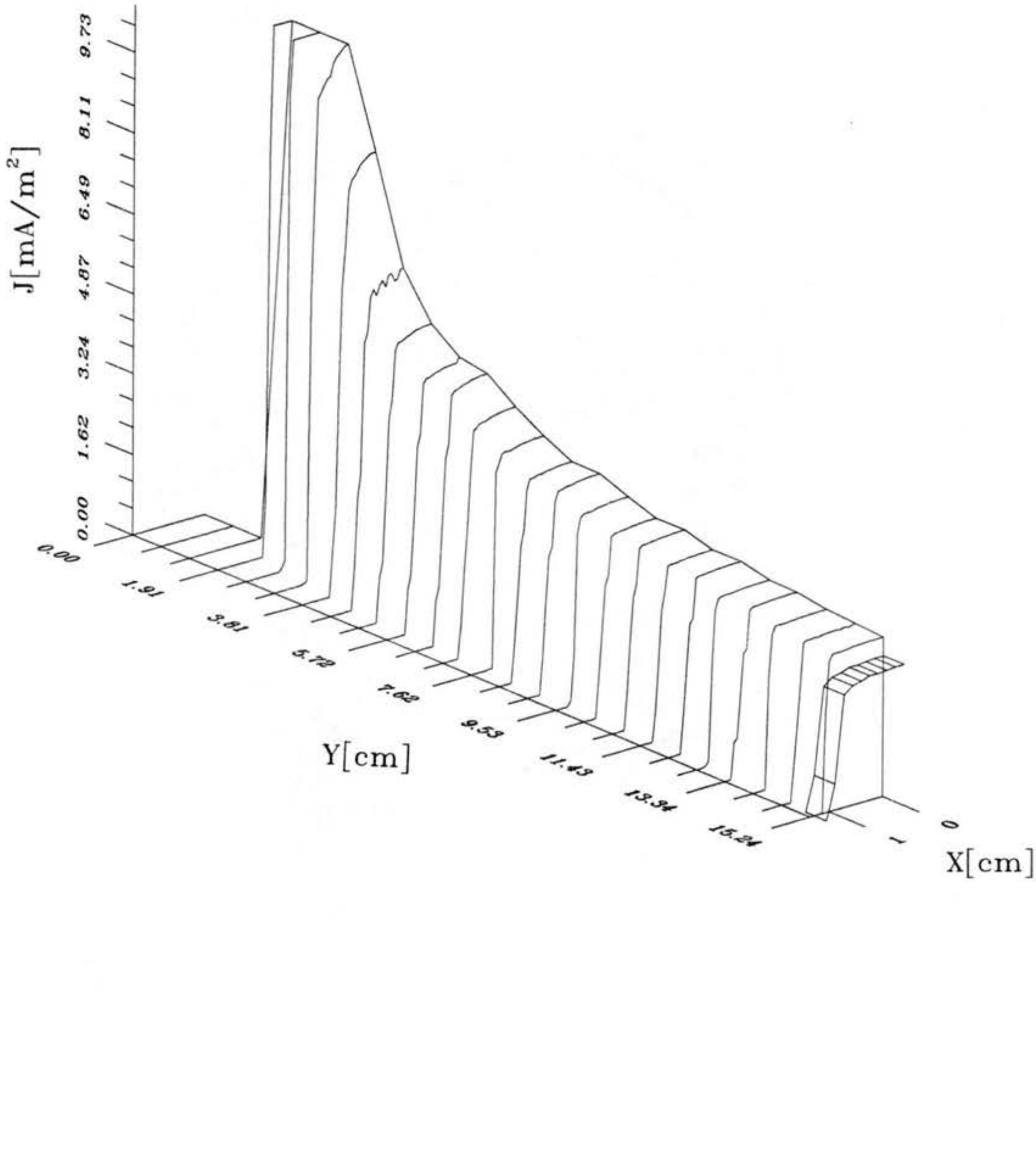

Figure 4.38. Calculated current density distribution across the inter-electrode space in the barbed plate configuration for $N_{EHD} = 1$. Peak current density at barb tip is 4,888 mA/m^2.

at $N_{EHD} = 1$. The plane plotted in this case is normal to the barbed plate and contains one barb at coordinate 0,0. These numerical data also indicate large spatial variations in current density. However, it is important in comparing these data to those plotted in Figure 4.37 to keep in mind that the scale of the barb-to-barb spacing is much smaller than that of the wire-to-wire spacing. As a result current density variations in the barbed plate precipitator are much smaller scale than are the variations in the wire-plate precipitator.

Figures 4.39 and 4.40 show electric field lines and lines of constant potential in the same planes of Figures 4.37 and 4.38. The barbed plate clearly behaves as intended in the sense that electric field lines are much more uniform over a larger portion of the inter-electrode space of the barbed plate precipitator than they are in the wire-plate precipitator. The barbed plate also produces a more uniform electric potential than do the wires, both in the streamwise (X) direction and in the transverse (Y) direction. This uniformity is an indication that the use of an "average" electric field in particle mobility calculations is acceptable in the barbed plate precipitator, except near the discharge points. It is clear that with the exception of the area immediately surrounding the barb or wire, electric field strength is greater nearest to the ground plate. This finding is in contrast to a Laplacian solution to the problems (in the absence of space change) in which the weakest electric field would be expected near the ground plate. Space change in the interelectrode space obviously has a profound effect on the electric field. Plots analogous to Figures 4.37 through 4.40 but for $N_{EHD} = 2$, look very similar to the plots shown here and are presented in Appendix B for completeness. The data presented in Section 4.2

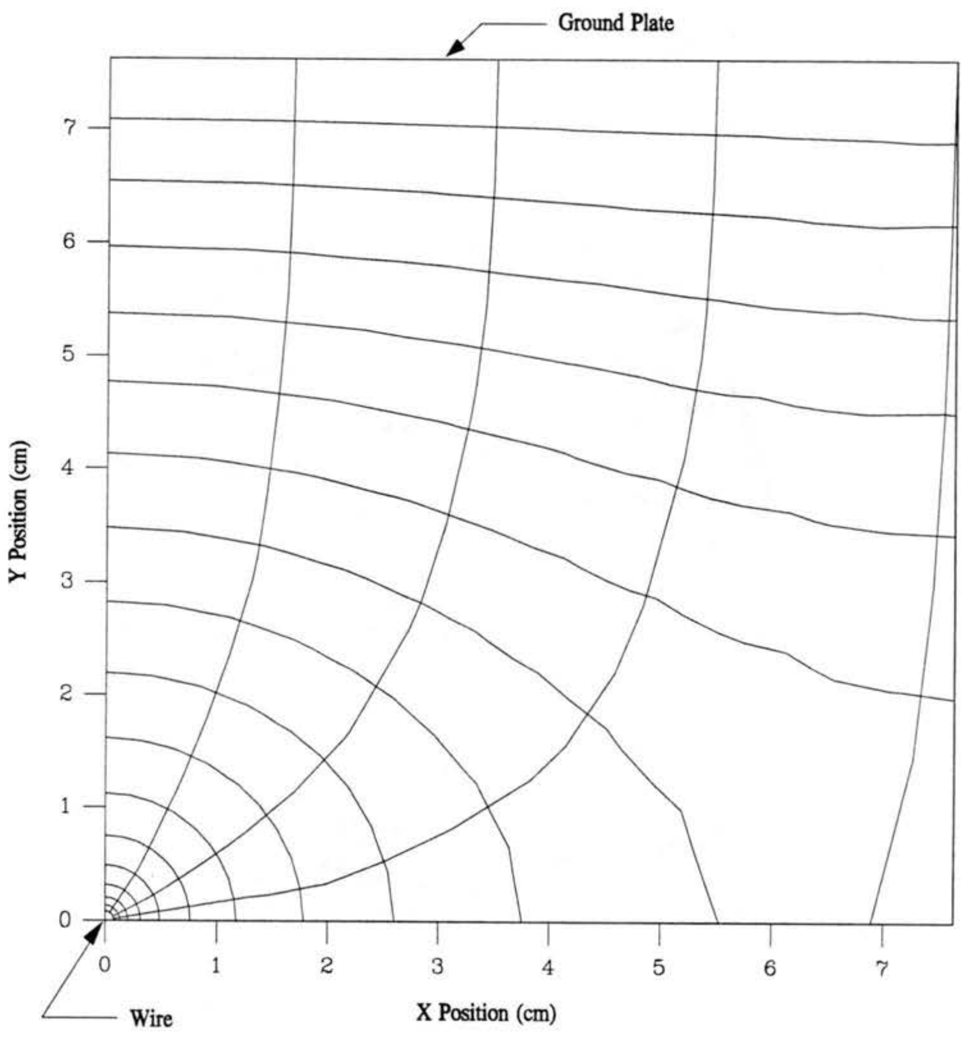

Figure 4.39. Calculated electric potential and field lines across the inter-electrode space in the wire-plate configuration for $N_{EHD} = 1$. Contour interval is 2 kV.

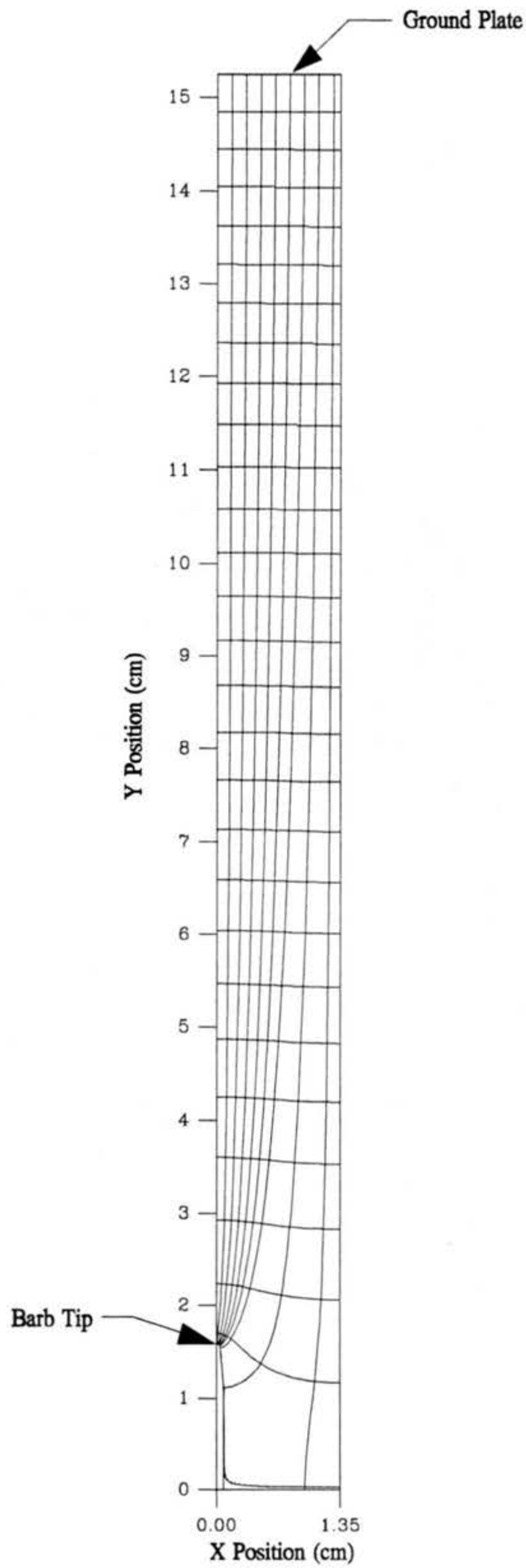

Figure 4.40. Calculated electric potential and field lines across the inter-electrode space in the barbed plate configuration for $N_{EHD} = 1$. Contour interval is 2 kV.

clearly show that the barbed plate geometry provides a more uniform current distribution than the wire-plate geometry.

4.3 Laser Light-Sheet Flow Visualization in the Wind Tunnel

The photographs presented here are obtained at a bulk streamwise velocities of 1.0 m/s and N_{EHD} = 1 unless otherwise noted. Pictures are more easily obtained at lower current densities and field strength because particles remain in the flow field for a longer period of time. The phenomena observed and discussed here appear similar at N_{EHD} = 1 and N_{EHD} = 2 when viewing the visualization in person. The plane illuminated by the laser light sheet in each photograph is the X-Y plane at or near Z = 0. The exposure time for each photograph is 1/60th or 1/125th of a second so that particle streaks are created to show motion.

Figure 4.41 is a photograph of flow in the barbed plate precipitator test section with the high voltage power turned off. The flow is moving from left to right and the illuminated streaklines are nearly parallel, indicating very low turbulence levels. The N_{EHD} = 0 condition for the wire-plate precipitator is very similar and not shown.

Figure 4.42 is a photograph of particle motion in the wire-plate precipitator operating at $N_{EHD} \approx 1$ and the view is from the top, upstream end of the test section. The flow is clearly much more turbulent than the no-power condition show in Figure 4.41. The black streak down the middle of the precipitator is the shadow created by wires to the right. The horseshoe-like shape around the second wire (from left) and lack of particles inside that area are an indication of high particle velocities due to the intense electric field near the wire. This is consistent with phenomena observed by other

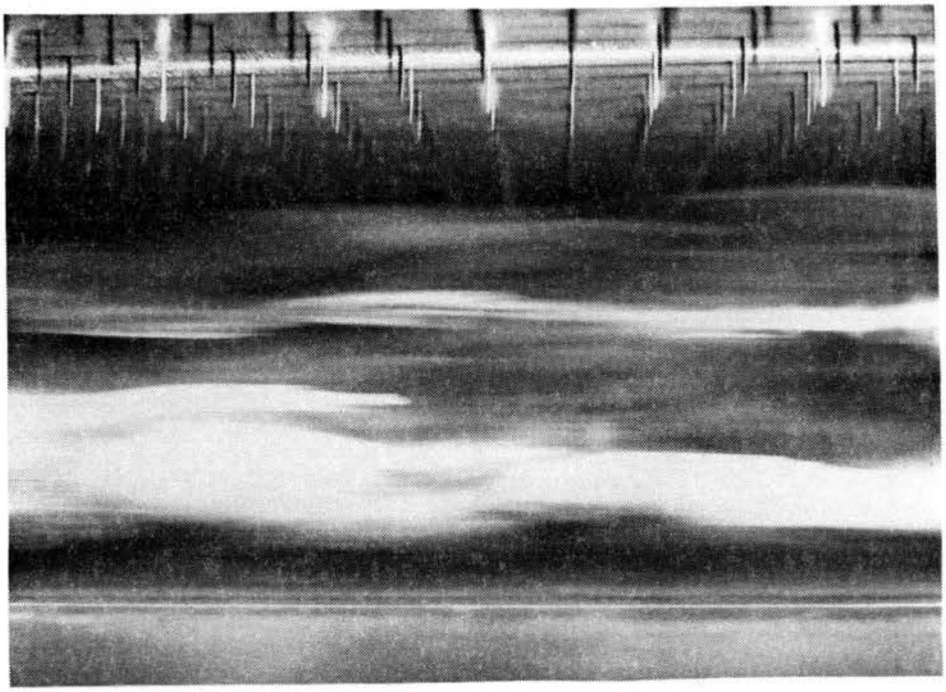

Figure 4.41. Laser light-sheet flow visualization of particle motion in the precipitator test section at $N_{EHD} = 0$.

Figure 4.42. Laser light-sheet flow visualization of particle motion in the wire-plate precipitator at $N_{EHD} \approx 1$.

researchers (Larsen and Christensen, 1986; Kallio and Stock, 1990; Davidson and McKinney, 1991). Some particles are forced around the region altogether, creating the horseshoe shape, much like the textbook potential flow problem of a source in a uniform flow. A pattern of motion toward the wall and then back toward the center of the channel is visible next to and downstream of the second wire.

Larger recirculating eddies are visible near the wall adjacent to the first wire and are accompanied by a region of accelerated streamwise flow surrounding the wire. Figure 4.43 is a close-up view of the region around the first wire. The recirculating eddies or "rolls" are consistent with the numerical and experimental results of Yamamoto (1981) and with laser Doppler data gathered in a barbed-wire precipitator by Larsen and Christensen (1986). The accelerated flow near the wire has been measured with laser Doppler anemometry by Leonard *et al.* (1983) and by Kalio and Stock (1992) and does not appear in helium-tracer measurements of Robinson (1975) or the LDA data of Masuda *et al.* (1979). This contradiction may be resolved by realizing that the data indicating an increased centerline velocity were made in single-wire precipitators or at the first wire of multiple-wire precipitators. It is apparent from this study that the interaction of the bulk flow and a single or leading wire creates the large scale rolls, not evident near interior wires. Thus it is important in obtaining measurements in a model precipitator, to consider only wires away from the upstream edge. Any measurements taken with a single wire, or near the leading wire will represent only edge effects.

Visualization of particle motion in the barbed plate precipitator operating at $N_{EHD} \approx 0.2$ is shown in Figure 4.44. The particle motion is clearly highly turbulent thoughout the precipitator. The central and end sections contain turbulence of a much smaller scale

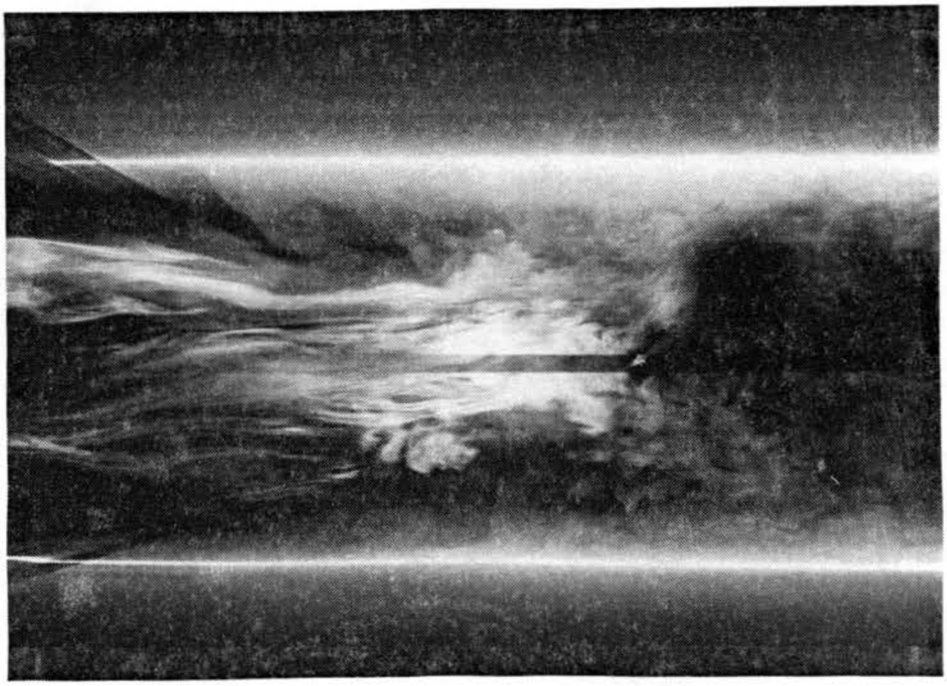

Figure 4.43. Laser light-sheet flow visualization particle motion in entrance of wire-plate precipitator at $N_{EHD} \approx 1$.

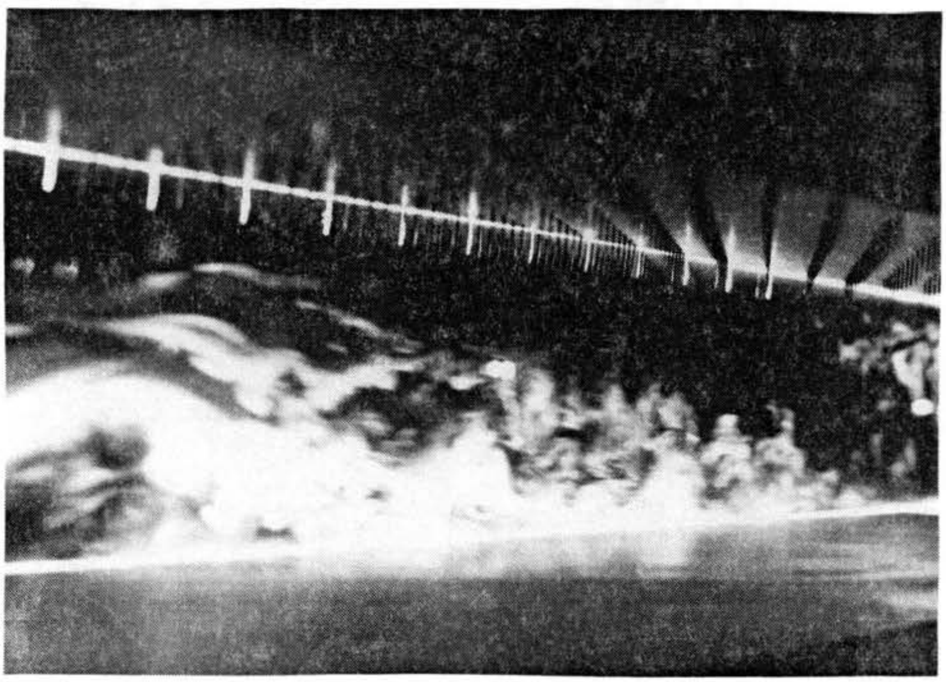

Figure 4.44. Laser light-sheet flow visualization of particle motion in the barbed plate precipitator at $N_{EHD} = 0.2$.

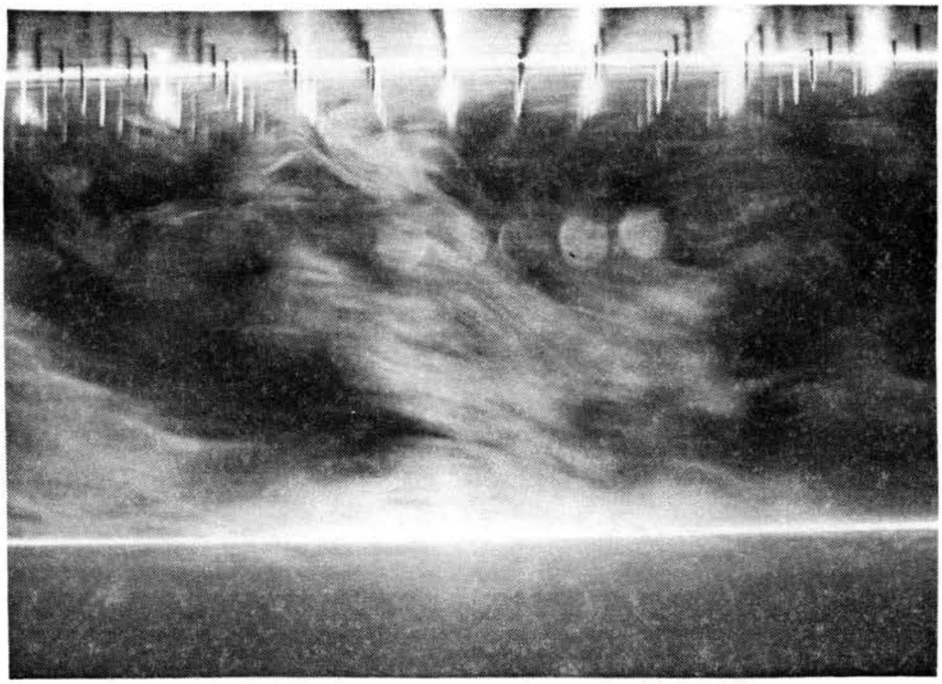

Figure 4.45. Laser light-sheet flow visualization particle motion in center of barbed plate precipitator at $N_{EHD} = 1$.

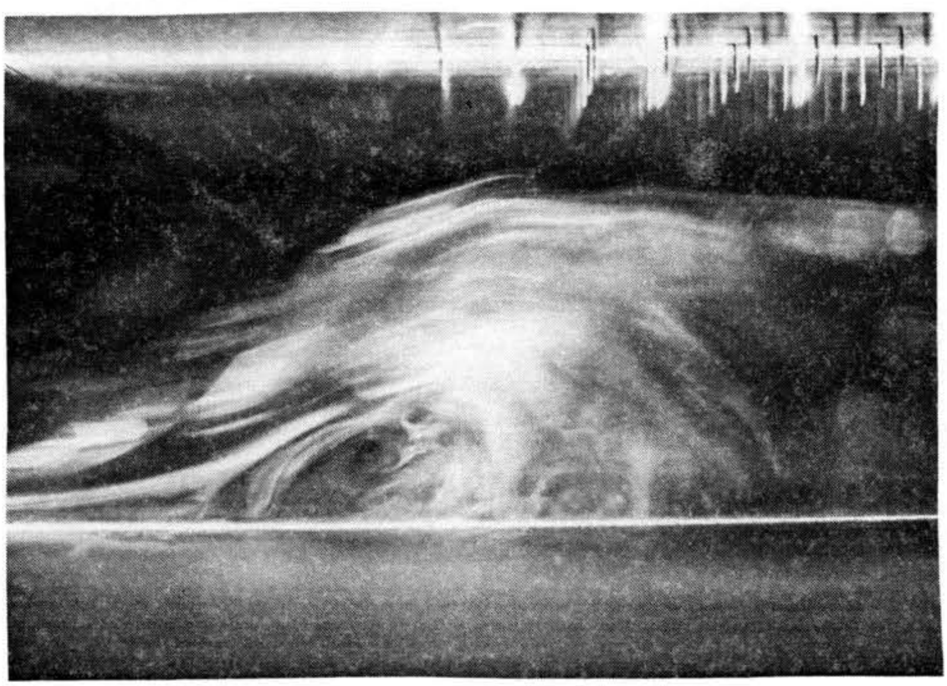

Figure 4.46. Laser light-sheet flow visualization particle motion in entrance of barbed plate precipitator at $N_{EHD} = 1$.

than does the entrance section. Figure 4.45 shows particle motion (at $N_{EHD} \approx 1$) in the central section of the precipitator. Particle motion away from barbs tips due to the electric wind and/or increased space charge and electric field in the vicinity of the barb tips is seen near the barbs just to the left of the center of the photograph. The entire region is highly turbulent. Figure 4.46 shows the particle motion at the entrance of the precipitator where a strong roll is present, similar to the two rolls observed in the wire-plate geometry. Once again measurements should be taken far from the leading edge of the plate.

4.4 Particle Velocities in the Electrostatic Precipitator

4.4.1 Particle Charge and Mobility

Prior to making any LDA measurements, the particle charging time and mobility are estimated using the methods presented in Chapter 3. Table 4.5 presents the results of these calculations for a 0.7 μm alumina particle under each of the precipitator operating conditions. The distance along the precipitator required for charging is estimated by assuming the particles are convected downstream at the 1.0 m/s bulk flow rate. It is clear that particles are charged to saturation well before the central section of the precipitator model. It takes as much as 4.8 cm before particles are charged to saturation in the barbed-plate precipitator at $N_{EHD} = 1$ and as little as 3.5 cm in the same precipitator at $N_{EHD} = 2$. Since no LDA measurements are made within 15 cm of the entrance to the precipitator it is safe to assume that all particles are fully charged in the measurement region (-15.24 cm to +15.24 cm about the precipitator center). Table 4.5 also indicates

Table 4.5. Particle charge and drift velocity in laboratory precipitators.

	$N_{EHD} = 1$		$N_{EHD} = 2$	
	Wires	Plate	Wires	Plate
Electrode Spacing (cm)	7.62	13.65	7.62	13.65
Voltage (kV)	34	56	40	68
Avg. Electric Field (kV/cm)	4.46	4.10	5.25	4.98
Current Density (mA/m²)	1.6	1.6	3.2	3.2
Saturation Charge (C)	5.67e-17	5.21e-17	6.66e-17	6.33e-17
Time to Sat. Charge (s)	0.057	0.048	0.039	0.035
Dist. to Sat. at 1.0 m/s (cm)	5.7	4.8	3.9	3.5
β_p at Sat. Chg. (m²/V s)	6.11e-07	5.61e-07	7.18e-07	6.81e-07
w_e at Sat. Chg. (m/s)	0.27	0.23	0.38	0.34
% of Sat. Chg. after 15.24 cm	111	114	113	114
% of Sat. Chg. after 45.72 cm	119	122	118	120

that diffusion charging contributes little to the total particle charge once saturation charge is reached. For example, particles in the barbed plate precipitator only reach 120% of the accepted saturation charge before exiting the measurement region. Charge values may exceed 100% because saturation charge is defined only as the maximum amount of charge that field charging may apply to a particle.

Calculated particle mobilities for a fully charged particle are 6.1×10^{-7} m^2/V-s for the wire-plate geometry at $N_{EHD} = 1$ and 5.6×10^{-7} m^2/V-s for the corresponding barbed plate geometry. The difference occurs because the average electric field is slightly higher in the wire-plate geometry than it is in the barbed plate geometry and therefore more charge can be placed on the particle through field charging. The higher average mobility, combined with the higher average electric field strength, produces a larger expected average transverse drift velocity in the wire-plate precipitator than in the barbed plate precipitator.

4.4.2 Mean and RMS Particle Motion Stability

In order to obtain an estimate of the required sample time to measure an accurate mean and rms particle velocity with the precipitator operating, particle velocities are sampled using the LDA for time spans up to 18 minutes at a sample rate of 200 Hz. Figures 4.47 and 4.48 are streamwise mean and rms velocity measurements showing 2.6 second segment averages and the cumulative average over time for the barbed plate precipitator at $N_{EHD} = 1$. Although the variation in the rms over the span is fairly steady, the mean value ranges from 0.65 m/s to 1.05 m/s and takes almost 5 minutes to make that shift. It is clear that particle motion in the operating precipitator is not a steady process. Changes in particle velocity are most likely the result of barbs becoming dirty and ceasing to discharge while other barbs are able to discharge with more current, thereby changing the current distribution and particle velocity patterns. The streamwise rms velocity and both the transverse mean and rms velocities, shown in Figures 4.49 and 4.50, are relatively stable. A sampling period of 92 seconds proved to be sufficient for all conditions except for the case shown in Figure 4.47, which is the worst case condition.

4.4.3 Particle Mean and RMS Velocities

Figures 4.51 through 4.56 are particle velocity maps in the X-Y plane of each precipitator geometry for $N_{EHD} = 0$, 1, and 2. Table 4.6 is a compilation of time series statistics on the velocity data. Because the electrode spacing in the barbed plate geometry is double that of the wire-plate geometry, it is necessary to gather data further from the entrance of the precipitator in the barbed plate geometry in order to avoid the effects of the entrance roll observed in the flow visualization. In the wire plate geometry, data is gathered near the second wire in the precipitator (at $X = -7.6$ cm , $Y = 0$ cm). In the

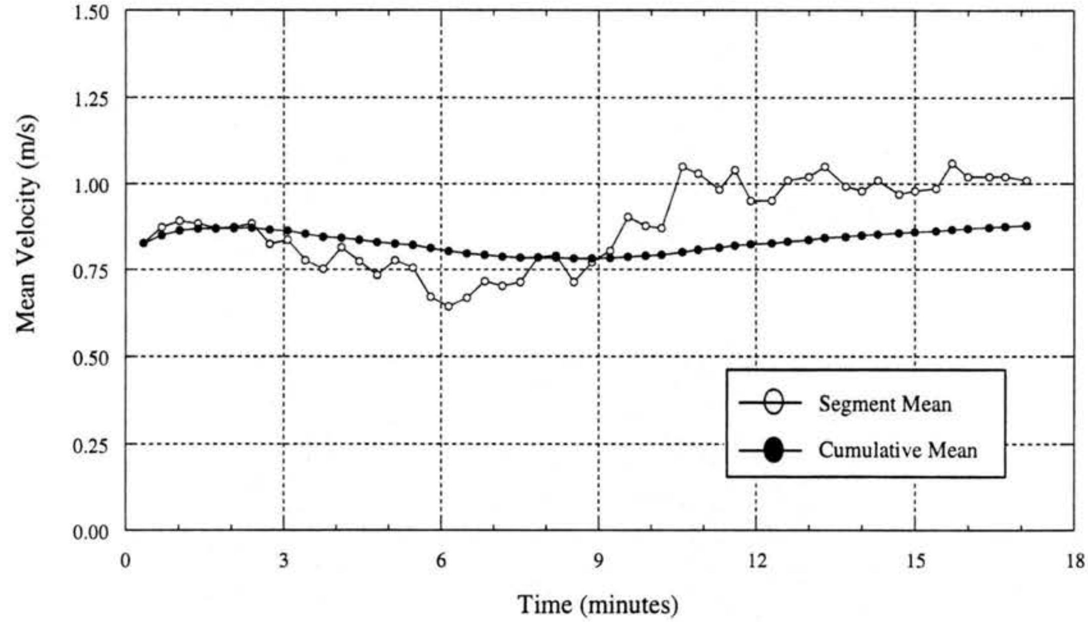

Figure 4.47. Streamwise particle mean velocity history.

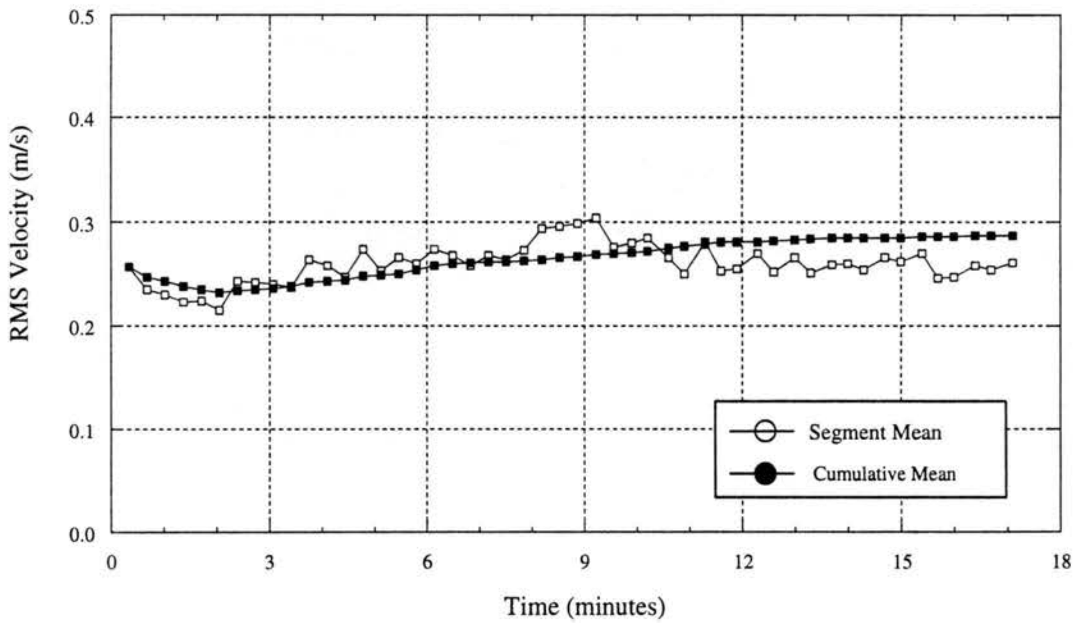

Figure 4.48. Streamwise particle RMS velocity history.

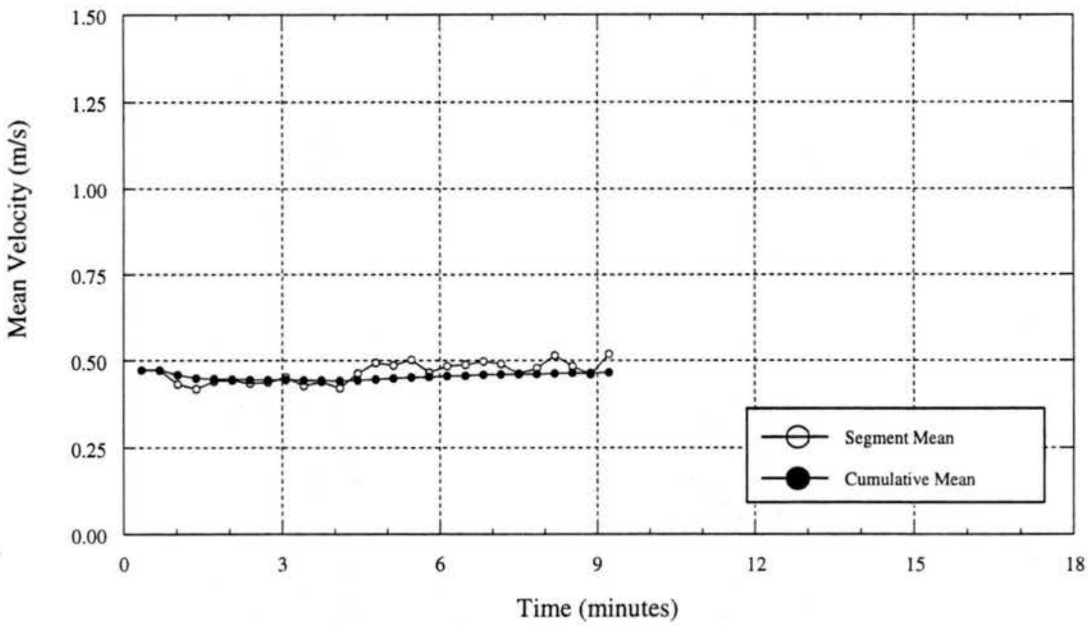

Figure 4.49. Transverse particle mean velocity history.

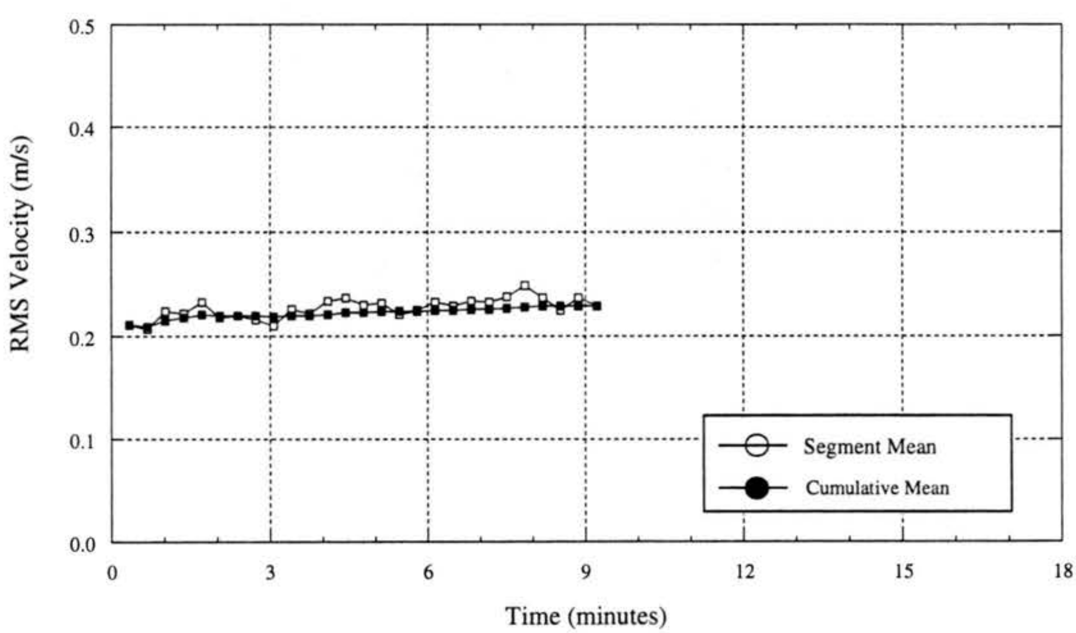

Figure 4.50. Transverse particle RMS velocity history.

barbed plate geometry, data is gathered near the column of barbs at X = 8.5 cm , Y = 7.6 cm. To make the two data sets easier to compare, the data are presented in this section with a shifted coordinate system, placing the wire and column of barbs mentioned above at a position X = 0. Additional data are taken at other locations in the wind tunnel, but not presented here in order to avoid improper weighting of the averages presented in Table 4.6. Appendix C contains tables listing all the data and Appendix D includes plots of the same data in the global coordinate system. All velocity values reported here are taken from the tables in Appendix D.

The arrows in Figures 4.51 through 4.56 are the vector sums of the streamwise (U) and transverse (V) particle velocities measured with the LDA. The length of the arrow is proportional to mean particle velocity and the arrow direction indicates the direction of the mean particle velocity. The circles at the arrow tails are the vector sum of the u_{rms} and v_{rms} velocities. The radius of each circle is scaled the same as the arrow lengths. A length of 2 cm in the plot coordinates represents a velocity of 1 m/s. In the barbed plate plots, the solid barbs are barbs in the same plane as the measurement points and the dashed barbs are in planes 13.5 mm above and below the measuring plane.

Figures 4.51 and 4.52 contain the particle velocity data in the absence of a corona discharge for the wire-plate and barbed plate geometries, respectively. As expected for a nominal flow of 1.0 m/s, particle velocities in the midsection of the channel are oriented in the streamwise direction at ≈ 1.0 m/s. Particles near the ground plate are slowed by the boundary layer. The rms velocities are so low (averaging ≈ 0.02 m/s yielding a turbulence intensity of 2%) that the circles cannot be seen on the plots. Figures 4.53 and 4.54 are plots of particle velocity data for $N_{EHD} = 1$. In the wire-plate geometry, shown

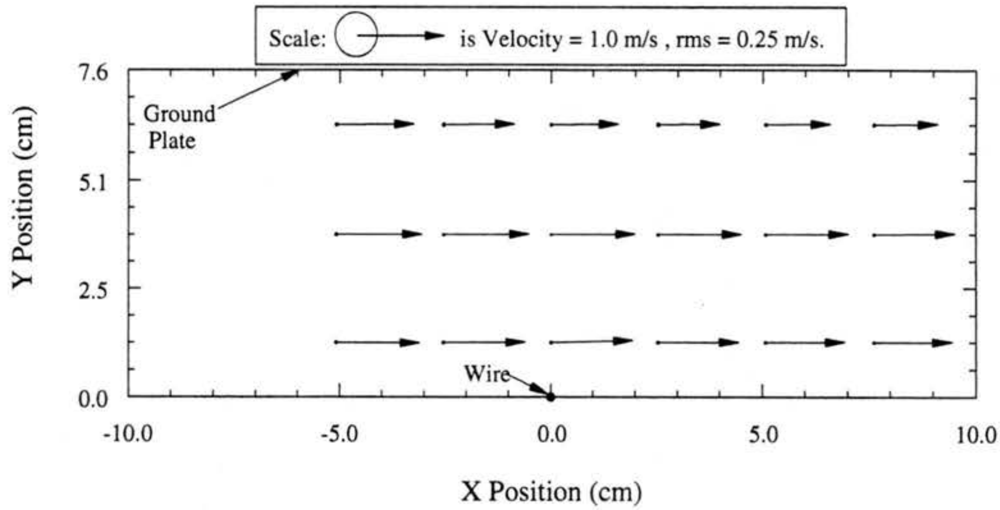

Figure 4.51. Particle velocity and RMS magnitude map for the wire-plate precipitator at $N_{EHD} = 0$.

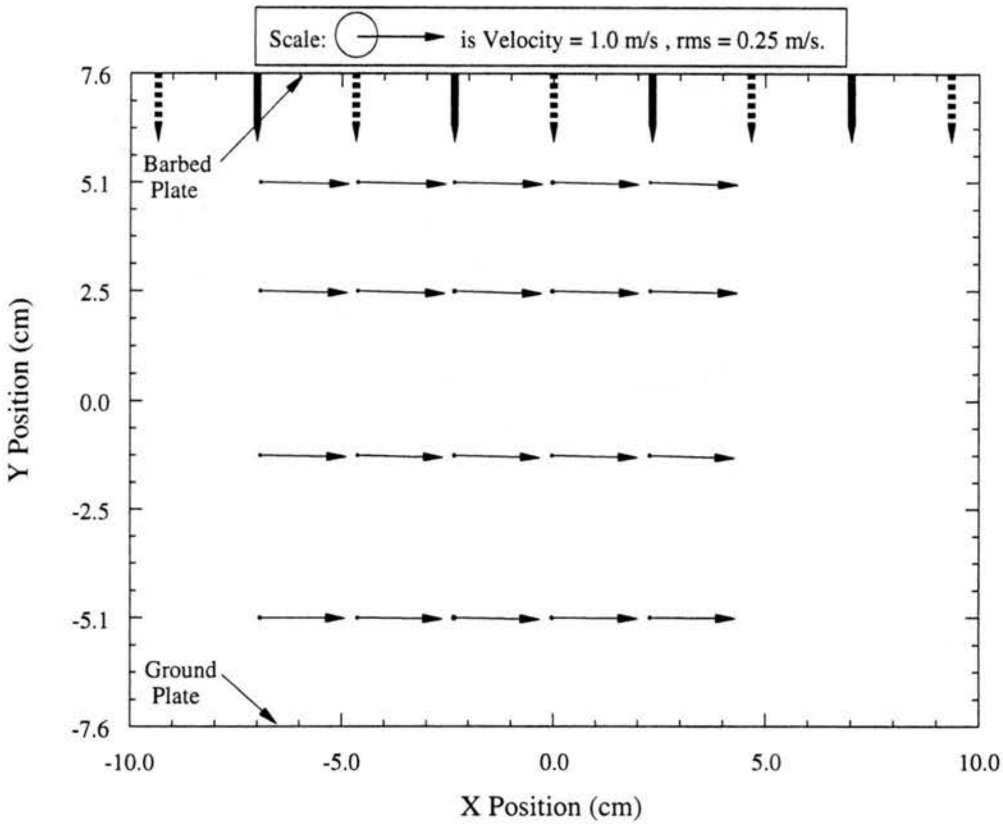

Figure 4.52. Particle velocity and RMS magnitude map for the barbed plate precipitator at $N_{EHD} = 0$.

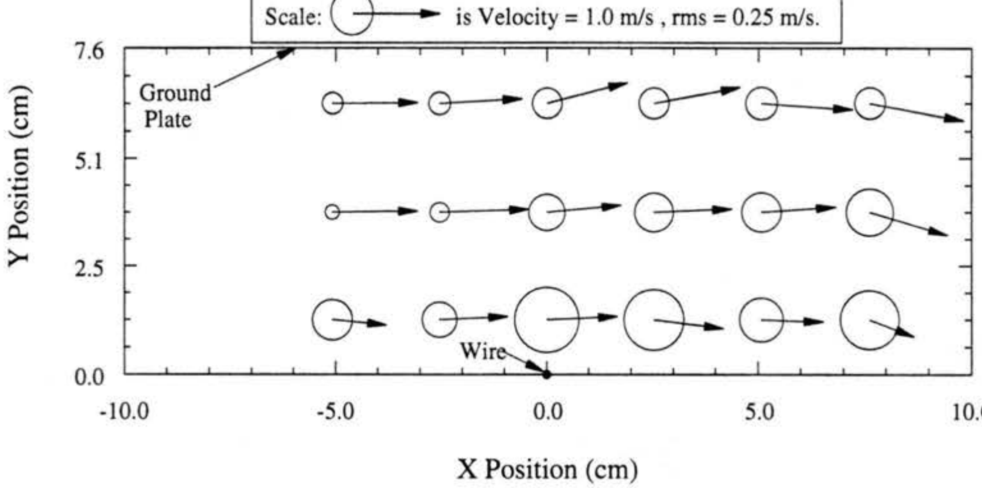

Figure 4.53. Particle velocity and RMS magnitude map for the wire-plate precipitator at $N_{EHD} = 1$.

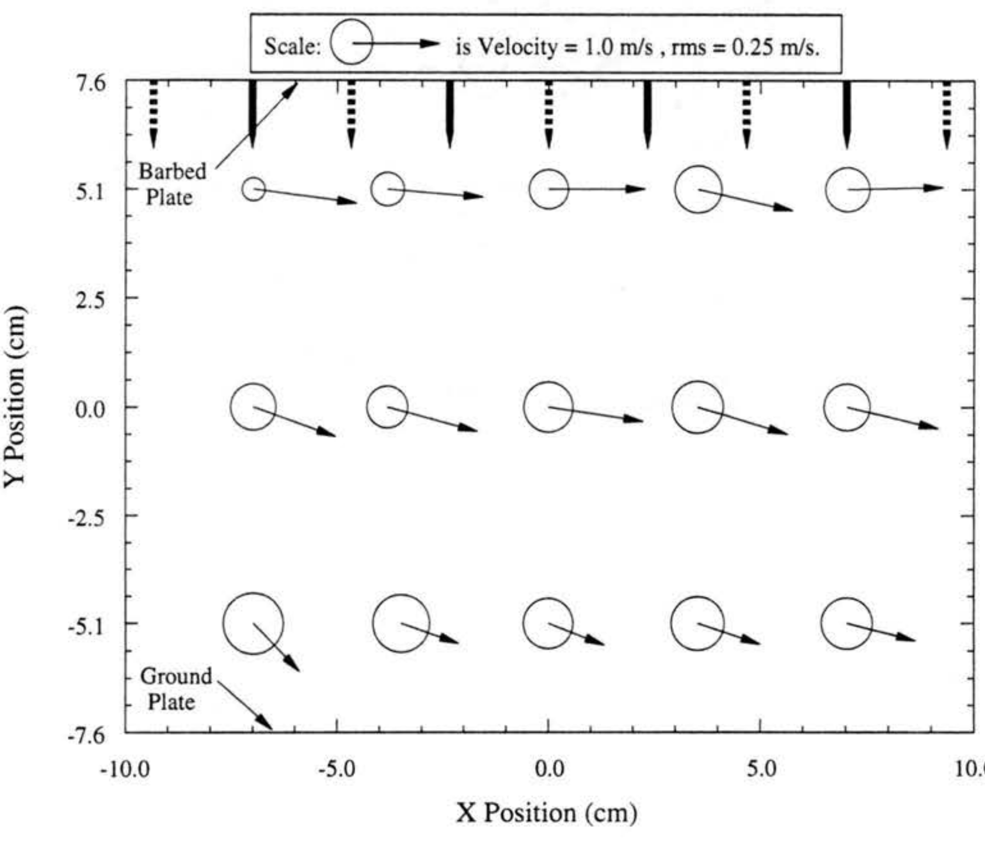

Figure 4.54. Particle velocity and RMS magnitude map for the barbed plate precipitator at $N_{EHD} = 1$.

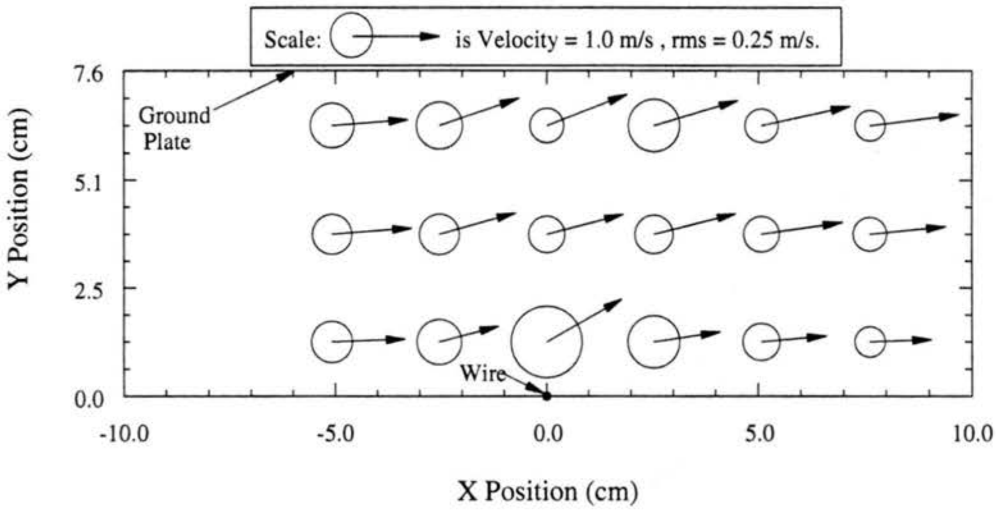

Figure 4.55. Particle velocity and RMS magnitude map for the wire-plate precipitator at $N_{EHD} = 2$.

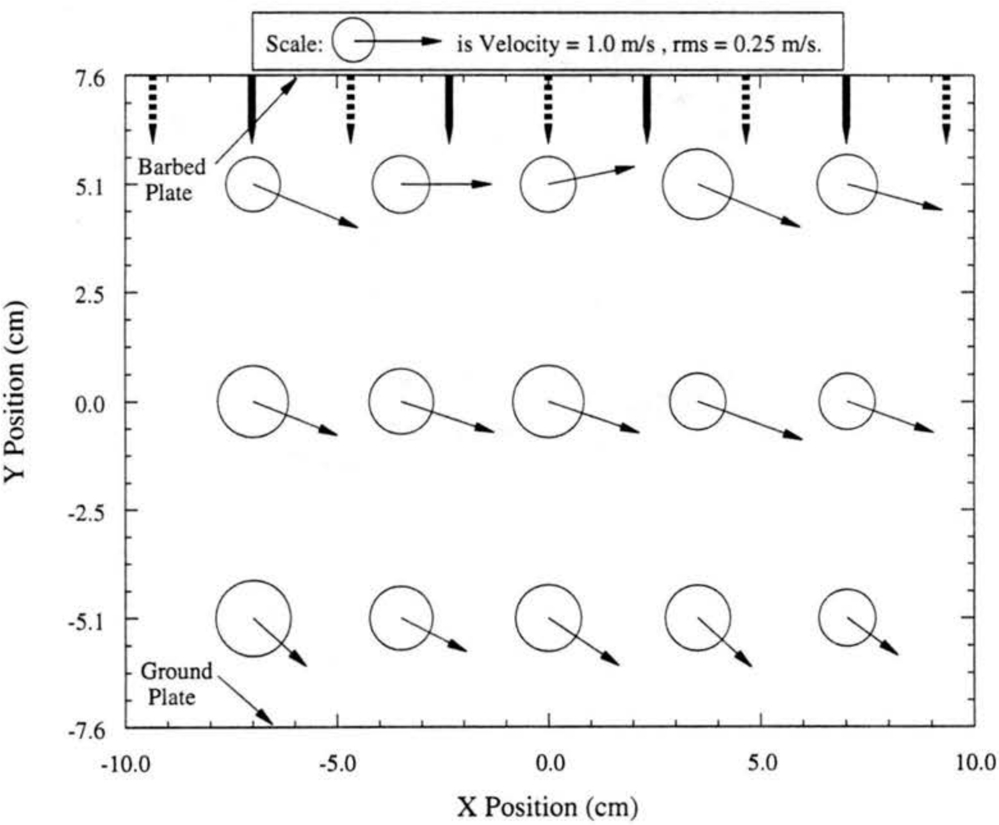

Figure 4.56. Particle velocity and RMS magnitude map for the barbed plate precipitator at $N_{EHD} = 2$.

Table 4.6. Streamwise and transverse particle velocity statistics.

		$N_{EHD} = 0$		$N_{EHD} = 1$		$N_{EHD} = 2$	
		Wires	Barbed Plate	Wires	Barbed Plate	Wires	Barbed Plate
Streamwise (U)	Mean Velocity (m/s)	0.91	1.02	0.90	0.96	0.90	0.97
	rms Velocity (m/s)	0.016	0.019	0.15	0.19	0.16	0.26
	Integral Length Scale (m)	0.26	0.23	0.016	0.018	0.017	0.020
	Diffusivity (m^2/s)	0.0042	.0044	.0024	.0034	.0027	.0052
Transverse (V)	Mean Velocity (m/s)	0.0084	0.022	-0.0085	0.22	0.19	0.37
	rms Velocity (m/s)	0.0050	0.0043	0.15	0.19	0.18	0.26
	Integral Length Scale (m)	2.3×10^{-5}	5.9×10^{-5}	1.4×10^{-3}	2.8×10^{-3}	4.7×10^{-3}	5.8×10^{-3}
	Diffusivity (m^2/s)	1.2×10^{-7}	2.5×10^{-7}	2.1×10^{-4}	5.3×10^{-4}	8.5×10^{-4}	1.5×10^{-3}
Turbulence Intensity (%)		1.84	1.91	23.57	27.28	26.18	35.42
Average Calculated Drift Velocity (m/s)		0.0	0.0	0.27	0.23	0.38	0.34

in Figure 4.53, both a drift toward the ground plate at the plane of the wire and a return flow between the pictured wire and the next wire are clearly visible. The largest drift (transverse) velocity occurs near the ground plate in the plane of the wire and is 0.24 m/s. The barbed plate data show a particle drift toward the ground plate in almost all locations, with higher velocities occurring near the ground plate. Turbulence intensities are greatly enhanced over the no-power condition in both geometries and are on average greater for the barbed plate (27.3% versus 23.6% in the wire-plate).

Figures 4.55 and 4.56 are analogous to Figures 4.53 and 4.54, but for $N_{EHD} = 2$. The accelerated drift velocity near the wire is very clear in this case and both geometries exhibit higher drift velocities near the ground plane. The average particle drift velocity measured in the barbed plate precipitator is 0.37 m/s, while it is 0.19 m/s in the wire-plate precipitator. These values differ from the estimated values of 0.34 and 0.38 reported in Table 4.6. The reason becomes clear when the electric potential distributions plotted in Figures 3.39, 3.40, B.3, and B.4 are considered carefully. The electric potential drops very quickly at the wire but not quite so much near the barb. The result is that the electric field throughout most of the inter-electrode space in the wire-plate geometry is weaker than the traditionally calculated average based on electrode spacing and wire voltage (as was calculated for Tables 4.5 and 4.6). The presence of the plate behind the barb tips in the barbed plate geometry prevents a sharp drop in the electric field just outside the corona region at the barb tips. Therefore, the barbed plate produces a high electric field strength over more of the inter-electrode space for a given electrode potential than the wire-plate geometry does. There is further discussion on this topic in Section 4.4.5.

Examination of the rms velocity values also reveals that turbulence levels vary spatially in the wire-plate precipitator more than they do in the barbed plate precipitator. Among the largest rms velocity values measured in either precipitator occur near the wire of the wire-plate precipitator, where rms velocity is 0.77 m/s at $N_{EHD} = 1$ and 0.85 m/s at $N_{EHD} = 1$. This indicates that the strong electric body force in the vicinity of the wires is the major producer of turbulence in that geometry. In the barbed plate geometry, on the other hand, the electric body force appears to generate equal turbulence throughout the entire interelectrode space.

4.4.4 Velocity Profiles

Horizontal velocity profiles extracted from the data shown in Figures 4.51 through 4.57 are plotted here so that streamwise and turbulent velocities from the different precipitator geometries may be compared more easily. Additionally, a vertical profile is plotted for the wire-plate geometry.

Figure 4.57 is a vertical profile of the transverse particle velocities at X = 0, Y = 3.8 (next to the second wire) in the wire plate geometry operating at $N_{EHD} = 1$. The variation in transverse velocity generated by the corona tufts along the wire is clear, with velocities ranging from -0.1 m/s to 0.6 m/s. This return flow, along with the return flow in the horizontal plane illustrated in Figure 4.53 make it clear that return flows or "rolls" exist in both the horizontal and vertical planes, corroborating work by previous researchers (Yamamoto and Velkoff, 1981; Larsen and Christensen, 1986). Note that the X-Y plane for all other velocity measurements in the wire-plate geometry is at Z = 6.35 cm, where the transverse velocity is near an average value of 0.2 m/s.

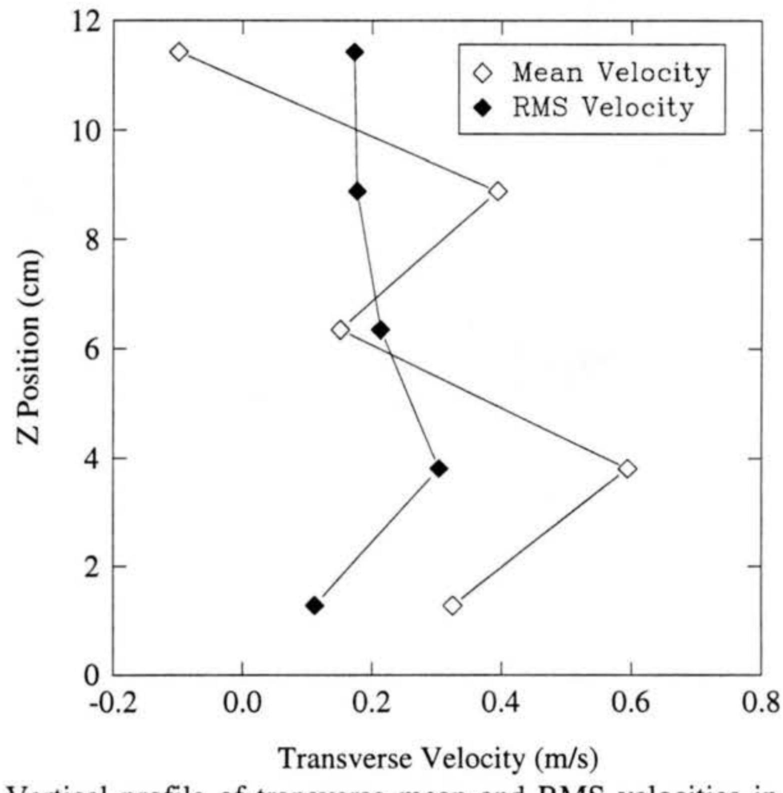

Figure 4.57. Vertical profile of transverse mean and RMS velocities in the wire-plate precipitator at $N_{EHD} = 1$.

Figure 4.58 is a horizontal profile in the X-direction of the streamwise velocities adjacent to a wire or barb (depending upon the electrode geometry). The wire is at position $Y = 0$ cm with ground plates at -7.62 cm and +7.62 cm and the barbed plate is at position $Y = 7.62$ cm with a ground plate at -7.62 cm. The data points plotted for the wires at negative Y positions are simply reflections of the actual data (at positive Y positions) and are denoted by a dashed connecting line. These data show the when the wire-plate precipitator operates at $N_{EHD} = 1$, the streamwise velocity near the wire is reduced by ≈15% from value at the $N_{EHD} = 0$ (1.0 m/s). This is partly due to the increased turbulence in the operating precipitator, enabling higher velocity flows to occur near the walls. The barbed plate profiles show a velocity deficit (≈40%) near the ground plate and a slight increase (≈10%) near the barbs.

The trends observed in profiles at the wire or barb also appear in averaged profiles, in which all data for a given Y position and operating condition are averaged into a single velocity value for that location. Figure 4.59 shows the average streamwise velocity as a function of Y position for both precipitators operating under each tested condition. Velocities are ≈20% lower near the core of the operating wire-plate precipitator than they are for $N_{EHD} = 0$. The reverse is true for the barbed plate electrode. Velocities are increased by ≈10% near the barbed plate when the power is on.

Figures 4.60 and 4.61 are transverse velocity profiles corresponding to the streamwise velocity plots of Figures 4.58 and 4.59. Transverse particle motion in both precipitators is highest near the ground plate with the exception of particles very near the wire at $N_{EHD} = 2$. This is consistent with observations made earlier and is expected because of the high electric field in the region near the wire. Figure 4.61 shows that for

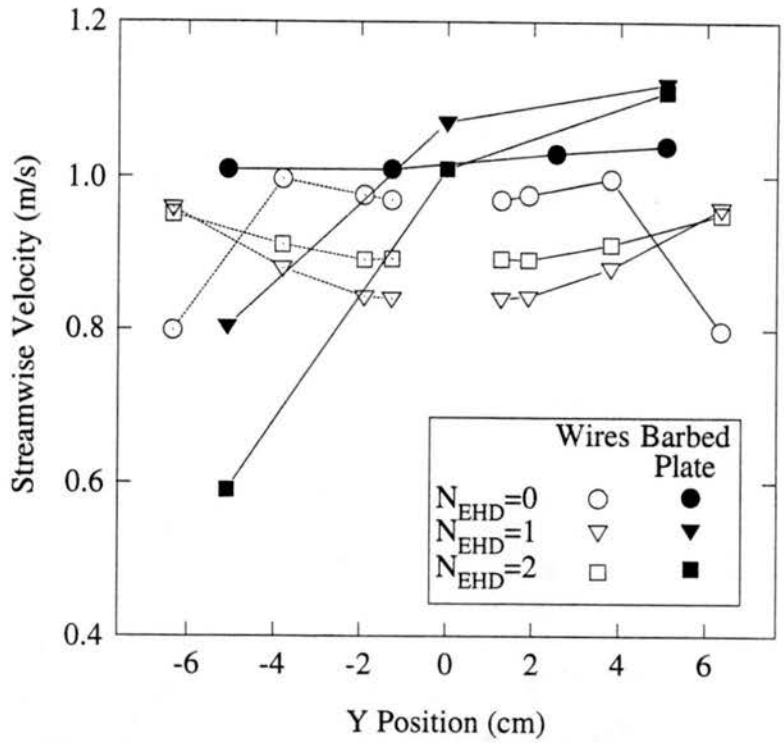

Figure 4.58. Horizontal profiles of streamwise particle velocities in the wire-plate and barbed plate precipitators. Profiles are in plane of wire or barb.

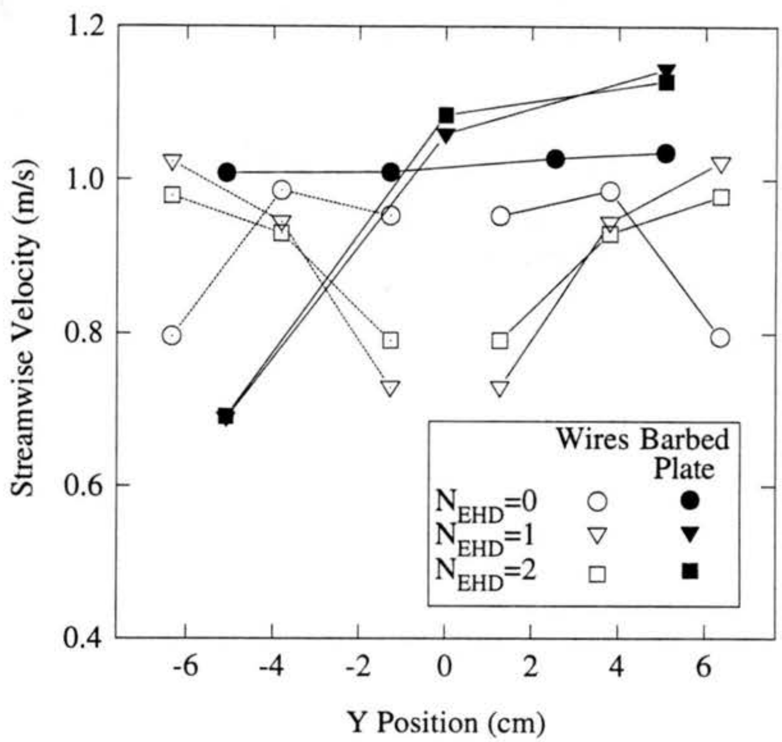

Figure 4.59. Averaged horizontal profiles of streamwise particle velocities in the wire-plate and barbed plate precipitators.

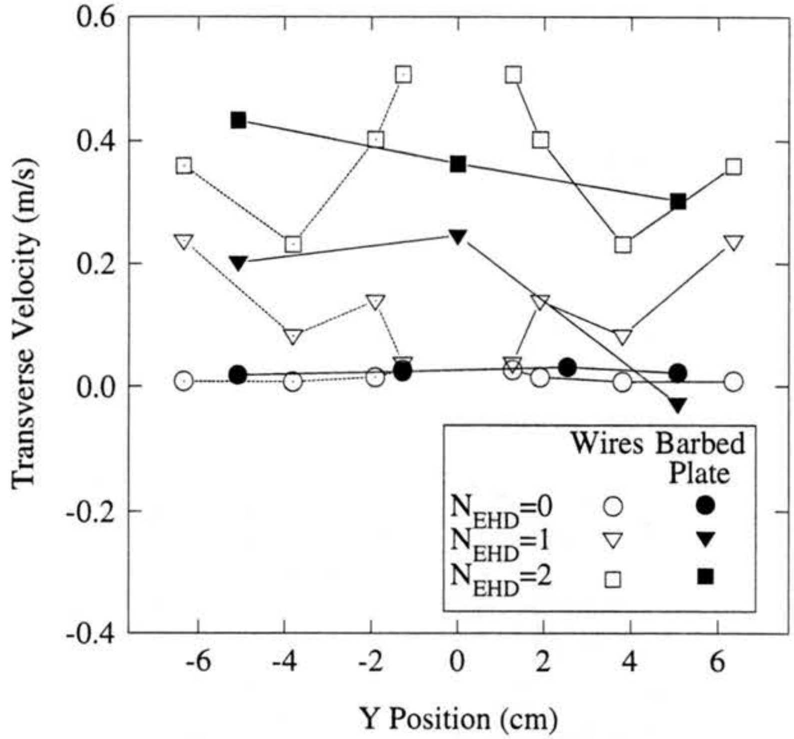

Figure 4.60. Horizontal profiles of transverse particle velocities in the wire-plate and barbed plate precipitators. Profiles are in plane of wire or barb.

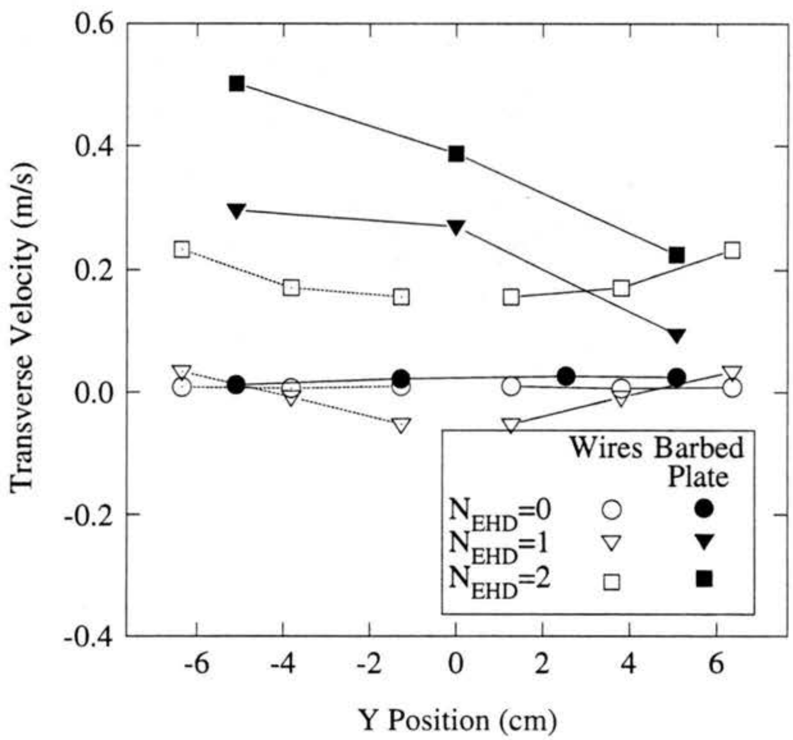

Figure 4.61. Averaged horizontal profiles of transverse particle velocities in the wire-plate and barbed plate precipitators.

$N_{EHD} = 2$, average transverse particle velocities near the ground plate (position Y = - 5.1 cm) in the barbed plate geometry are ≈ 0.5 m/s while velocities at the equivalent position in the wire-plate geometry are only ≈ 0.25 m/s.

4.4.5 Calculated Versus Measured Drift Velocities

Figures 4.62 through 4.65 are comparisons of measured transverse particle velocities and calculated expected drift velocities as a function of transverse position. The calculated particle drift velocities are based on local values of the electric field obtained from Figures 4.39 and 4.40 and the calculation techniques described in Section 3.4.1. Figures 4.62 and 4.63 are plots of transverse motion in the plane of a barb or wire and Figures 4.64 and 4.65 show average particle motion for a given transverse position. Figures 4.64 and 4.65 indicate that average transverse particle velocities are very close to the predicted particle drift velocities, particularly for the case of $N_{EHD} = 2$. Drift velocities are higher near the ground plate than they are near the electrode in both geometries because the transverse component of the electric field is on average higher near the ground plate than elsewhere (except immediately next to the discharge electrodes). In the wire-plate precipitator operating at $N_{EHD} = 1$, the average drift velocity remains near zero but exhibits the same expected spatial trend. This trend is a clear indication that corona induced secondary flows exist within the precipitator and are influencing particle motion. The particles in the wire-plate geometry at $N_{EHD} = 1$ are entrained in a secondary flow downstream of the wire that is clearly visible in Figure 4.53.

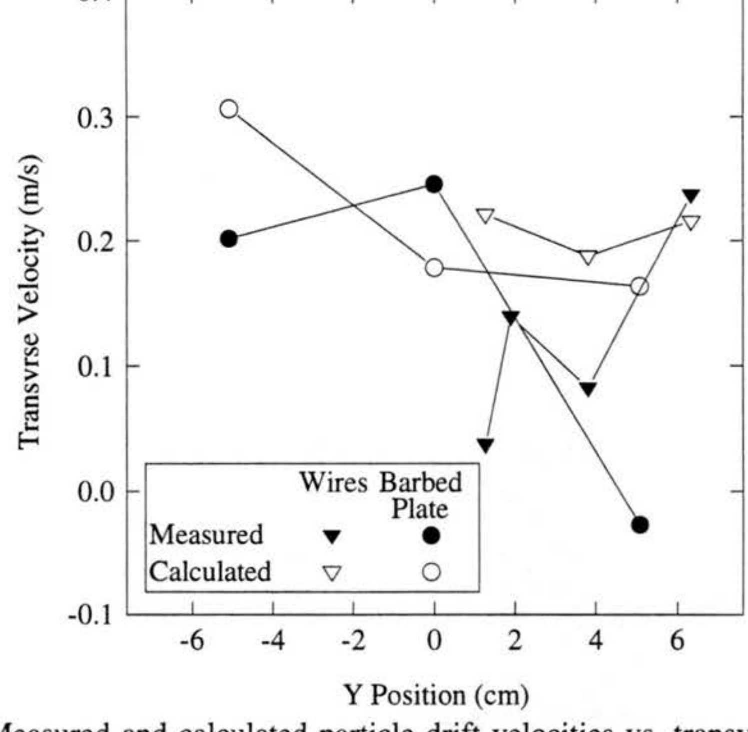

Figure 4.62. Measured and calculated particle drift velocities vs. transverse position in the plane of a barb or wire at $N_{EHD} = 1$.

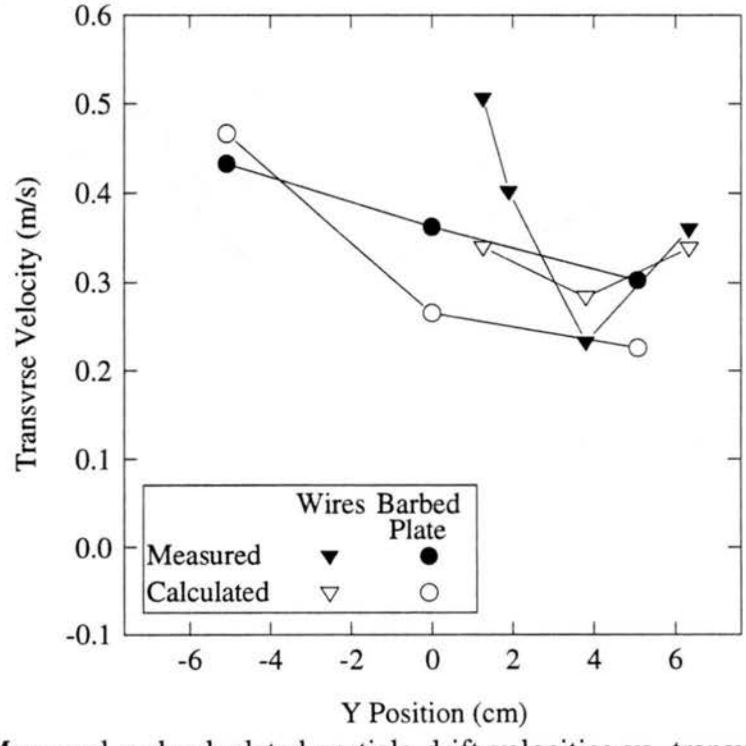

Figure 4.63. Measured and calculated particle drift velocities vs. transverse position in the plane of a barb or wire at $N_{EHD} = 2$.

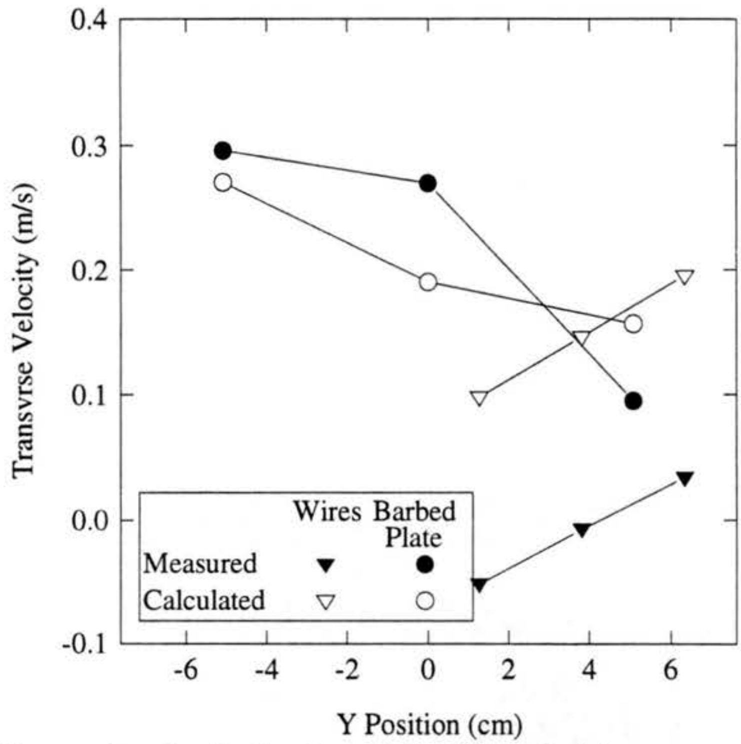

Figure 4.64. Measured and calculated particle drift velocities vs. transverse position averaged along the length of the precipitator at $N_{EHD} = 1$.

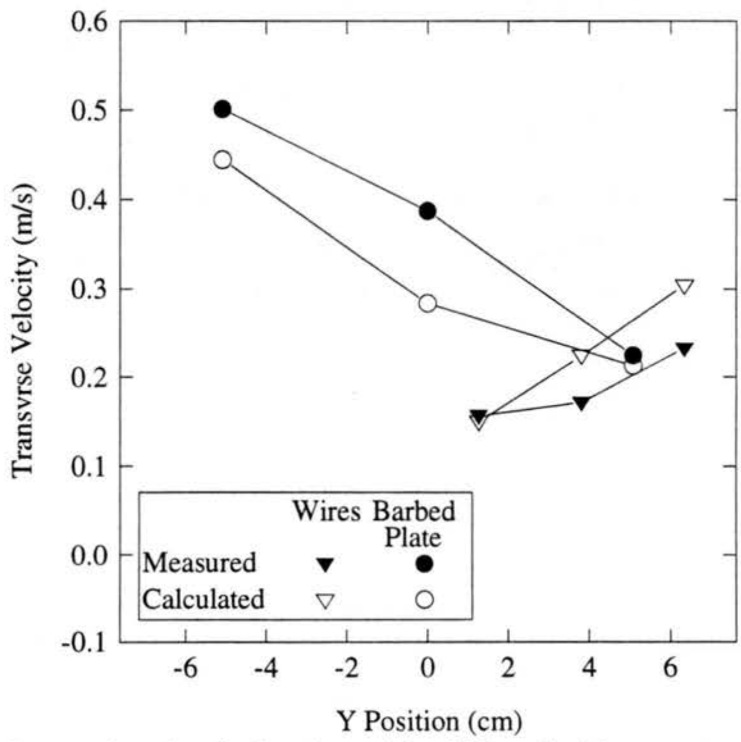

Figure 4.65. Measured and calculated particle drift velocities vs. transverse position averaged along the length of the precipitator at $N_{EHD} = 2$.

4.4.6 Integral Length Scales

Integral length scales are calculated as detailed in Section 3.4.3 and are averaged for both the streamwise and transverse velocity components. The average numbers are listed in Table 4.6 and plots of all integral length scale measurements are included in Appendix E. Streamwise and transverse integral length scales are similar in the two electrode geometries. The streamwise integral length scales for $N_{EHD} = 0$ are 0.26 m and 0.23 m for the barbed plate and wire-plate geometries, respectively. At $N_{EHD} = 1$, the wire-plate length scale is reduced to 0.016 m and the barbed plate length scale is reduced to 0.018 m due to the electrically generated turbulence. Streamwise integral length scales for $N_{EHD} = 2$ are almost identical to those at $N_{EHD} = 1$. The transverse integral length scales are on the order of 10^{-5} m at $N_{EHD} = 0$ for both geometries and are increased to the order of 10^{-3} m when $N_{EHD} = 1$ or $N_{EHD} = 2$. The barbed plate does not appear to offer any reduction in the length scales of particle motion when compared to the wire plate geometry.

Particle diffusivities, included in Table 4.6, indicate both streamwise and transverse particle difusivities are higher in the barbed plate geometry than they are in the wire-plate precipitator. This increase in mixing is normally asociated with more efficient particle charging.

4.5 Particle Collection

Photographs of the dust cake collected on the ground plate for each electrode geometry are presented in Figures 4.66 through 4.69. Each precipitator is operated at $N_{EHD} = 2$ for 1¼ hours with an inlet dust supply of 3.0×10^{-7} g/cm^3 of aluminum oxide.

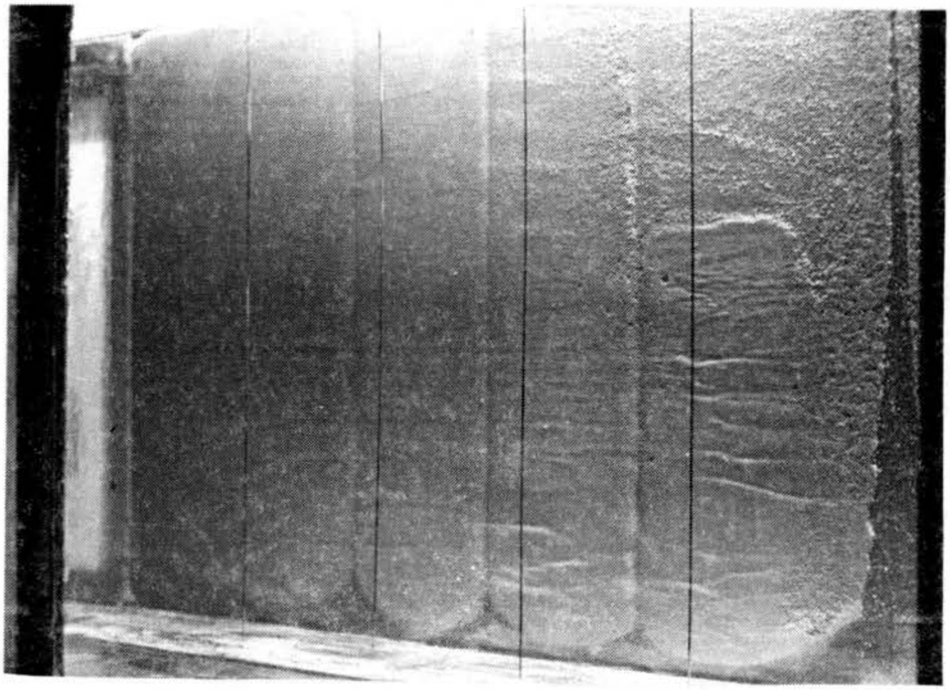

Figure 4.66. Particle deposition pattern for wire-plate precipitator operating at $N_{EHD} = 2$.

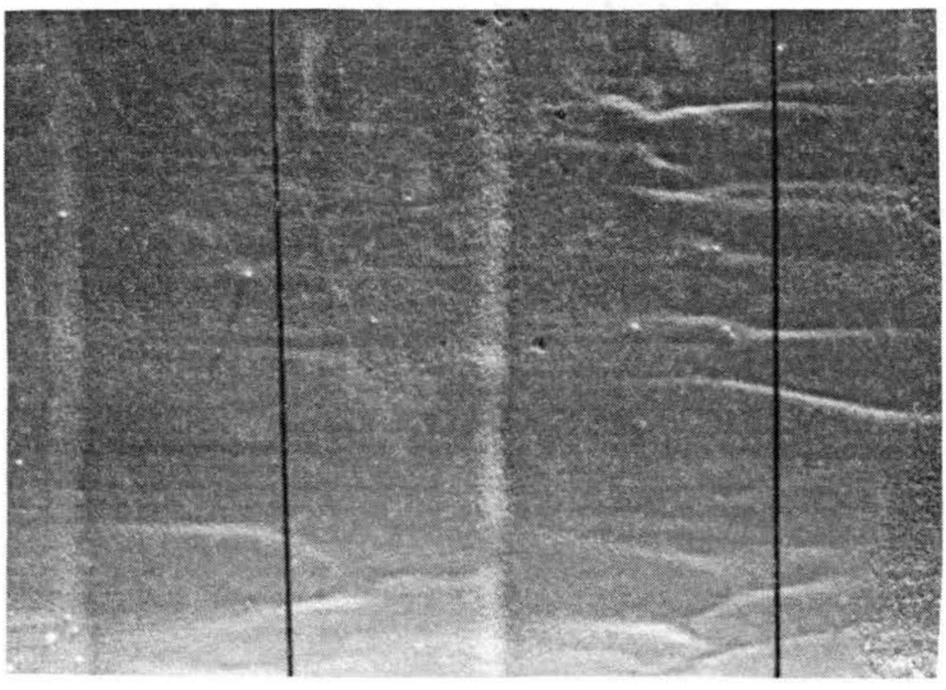

Figure 4.67. Close-up view of particle deposition pattern for wire-plate precipitator operating at $N_{EHD} = 2$.

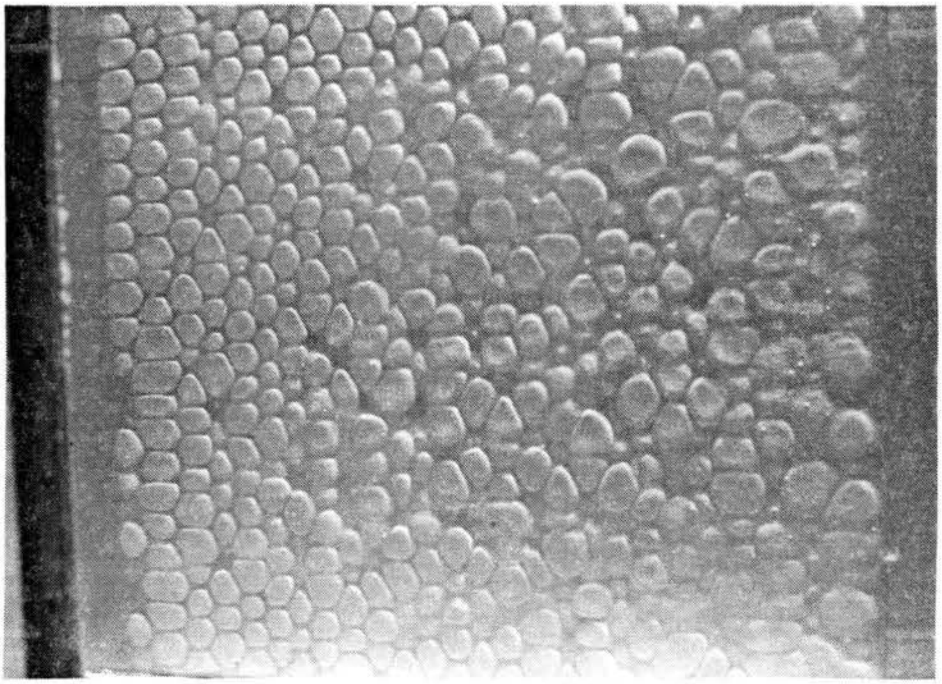

Figure 4.68. Particle deposition pattern for barbed plate precipitator operating at $N_{EHD} = 2$.

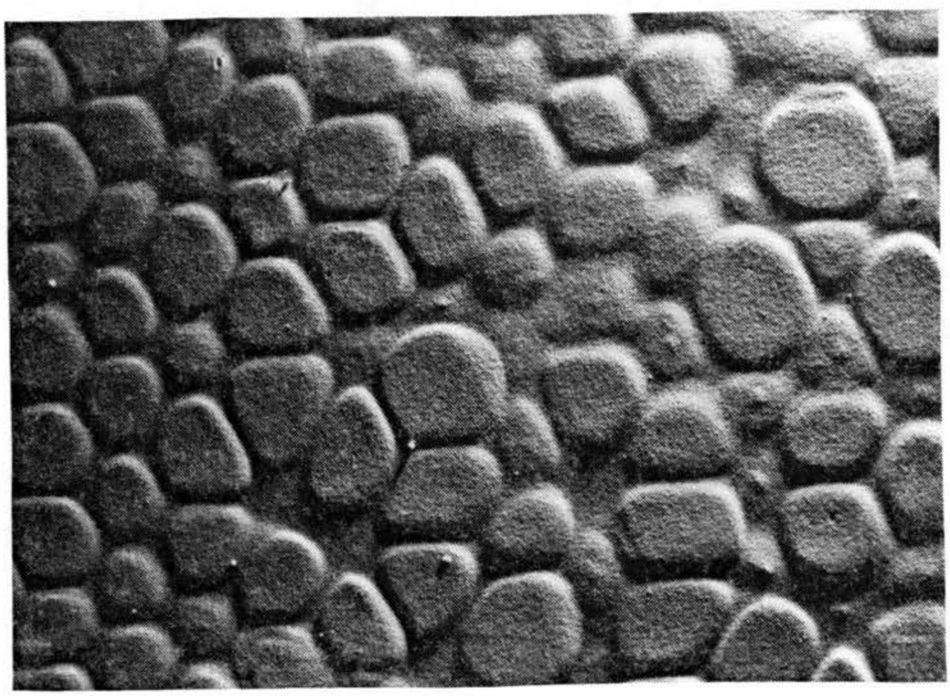

Figure 4.69. Close-up view particle deposition pattern for barbed plate precipitator operating at $N_{EHD} = 2$.

Figure 4.66 shows the ground plate at Y = -7.62 cm for the wire-plate geometry. The bulk flow passed from right to left in the photograph. The entrance section of the precipitator has a heavier build-up of particles than does the downstream end as might be expected. The thin regions of low current density between wires are clearly visible as locations where the dust cake is very thin. The lack of current in these areas allows any particles that arrive at the ground plate there to lose their charge and be easily re-entrained into the flow. The upper right corner of the plate shows evidence of scouring, where larger chunks of particles have been re-entrained into the flow. Figure 4.67 is a close-up view of the same plate and shows the same pattern observed in the copper plate oxidation experiments. Regions of low current between tufts fail to hold particles to the plate and the result is the rippled pattern of horizontal lines.

The ground plate collection pattern for the barbed plate is pictured in Figures 4.68 and 4.69. A pattern strikingly similar to the ground plate oxidation pattern is clearly visible. The pattern is more pronounced than the wire-plate pattern for two reasons: the regions of low and high current are more stable than in the wire-plate precipitator, and more dust is collected on the ground plate since there is only one plate. The upstream (right) portion of the pattern is less well defined than the downstream portion, indicating that the barbs near the entrance of the precipitator do not all discharge uniformly. Visual observation of the corona confirms that not all barbs discharge when the precipitator is dirty, particularly near the leading edge where the highest concentrations of particles are found. When the barbs are all cleaned, nearly all discharge, as indicated by the pattern near the downstream edge of the plate.

CHAPTER 5.0

CONCLUSIONS

This study is an investigation of a novel barbed plate electrode designed to reduce the spatial inhomogeneities of current density and electric field in electrostatic precipitators. The motivation behind study of the new design is poor collection of fine particles in conventional wire-plate precipitators. Poor collection in wire-plate precipitators is due primarily to two phenomena. Inadequate particle charging is caused by particle motion through areas of low current. Interruption of particle movement towards the collector plates is due to entrainment of particles in large scale flow disturbances caused by the nonuniform electric field. It was hypothesized that reduction of the distance between corona discharge tufts would reduce the scales of nonuniformity in electric field and electrically induced secondary flows and turbulence.

In the first phase of the study, the barbed plate electrode was optimized to provide the most uniform distribution of current density at the ground plate. The optimized design has 15.9 mm long barbs placed in a hexagonal grid at 27.0 mm intervals. Comparison of current density distributions of this optimized barbed plate to those of the wire-plate design confirms the superiority of the barbed plate in terms of electrical characteristics. Higher electric field strength over most of the inter-electrode space, due to the presence of the high voltage plate supporting the barbs, increases particle velocities in the direction perpendicular to the collection plates over those measured in a conventional precipitator.

The corona discharge in both the wire-plate and barbed plate geometries produces turbulence. The barbed plate produces 16 percent to 35 percent higher turbulence intensities than are present in the wire-plate precipitator. This increase in the magnitude of turbulence is not accompanied by a reduction in the measured scale of turbulence. There is, however, evidence of a large scale secondary flow in the wire-plate precipitator that is not present in the barbed plate precipitator. The equivalence of integral length scales in the two geometries may be partially caused by the fact that the electrode spacing in the barbed plate precipitator is twice that in the wire-plate arrangement. Future study of the barbed plate design should consider a smaller barbed plate-to-collector plate gap.

The most apparent benefit of the barbed plate discharge electrode may be more efficient particle charging. Higher particle diffusivities in the barbed plate geometry promote particle charging since particles can not easily sneak through areas of low current. In addition, in the barbed plate design, areas of low current are reduced in size. The barbed plate should serve as an excellent precharging section to a parallel plate precipitator.

Future experimental studies of the fluid mechanics of the barbed plate, or any electrode arrangement modelling industrial-scale precipitators, should be conducted in a flow channel sufficiently long to avoid entrance effects. Both flow visualization and laser Doppler anemometer measurements indicate caution must be used when interpreting data. The precipitator entrance effects measured in prior studies are not indicative of particle or gas motion in full-scale precipitators. Collection efficiencies should be measured in long test sections to compare barbed plate and wire-plate geometries.

REFERENCES

Atten, P., McCluskey, F., and Lahjomri, A (1985) Electrohydrodynamic Simulation of Electrostatic Precipitators. *IEEE Trans. Indus. Applications*, vol. 50A, pp. 1528-1533.

Atten, P., McCluskey, F., and Lahjomri, A. (1987) The Electrohydrodynamic Origin of Turbulence in Electrostatic Precipitators. *IEEE Trans. Indus. Applications*, vol. 1A-23 no. 4, pp. 705-711.

Bendat, J.S., and Piersol, A.G. (1971) *Random Data: Analysis and Measurement Procedures*, New York: Wiley.

Berstein, S., and Crowe, C.T. (1981) Interaction Between Electrostatics and Fluid Dynamics in Electrostatic Precipitators. *Environ. Intl.*, vol. 5, pp. 181-189.

Blier, B.H. (Jan. 19, 1971) Electrostatic Precipitator. U.S. Patent 3,555,818.

Boulloud, A. and Charrier, J. (1980) Current Density on the Plane Electrode of a Positive Point-to-Plane Glow Corona Discharge. *Proc. 6th Int. Conf. Gas Discharges*, pp. 110-113.

Bridge, J.H. (Oct. 9, 1906) Electrically Treating Air or Other Gases. U.S. Patent 832,767.

Chattock, A.P. (1899), On the Velocity and Mass of Ions in the Electric Wind in Air. *Phil. Mag. J. Sci.*, series 5, vol. 48, pp. 401-420.

Collins, L.F., Self, S.A., and Shearer, D.D. (1978) Point-Source Corona Current Distribution in an External Field. *IEEE Trans. Indus. App.*, vol. 14, pp. 506-509.

Davidson, J.H., and Shaughnessy, E.J. (1984a) An Electrostatic Precipitator Facility for Turbulence Research. *Proceedings of the Fifth Symp. on the Transfer and Utilization of Particulate Control Technology*, Kansas City, MO, 1984, (EPA/EPRI vol. 2, 30-12, Feb. 1986).

Davidson, J.H., and Shaughnessy, E.J. (1984b) Mean Velocity and Turbulence Intensity Profiles in a Large Scale Laboratory Precipitator. *ASME Joint Power Generation Conference*, Toronto, ASME paper no 84-JPGC-APC-1.

Davidson, J.H., Shaughnessy, E.J. (1986) Turbulence Generation by Electric Body Forces. *Exp.in Fluids*, vol. 4, pp. 17-26.

Davidson, J.H. and McKinney, P.J. (1989) Turbulent Mixing in a Barbed Plate-to-Plate Electrostatic Precipitator. *Atmos. Environ.*, vol. 23, pp. 2093-2107.

Davidson, J.H., and McKinney, P.J. (1990) Electrohydrodynamic Precipitator Flow With a Barbed Plate Discharge Electrode. *J. Aerosol Sci. and Tech.*, vol. 10, no. 4.

Davidson, J.H. and McKinney, P.J. (1991) EHD Flow Visualization in the Wire-Plate and Barbed Plate Electrostatic Precipitator," *IEEE Trans. Indus. App.*, vol. 27, pp 154-160, 1991.

Deutsh, W. (1922) *Ann. der Physik* vol. 68, pg. 335.

Flippen, L.D. (1982) Electrohydrodynamics, Ph.D. Dissertation, Duke University.

Feldman, P.L., Kumar, K.S., and Cooperman, G.D. (1977) Turbulent Diffusion in Electrostatic Precipitators. *AIChE Symp. Series*, vol. 165, no. 73, pp. 120-130.

Fortescue, C.G. (Aug. 29, 1922) Apparatus for Electrical Precipitation. U.S. Patent 1,427,370.

Goldman, A., Selim, E.O., and Waters, R.T. (1978) Current Distribution in the Negative Corona Discharge in Air. *Proc. 5th Int. Conf. Gas Discharges*, pp. 88-91.

Hauksbee, F. (1709) *Physico-Mechanical Experiments on Various Subjects*, 1st ed., London, 53-64.

Hinds, W.C. (1982) *Aerosol Technology Properties Behavior, and Measurement of Airborne Particles*, New York: John Wiley & Sons.

Kallio, G.A. and Stock, D.E. (1990) Flow Visualization Inside a Wire-Plate Electrostatic Precipitators. *IEEE Trans. Indus. App.*, vol. 36, no. 3, pp. 503-514.

Kallio, G.A. and Stock, D.E. (1992) Interaction of Electrostatic and Fluid Dynamic Fields in Wire-Plate Electrostatic Precipitators. *J. Fluid Mech.*, vol. 240, pp. 133-166.

Kondo, Y. and Miyoshi, Y. (1978) Pulseless Corona in Negative Point to Plane Gap. *Jap. J. App. Phys.*, vol. 17, pp. 643-649.

Larsen, P.S., and Christensen, E.M. (1986) Secondary Flow and Turbulence in Electrostatic Precipitators. *Third International Symposium on Applications of Laser Anemometry to Fluid Mechanics*, Lisbon, Portugal.

Larsen, P.S., and Sorensen, S.K. (1984) Effect of Secondary Flows and Turbulence on Electrostatic Precipitators. *Atmos. Environment*, vol. 18, pp. 1963-1967.

Lawless, P.A., McLean, K.J., Sparks, L.E., and Ramsey, G.H. (1986) Negative Corona in Wire-Plate Electrostatic Precipitators, Part I: Characteristics of Individual Tuft-Corona Discharges. *J. of Electrostatics* vol. 18, pp. 199-217.

Leonard, G.L., Mitchner, M., and Self, S.A. (1980) Particle Transport in Electrostatic Precipitators. *Atmos. Environment*, vol. 14, pp. 1289-1299.

Leonard, G.L., Mitchner, M., and Self, S.A. (1982) Experimental Study of the Effect of Turbulent Diffusion on Precipitator Efficiency. *J. Aerosol Sci.and Tech.*, vol. 13, no. 4, pp. 271-284.

Leonard, G.L., Mitchner, M., and Self, S.A.(1983) An Experimental Study of the Electrohydrodynamic Flow in Electrostatic Precipitators. *J. Fluid Mech.*, vol. 127, pp. 123-140.

Linnebur, P. (1993) Personal communication. Anticipated M.S. Thesis, Colorado State University.

Malik, M.R., Weinstein, L.M., and Hussaini M.Y., (1983) Ion Wind Drag Reduction. *AIAA 21st Aerospace Sci. Meeting.*

Masuda, S., Ayutsu, K., Kanno, Y., and Ko, M. (1979) Motion of Small Charge Particles Inside an Electrostatic Precipitator. *IEEE IAS Conference Record*, pp. 139-145.

McDonald, J.R., Smith, B.W., Spencer, H.W., and Sparks, L.E. (1977) A Mathematical Model for Calculating Electrical Conditions in Wire-Duct Electrostatic Precipitation Devices. *J. Applied Physics*, vol. 48, no. 6, pp. 2231-2243.

McKinney, P.J. (1988) Electrohydrodynamic Flow in a Barbed Plate Electrostatic Precipitator. M.S. Thesis, Colorado State University.

McKinney, P.J., and Davidson, J.H. (1988) Microcomputer Based Turbulent Flow Data Acquisition and Analysis - Asyst Extended. *Symposium on Small Computers for Fluid Mechanics Analysis and Research ASME Winter Annual Meeting*, Chicago.

McLean, K.J., Lawless, P.A., Sparks, L.E., and Ramsey, G.H., (1986) Negative Corona in Wire-Plate Electrostatic Precipitators, Part II: Calculation of Electrical Characteristics of Contaminated Discharge Electrodes. *J. Electrostatics*, vol. 18, pp. 219-231.

Peterson, R.J. (1993) Modification of a Turbulent Flow Field by Electrically Charged Particles Within an Electric Field. Ph.D dissertation, Civil Engineering, Colorado State University.

Ramadan, O.E., and Soo, S.L. (1969) Electrohydrodynamic Secondary Flow. *Phys. Fluids*, vol. 12, pp. 1943-1945.

Reist, P.C. (1984) *Introduction to Aerosol Science*, New York: MacMillan Publishing Company.

Riehle, C., and Loffler, F. (1990) Investigations of Particle Dynamics and Separation Efficiency of a Laboratory-Scale Electrostatic Precipitator using Laser-Doppler Velocimetry and Particle Light-Scattering Size Analysis. *The 4th International Conference on Electrostatic Precipitation*, Beijing, China.

Robertson, J.A. (Jan. 15, 1974) Apparatus and Method for Electrical Precipitation. U.S. Patent 3,785,118.

Robinson, M. (1961) Movement of Air in the Electric Wind of the Corona Discharge. *Trans. Am. inst. Electr. Eng.*, vol. 80 (Part 1), pp. 143-150.

Robinson, M. (1973) "Electrostatic Precipitation" in *Electrostatics and its Applications*, A.D. Moore, Ed., New York: John Wiley & Sons.

Robinson, M. (1975) Effects of the Corona Discharge on Electric-Wind Convection and Eddy Diffusion in an Electrostatic Precipitator. Ph.D. Dissertation, The Cooper Union University.

Self, S.A., Mitchner, M., Fisher, M.J., Gere, D.S., and Leach, R.N. (1981) Corona Discharge Structure and Its Influence on Precipitation and Reentrainment. *IEEE IAS Conference Record*, pp. 1128-1135.

Self, S.A., Kihm, K.D., and Mitchner, M. (1987) Precipitator Performance Improvement Through Turbulence Control. *3rd International Conference on Electrostatic Precipitation*, Avano/Venice, Italy.

Self, S.A., Mitchner, M.,and Kihm, K.D. (1988) Effects of Turbulence in Wire-Plate Precipitators. *7th EPA/EPRI Symposium on Particulate Control Technology*, Nashville.

Selim, E.O. and Waters, R.T. (1980) Electrical Characteristics of Negative Rod/Plane Corona in Air at Atmospheric Pressure and Below. *Proc. 6th Int. Conf. Gas Discharges*, pp. 146-149.

Shaughnessy, E.J., Davidson, J.H., and Hay, J.C. (1985) The Fluid Mechanics of Electrostatic Precipitators. *J. Aerosol Sci. and Tech.*, vol. 4, pp. 471-476.

Shaughnessy, E.J., Solomon, G.S. (1991) Electrohydrodynamic Pressure of the Point-to-Plane Corona Discharge. *J. Aerosol Sci. and Tech.*, vol. 14, pp. 193-200.

Shively, W.L., and Harlow, E.V. (Apr. 2, 1940) Gas Treating Apparatus. U.S. Patent 2,195,431.

Sigmond, R.S. (1982) Simple Approximate Treatment of Unipolar Space-Charge-Dominated Coronas: The Warburg Law and the Saturation Current. *J. Appl. Phys.*, vol. 52, pp. 891-898.

Sigmond, R.S. (1986) The Unipolar Space Charge Flow Problem. *J. Electrostatics*, vol. 18, pp. 249-272.

Steuernagel, W. (Apr. 1, 1969) Electrode Discharge Plate for Dust Collection. U.S. Patent 3,435,594.

Tassicker, O.J. (1969) Measurements of Corona Current at an Electrode Boundary. *Electron. Lett.*, vol. 5, pp. 285-286.

Tassicker, O.J. (1972) Aspects of Forces on Charged Particles in Electrostatic Precipitators. Ph.D. Thesis, University of New South Wales.

Ushimaru, K., Butler, G.W., and Milovsoroff, P. (1982) An Experimental and Theoretical Investigation of Electrostatic Precipitators. Rep. 219, Flow Industries, Kent, WA.

Warburg, E. (1899) *Weid. Ann.*, vol. 67, pg. 69.

White, H.J. (1963) *Industrial Electrostatic Precipitation*, Reading: Addison-Wesley Publishing.

Yabe, A., Mori, Y., and Nijikate, K. (1978) EHD Study of the Corona Wind Between Wire and Plate Electrodes. *AIAA Journal*, vol. 16, pp. 340-345.

Yamamoto, T., and Sparks, L.E. (1986) Numerical Simulation of Three-Dimensional Tuft Corona and Electrohydrodynamics. *IEEE Trans. Indus. Applications*, vol. 1A-22, no. 5, pp. 880-885.

Yamamoto, T., and Velkoff, H.R. (1981) Electrohydrodynamics in an Electrostatic Precipitator. *J. Fluid Mech.*, vol. 108, pp. 1-8.

APPENDIX A

GROUND PLATE CURRENT DENSITY DISTRIBUTION FOR A BARBED SCREEN

A design for a barbed screen has also been considered as a retrofit electrode for a wire-plate precipitator. A barbed screen could potentially provide the same uniform discharge pattern that the barbed plate does and provide a reasonably uniform electric field while not halving the channel width as does a barbed plate. Figure A.1 shows the ground plate oxidation pattern for a screen with 6.0 mm long barbs at a 25.4 mm square spacing. Figure A.2 shows the current density distribution at the ground plane beneath the center row of barbs for the same screen. Both figures indicate ground plane current density is very uniform. The primary difficulty with the barbed screen in the laboratory is the control of the dominant discharge of the edge barbs. The use of shorter barbs alone is not effective, but the addition of a section of plate at the screen's edge does have some beneficial effect. The design in then really a hybrid barbed screen/barbed plate.

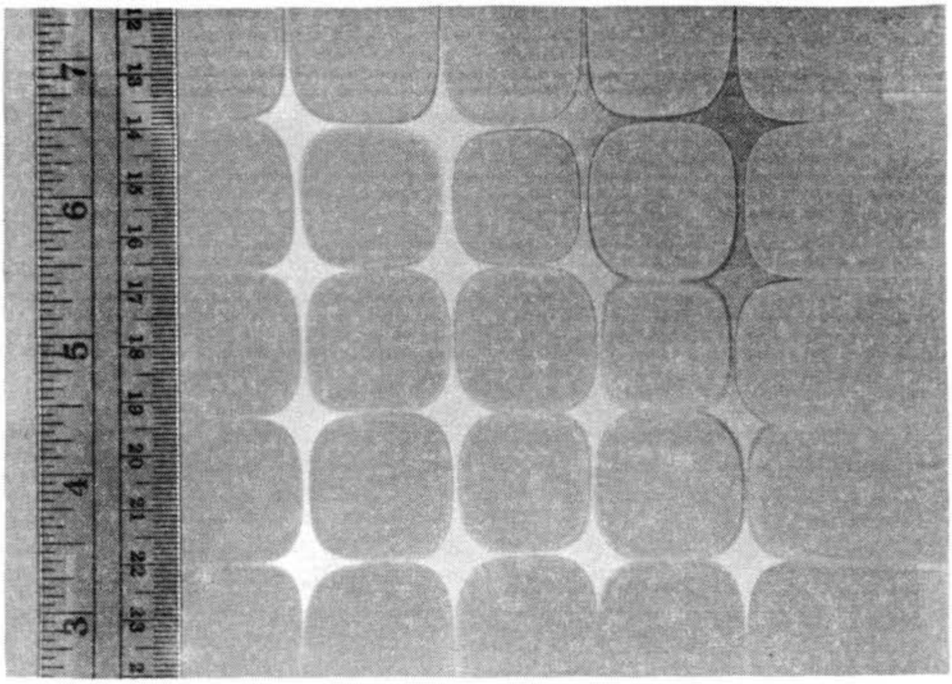

Figure A.1. Oxidation pattern of barbed screen.

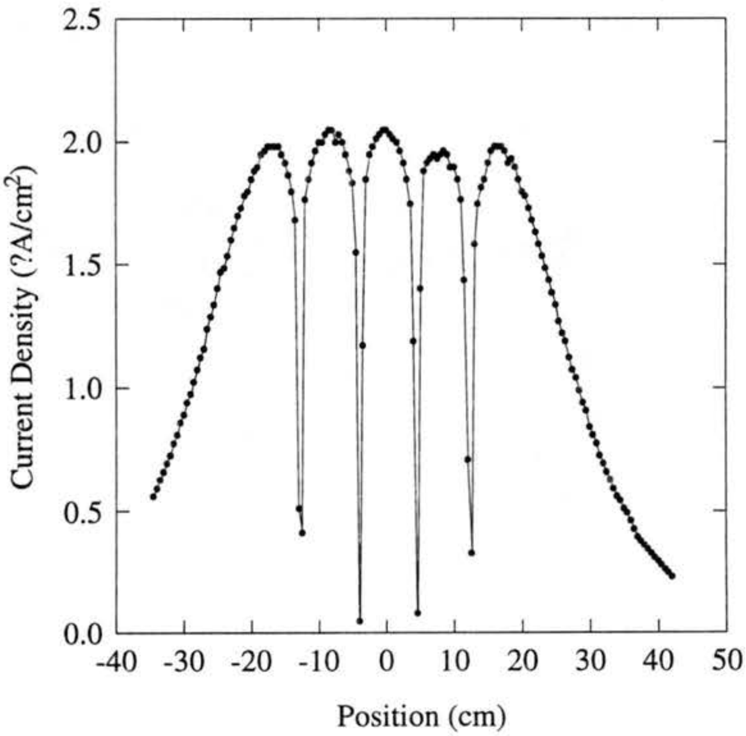

Figure A.2. Ground plate current density profile of barbed screen.

APPENDIX B

CALCULATED INTER-ELECTRODE CURRENT DENSITY AND ELECTRIC FIELD DISTRIBUTIONS FOR MODEL PRECIPITATORS AT $N_{EHD} = 2$

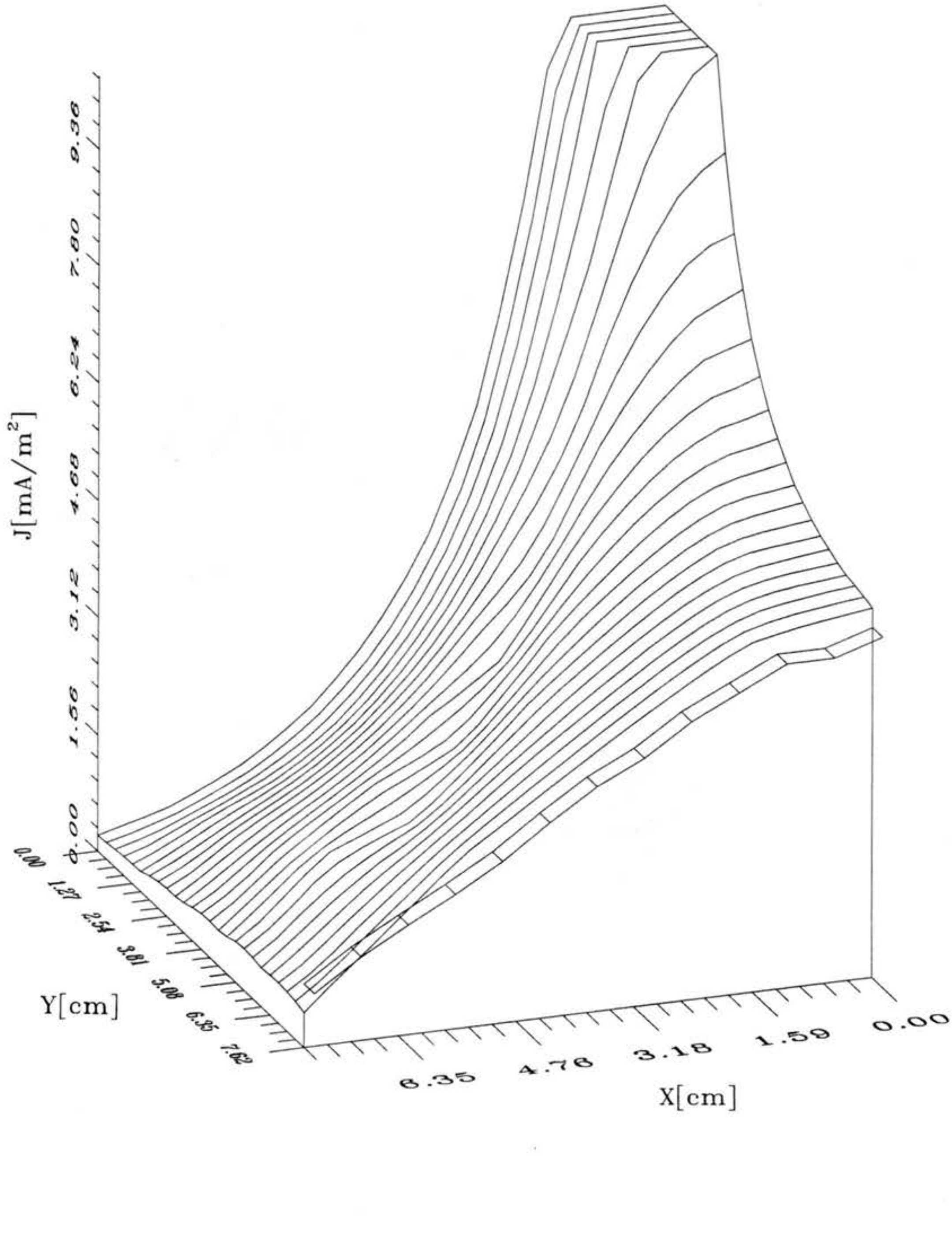

Figure B.1. Calculated current density distribution accross the inter-electrode space in the wire-plate configuration for $N_{EHD} = 2$. Peak current density at wire is 208 mA/m^2.

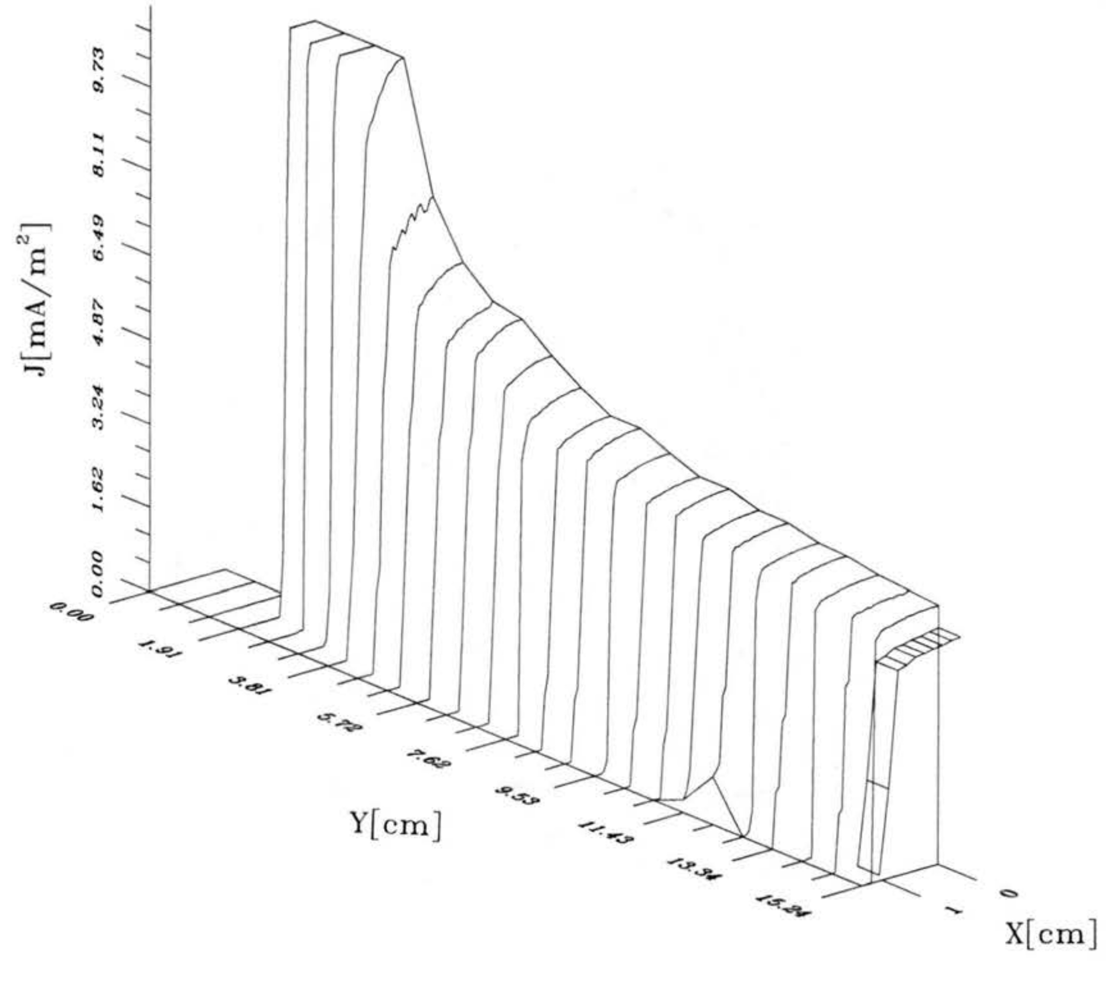

Figure B.2. Calculated current density distribution across the inter-electrode space in the barbed plate configuration for $N_{EHD} = 2$. Peak current density at barb tip is 25,288 mA/m^2.

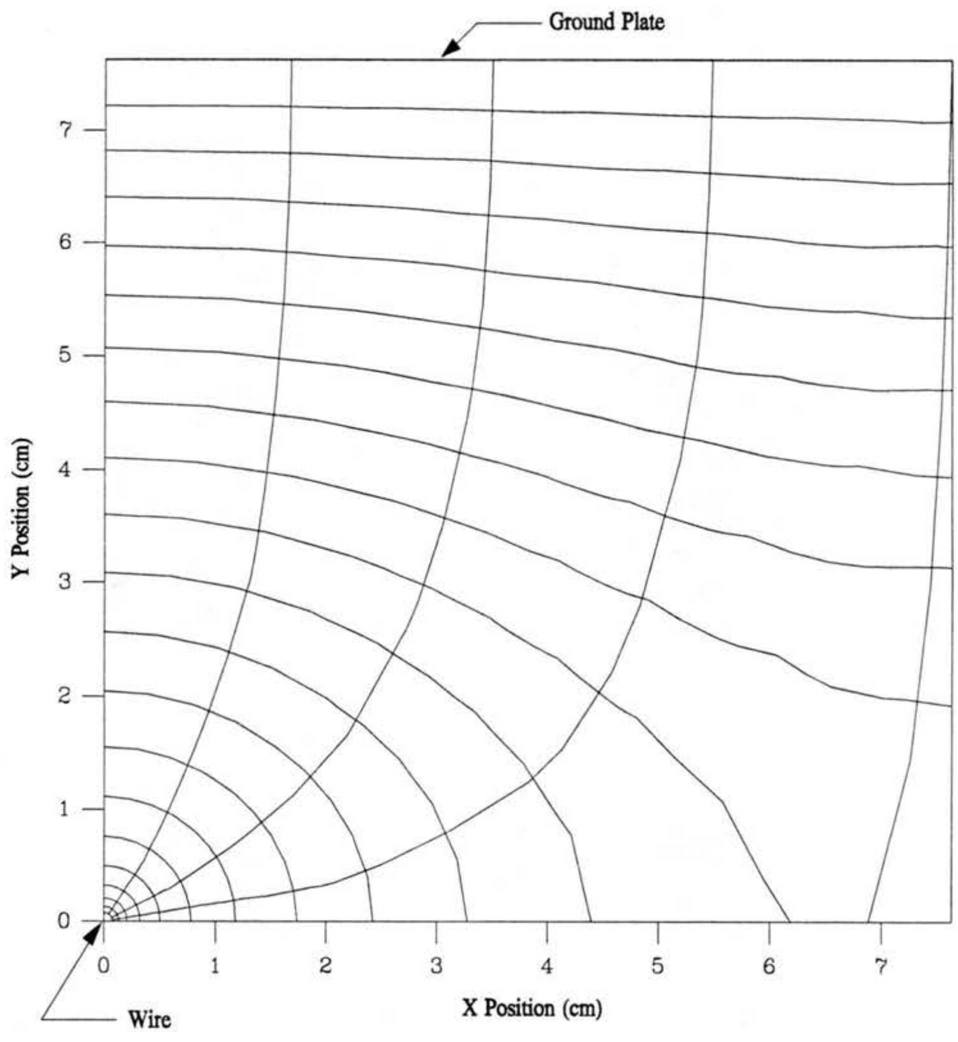

Figure B.3. Calculated electric potential and field lines across the inter-electrode space in the wire-plate configuration for N_{EHD} = 2. Contour interval is 2 kV.

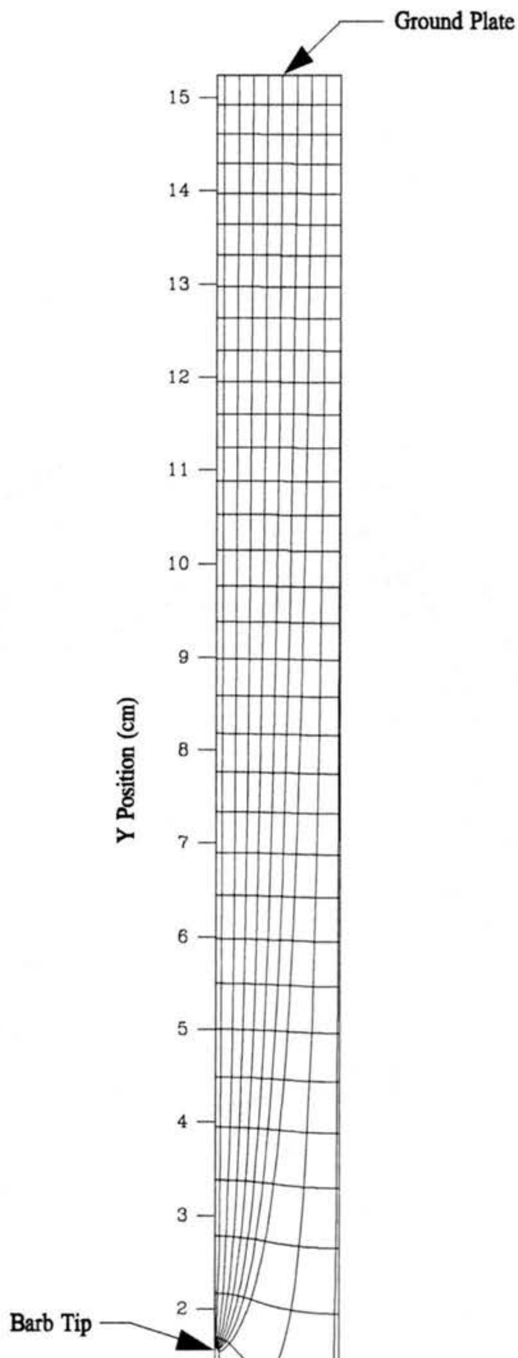

Figure B.4. Calculated electric potential and field lines across the inter-electrode space in the barbed plate configuration for N_{EHD} = 2. Contour interval is 2 kV.

APPENDIX C

LASER DOPPLER PARTICLE VELOCITY DATA

Table C.1. Particle velocity data for the wire-plate precipitator at $N_{EHD} = 0$.

	Global Coordinates		Shifted Coordinates		Streamwise (U)			Transverse (V)			Vector Sum
Data Point	X (cm)	Y (cm)	X (cm)	Y (cm)	U (m/s)	u_{rms} (m/s)	ℓ_x (m)	V (m/s)	v_{rms} (m/s)	ℓ_y (m)	rms (m)
1	-15.24	1.27	-7.62	1.27	0.987	1.75e-02	5.48e-02	4.76e-04	5.11e-03	1.27e-06	3.65e-02
2	-15.24	3.81	-7.62	3.81	1.02	1.65e-02	3.61e-01	-1.26e-03	3.33e-03	3.32e-06	3.37e-02
3	-15.24	6.35	-7.62	6.35	0.851	1.83e-02	5.20e-01	1.46e-03	5.21e-03	3.82e-06	3.81e-02
4	-12.7	1.27	-5.08	1.27	0.986	1.58e-02	5.97e-02	-9.95e-04	4.60e-03	2.65e-06	3.29e-02
5	-12.7	3.81	-5.08	3.81	1.01	1.58e-02	5.25e-02	3.81e-03	4.82e-03	9.96e-06	3.30e-02
6	-12.7	6.35	-5.08	6.35	0.915	1.70e-02	1.10e-01	7.29e-03	3.34e-03	1.95e-05	3.46e-02
7	-10.16	1.27	-2.54	1.27	0.966	1.67e-02	3.43e-01	8.72e-03	5.10e-03	2.30e-05	3.49e-02
8	-10.16	3.81	-2.54	3.81	1.01	1.48e-02	1.66e-01	6.22e-03	4.01e-03	1.62e-05	3.07e-02
9	-10.16	6.35	-2.54	6.35	0.836	2.09e-02	1.28e+00	7.87e-03	5.88e-03	2.09e-05	4.34e-02
10	-7.62	1.27	0	1.27	0.97	1.43e-02	5.41e-02	2.67e-02	9.49e-03	7.31e-05	3.43e-02
11	-7.62	1.905	0	1.905	0.976	1.44e-02	4.57e-02	1.54e-02	4.57e-03	4.10e-05	3.02e-02
12	-7.62	3.81	0	3.81	0.997	1.32e-02	4.93e-02	7.84e-03	3.14e-03	2.10e-05	2.71e-02
13	-7.62	6.35	0	6.35	0.798	1.88e-02	9.00e-01	8.19e-03	3.41e-03	2.13e-05	3.82e-02
14	-5.08	1.27	2.54	1.27	0.955	1.61e-02	1.74e-02	7.11e-03	5.13e-03	2.00e-05	3.38e-02
15	-5.08	3.81	2.54	3.81	0.984	1.38e-02	2.32e-02	4.27e-03	3.51e-03	1.13e-05	2.85e-02
16	-5.08	6.35	2.54	6.35	0.724	1.73e-02	9.65e-02	8.75e-03	4.08e-03	2.30e-05	3.55e-02
17	-2.54	1.27	5.08	1.27	0.932	1.30e-02	4.64e-02	1.02e-02	5.30e-03	2.89e-05	2.81e-02
18	-2.54	3.81	5.08	3.81	0.968	1.35e-02	2.07e-02	7.59e-03	4.14e-03	1.97e-05	2.82e-02
19	-2.54	6.35	5.08	6.35	0.758	1.62e-02	3.30e-01	8.26e-03	5.48e-03	2.15e-05	3.42e-02
20	0	1.27	7.62	1.27	0.912	1.40e-02	3.80e-02	9.25e-03	5.30e-03	2.75e-05	2.99e-02
21	0	3.81	7.62	3.81	0.945	1.34e-02	1.82e-02	9.22e-03	6.77e-03	2.48e-05	3.00e-02
22	0	6.35	7.62	6.35	0.745	1.74e-02	1.14e+00	1.18e-02	6.49e-03	3.18e-05	3.71e-02

Table C.2. Particle velocity data for the barbed plate precipitator at $N_{EHD} = 0$.

	Global Coordinates		Shifted Coordinates		Streamwise (U)			Transverse (V)			Vector Sum
Data Point	X (cm)	Y (cm)	X (cm)	Y (cm)	U (m/s)	u_{rms} (m/s)	ℓ_x (m)	V (m/s)	v_{rms} (m/s)	ℓ_y (m)	rms (m/s)
1	-8.255	-5.08	-6.93471	-5.08	1.01	2.05e-02	5.16e-01	9.22e-03	4.16e-03	2.45e-05	4.18e-02
2	-8.255	-1.27	-6.93471	-1.27	1.02	1.82e-02	2.02e-01	1.99e-02	4.19e-03	5.25e-05	3.74e-02
3	-8.255	2.54	-6.93471	2.54	1.03	1.76e-02	1.93e-01	2.47e-02	4.77e-03	6.58e-05	3.65e-02
4	-8.255	5.08	-6.93471	5.08	1.05	1.75e-02	1.62e-01	2.24e-02	3.68e-03	6.11e-05	3.58e-02
5	-5.9436	-5.08	-4.62331	-5.08	1	1.75e-02	1.82e-01	1.37e-02	3.19e-03	3.68e-05	3.56e-02
6	-5.9436	-1.27	-4.62331	-1.27	1.01	1.71e-02	3.36e-01	2.12e-02	4.39e-03	5.58e-05	3.53e-02
7	-5.9436	2.54	-4.62331	2.54	1.03	1.67e-02	1.20e-01	2.79e-02	4.86e-03	7.52e-05	3.48e-02
8	-5.9436	5.08	-4.62331	5.08	1.04	1.64e-02	5.26e-02	2.41e-02	4.04e-03	6.65e-05	3.38e-02
9	-3.6576	-5.08	-2.33731	-5.08	1.01	2.53e-02	5.91e-01	1.81e-02	3.76e-03	4.82e-05	5.12e-02
10	-3.6576	-1.27	-2.33731	-1.27	1.01	1.95e-02	4.60e-01	2.44e-02	3.83e-03	6.41e-05	3.97e-02
11	-3.6576	2.54	-2.33731	2.54	1.03	2.07e-02	3.56e-01	3.15e-02	5.57e-03	8.30e-05	4.29e-02
12	-3.6576	5.08	-2.33731	5.08	1.04	1.55e-02	2.30e-02	2.21e-02	4.44e-03	6.22e-05	3.22e-02
13	-1.3462	-5.08	-0.02591	-5.08	1.01	1.90e-02	2.49e-01	1.02e-02	3.38e-03	2.78e-05	3.86e-02
14	-1.3462	-1.27	-0.02591	-1.27	1.01	1.66e-02	1.48e-01	2.12e-02	4.42e-03	5.54e-05	3.44e-02
15	-1.3462	2.54	-0.02591	2.54	1.02	2.11e-02	1.80e-02	2.58e-02	8.21e-03	6.97e-05	4.53e-02
16	-1.3462	5.08	-0.02591	5.08	1.02	1.97e-02	4.90e-01	2.46e-02	5.72e-03	6.87e-05	4.10e-02
17	0.9652	-5.08	2.285492	-5.08	1.01	1.76e-02	1.45e-01	1.16e-02	3.85e-03	3.19e-05	3.60e-02
18	0.9652	-1.27	2.285492	-1.27	0.999	1.95e-02	7.15e-02	2.57e-02	3.09e-03	7.06e-05	3.95e-02
19	0.9652	2.54	2.285492	2.54	1.03	1.92e-02	3.35e-01	2.25e-02	3.35e-03	6.15e-05	3.90e-02
20	0.9652	5.08	2.285492	5.08	1.03	1.62e-02	2.39e-02	3.02e-02	4.02e-03	8.88e-05	3.34e-02

Table C.3. Particle velocity data for the wire-plate precipitator at $N_{EHD} = 1$.

	Global Coordinates		Shifted Coordinates		Streamwise (U)			Transverse (V)			Vector Sum
Data Point	X (cm)	Y (cm)	X (cm)	Y (cm)	U (m/s)	u_{rms} (m/s)	ℓ_x (m)	V (m/s)	v_{rms} (m/s)	ℓ_y (m)	rms (m/s)
1	-15.24	1.27	-7.62	1.27	0.639	1.79e-01	9.19e-03	-1.43e-01	1.43e-01	1.35e-03	4.58e-01
2	-15.24	3.81	-7.62	3.81	1.04	4.57e-02	1.27e-02	2.12e-02	9.36e-02	4.04e-04	2.08e-01
3	-15.24	6.35	-7.62	6.35	1.07	7.59e-02	6.76e-02	9.28e-02	1.02e-01	2.00e-02	2.54e-01
4	-12.7	1.27	-5.08	1.27	0.645	1.72e-01	9.93e-03	-6.14e-02	1.63e-01	5.98e-04	4.74e-01
5	-12.7	3.81	-5.08	3.81	1.01	5.44e-02	1.23e-02	1.23e-02	6.59e-02	1.60e-04	1.71e-01
6	-12.7	6.35	-5.08	6.35	1.01	1.03e-01	2.54e-02	9.85e-03	6.93e-02	2.29e-04	2.48e-01
7	-10.16	1.27	-2.54	1.27	0.808	1.50e-01	9.64e-03	4.02e-02	1.43e-01	3.77e-04	4.14e-01
8	-10.16	3.81	-2.54	3.81	1.06	7.62e-02	1.54e-02	3.44e-02	8.76e-02	6.14e-04	2.32e-01
9	-10.16	6.35	-2.54	6.35	0.978	1.16e-01	3.14e-02	5.14e-02	5.75e-02	1.21e-03	2.59e-01
10	-7.62	1.27	0	1.27	0.841	2.47e-01	1.29e-02	3.74e-02	2.93e-01	4.37e-04	7.66e-01
11	-7.62	1.905	0	1.905	0.843	1.89e-01	8.71e-03	1.39e-01	2.54e-01	1.61e-03	6.33e-01
12	-7.62	3.81	0	3.81	0.881	1.42e-01	1.25e-02	8.21e-02	1.63e-01	8.42e-04	4.32e-01
13	-7.62	6.35	0	6.35	0.96	1.21e-01	1.65e-02	2.37e-01	1.29e-01	4.67e-03	3.54e-01
14	-5.08	1.27	2.54	1.27	0.824	2.13e-01	1.25e-02	-1.05e-01	2.86e-01	1.55e-03	7.13e-01
15	-5.08	3.81	2.54	3.81	0.923	1.38e-01	1.06e-02	3.69e-02	1.83e-01	3.81e-04	4.58e-01
16	-5.08	6.35	2.54	6.35	1.02	1.27e-01	1.71e-02	1.82e-01	1.25e-01	2.64e-03	3.56e-01
17	-2.54	1.27	5.08	1.27	0.733	1.90e-01	1.09e-02	-2.25e-02	1.74e-01	2.28e-04	5.15e-01
18	-2.54	3.81	5.08	3.81	0.876	1.55e-01	1.26e-02	6.11e-02	1.74e-01	6.20e-04	4.66e-01
19	-2.54	6.35	5.08	6.35	1.07	1.47e-01	1.88e-02	-7.52e-02	1.15e-01	1.20e-03	3.73e-01
20	0	1.27	7.62	1.27	0.523	2.57e-01	1.29e-02	-2.01e-01	2.33e-01	2.62e-03	6.94e-01
21	0	3.81	7.62	3.81	0.917	1.92e-01	3.57e-02	-2.71e-01	2.00e-01	2.78e-03	5.54e-01
22	0	6.35	7.62	6.35	1.1	1.37e-01	1.39e-02	-2.01e-01	1.20e-01	3.77e-03	3.64e-01

Table C.4. Particle velocity data for the barbed plate precipitator at N_{EHD} = 1.

	Global Coordinates		Shifted Coordinates		Streamwise (U)			Transverse (V)			Vector Sum
Data Doint	X (cm)	Y (cm)	X (cm)	Y (cm)	U (m/s)	u_{rms} (m/s)	ℓ_x (m/s)	V (m/s)	v_{rms} (m/s)	ℓ_y (m)	rms (m/s)
1	-12.7508	-5.08	-21.0058	-5.08	0.553	2.75e-01	1.55e-02	2.29e-01	3.08e-01	6.55e-03	8.26e-01
2	-12.7508	0	-21.0058	0	0.916	1.63e-01	2.52e-02	-7.88e-02	1.35e-01	1.42e-03	4.23e-01
3	-12.7508	5.08	-21.0058	5.08	1.34	8.50e-02	3.92e+00	5.85e-03	7.24e-02	2.30e-03	2.23e-01
4	-9.1948	-5.08	-17.4498	-5.08	0.495	2.66e-01	1.23e-02	-1.78e-01	3.21e-01	4.73e-03	8.34e-01
5	-9.1948	0	-17.4498	0	0.794	2.11e-01	1.69e-02	-5.36e-02	1.65e-01	6.25e-04	5.36e-01
6	-9.1948	5.08	-17.4498	5.08	1.3	6.91e-02	6.18e+00	-2.81e-02	9.04e-02	3.35e-02	2.28e-01
7	-5.715	-5.08	-13.97	-5.08	0.464	2.95e-01	1.24e-02	1.95e-01	2.92e-01	4.89e-03	8.30e-01
8	-5.715	0	-13.97	0	1.23	2.73e-01	4.49e-02	4.10e-01	2.07e-01	1.46e-02	6.85e-01
9	-5.715	5.08	-13.97	5.08	1.13	1.31e-01	7.15e-02	4.70e-01	9.60e-02	8.91e-02	3.25e-01
10	-2.2098	-5.08	-10.4648	-5.08	0.434	2.97e-01	1.49e-02	1.78e-01	2.79e-01	3.86e-03	8.15e-01
11	-2.2098	0	-10.4648	0	1.21	2.07e-01	1.99e-02	1.27e-01	1.49e-01	1.28e-03	5.10e-01
12	-2.2098	5.08	-10.4648	5.08	1.22	9.04e-02	1.12e-02	2.06e-01	8.26e-02	2.84e-02	2.45e-01
13	1.27	-5.08	-6.985	-5.08	0.548	2.67e-01	1.19e-02	5.53e-01	2.37e-01	6.08e-03	7.14e-01
14	1.27	0	-6.985	0	0.976	2.08e-01	1.45e-02	3.43e-01	1.73e-01	3.25e-03	5.41e-01
15	1.27	5.08	-6.985	5.08	1.22	1.05e-01	4.53e-02	1.64e-01	8.62e-02	4.51e-03	2.72e-01
16	4.445	0	-3.81	0	1.07	1.73e-01	2.01e-02	2.82e-01	1.72e-01	4.35e-03	4.88e-01
17	4.445	5.08	-3.81	5.08	1.13	1.45e-01	3.03e-02	9.03e-02	1.38e-01	2.23e-03	4.00e-01
18	4.7752	-5.08	-3.4798	-5.08	0.684	2.45e-01	1.55e-02	2.33e-01	2.31e-01	2.14e-03	6.73e-01
19	8.255	-5.08	0	-5.08	0.665	2.19e-01	1.57e-02	2.52e-01	1.94e-01	2.26e-03	5.85e-01
20	8.255	0	0	0	1.12	2.14e-01	1.49e-02	1.66e-01	1.97e-01	1.43e-03	5.82e-01
21	8.255	5.08	0	5.08	1.14	1.69e-01	1.98e-02	-3.03e-03	1.60e-01	5.24e-05	4.65e-01
22	8.89	6.0452	0.635	6.0452	0.894	1.79e-01	1.56e-02	-3.62e-02	1.53e-01	2.59e-04	4.71e-01
23	10.6172	6.0452	2.3622	6.0452	1.09	1.83e-01	2.00e-02	1.27e-01	1.56e-01	8.51e-04	4.81e-01
24	11.7856	-5.08	3.5306	-5.08	0.741	1.96e-01	1.28e-02	2.41e-01	2.44e-01	4.37e-03	6.26e-01
25	11.7856	0	3.5306	0	1.06	2.18e-01	1.55e-02	3.13e-01	2.10e-01	3.31e-03	6.05e-01
26	11.7856	5.08	3.5306	5.08	1.11	1.51e-01	7.71e-03	2.50e-01	2.33e-01	2.83e-03	5.55e-01
27	12.3698	6.0452	4.1148	6.0452	1.1	1.86e-01	1.01e-02	-4.40e-02	1.81e-01	2.86e-04	5.19e-01
28	15.2908	-5.08	7.0358	-5.08	0.804	1.91e-01	1.56e-02	2.02e-01	2.29e-01	2.26e-03	5.96e-01
29	15.2908	0	7.0358	0	1.07	1.90e-01	1.20e-02	2.46e-01	1.92e-01	3.04e-03	5.40e-01
30	15.2908	5.08	7.0358	5.08	1.12	1.81e-01	1.44e-02	-2.72e-02	1.85e-01	2.75e-04	5.18e-01

Table C.5. Particle velocity data for the wire-plate precipitator at $N_{EHD} = 2$.

	Global Coordinates		Shifted Coordinates		Streamwise (U)			Transverse (V)			Vector Sum
Data Point	X (cm)	Y (cm)	X (cm)	Y (cm)	U (m/s)	u_{rms} (m/s)	ℓ_x (m)	V (m/s)	v_{rms} (m/s)	ℓ_y (m)	rms
1	-15.24	1.27	-7.62	1.27	0.865	1.73e-01	8.79e-03	5.16e-02	1.94e-01	4.76e-04	5.20e-01
2	-15.24	3.81	-7.62	3.81	0.965	1.60e-01	9.10e-03	1.70e-01	2.27e-01	3.47e-03	5.55e-01
3	-15.24	6.35	-7.62	6.35	0.909	1.77e-01	1.79e-02	2.15e-01	2.56e-01	6.11e-03	6.22e-01
4	-12.7	1.27	-5.08	1.27	0.87	1.60e-01	7.52e-03	3.34e-02	1.83e-01	2.79e-04	4.86e-01
5	-12.7	3.81	-5.08	3.81	0.945	1.40e-01	8.57e-03	7.25e-02	1.86e-01	9.19e-04	4.66e-01
6	-12.7	6.35	-5.08	6.35	0.9	1.52e-01	1.41e-02	6.66e-02	2.09e-01	1.75e-03	5.17e-01
7	-10.16	1.27	-2.54	1.27	0.707	2.00e-01	1.29e-02	1.86e-01	1.74e-01	1.68e-03	5.30e-01
8	-10.16	3.81	-2.54	3.81	0.908	1.59e-01	1.07e-02	2.51e-01	1.78e-01	1.16e-02	4.77e-01
9	-10.16	6.35	-2.54	6.35	0.945	1.62e-01	1.67e-02	3.20e-01	2.23e-01	4.98e-03	5.51e-01
10	-7.62	1.27	0	1.27	0.893	3.08e-01	1.72e-02	5.06e-01	2.89e-01	5.17e-03	8.45e-01
11	-7.62	1.905	0	1.905	0.892	2.12e-01	1.02e-02	4.02e-01	2.39e-01	4.02e-03	6.39e-01
12	-7.62	3.81	0	3.81	0.912	1.37e-01	8.46e-03	2.32e-01	1.66e-01	2.46e-03	4.30e-01
13	-7.62	6.35	0	6.35	0.952	1.43e-01	1.92e-02	3.60e-01	1.42e-01	6.46e-03	4.03e-01
14	-5.08	1.27	2.54	1.27	0.786	2.33e-01	1.14e-02	1.16e-01	2.01e-01	1.09e-03	6.15e-01
15	-5.08	3.81	2.54	3.81	0.975	1.39e-01	9.04e-03	2.41e-01	1.78e-01	2.67e-03	4.52e-01
16	-5.08	6.35	2.54	6.35	0.996	2.01e-01	1.98e-02	2.93e-01	2.29e-01	3.79e-02	6.09e-01
17	-2.54	1.27	5.08	1.27	0.766	1.62e-01	1.08e-02	6.85e-02	1.44e-01	5.31e-04	4.33e-01
18	-2.54	3.81	5.08	3.81	0.95	1.19e-01	7.41e-03	1.39e-01	1.71e-01	1.65e-03	4.17e-01
19	-2.54	6.35	5.08	6.35	1.04	1.35e-01	1.02e-01	2.26e-01	1.41e-01	3.00e-03	3.90e-01
20	0	1.27	7.62	1.27	0.723	1.33e-01	1.01e-02	2.81e-02	1.21e-01	2.21e-04	3.60e-01
21	0	3.81	7.62	3.81	0.889	1.20e-01	8.34e-03	9.17e-02	1.58e-01	6.48e-04	3.97e-01
22	0	6.35	7.62	6.35	1.04	1.13e-01	1.14e-02	1.30e-01	1.40e-01	1.42e-03	3.60e-01

Table C.6. Particle velocity data for the barbed plate precipitator at N_{EHD} = 2.

	Global Coordinates		Shifted Coordinates		Streamwise (U)			Transverse (V)			Vector Sum
Data Point	X (cm)	Y (cm)	X (cm)	Y (cm)	U (m/s)	u_{rms} (m/s)	ℓ_x (m)	V (m/s)	v_{rms} (m/s)	ℓ_y (m)	rms
1	-12.7508	-5.08	-21.0058	-5.08	-0.119	3.31e-01	5.27e-03	5.11e-01	3.41e-01	1.74e-02	9.50e-01
2	-12.7508	0	-21.0058	0	0.922	3.69e-01	3.98e-02	2.45e-01	2.63e-01	3.14e-03	9.06e-01
3	-12.7508	5.08	-21.0058	5.08	1.41	2.16e-01	4.43e-02	-1.59e-01	2.07e-01	2.58e-03	5.98e-01
4	-9.1948	-5.08	-17.4498	-5.08	-0.0222	3.25e-01	1.17e-03	3.16e-01	2.64e-01	6.35e-03	8.37e-01
5	-9.1948	0	-17.4498	0	0.896	3.62e-01	2.25e-02	7.54e-02	2.86e-01	8.58e-04	9.23e-01
6	-9.1948	5.08	-17.4498	5.08	1.27	4.15e-01	4.53e-02	-7.35e-02	3.54e-01	1.19e-03	1.09e+00
7	-5.715	-5.08	-13.97	-5.08	0.447	2.58e-01	1.27e-02	5.54e-01	2.49e-01	8.96e-03	7.17e-01
8	-5.715	0	-13.97	0	0.853	3.21e-01	1.75e-02	4.22e-01	2.65e-01	3.84e-03	8.33e-01
9	-5.715	5.08	-13.97	5.08	1.42	2.99e-01	3.89e-02	3.99e-01	2.69e-01	5.20e-03	8.04e-01
10	-2.2098	-5.08	-10.4648	-5.08	0.464	3.38e-01	1.54e-02	3.22e-01	3.33e-01	5.98e-03	9.49e-01
11	-2.2098	0	-10.4648	0	0.657	3.86e-01	1.79e-02	2.13e-02	3.92e-01	3.21e-04	1.10e+00
12	-2.2098	5.08	-10.4648	5.08	1.29	2.32e-01	2.31e-02	1.93e-01	1.76e-01	1.31e-03	5.82e-01
13	1.27	-5.08	-6.985	-5.08	0.625	3.05e-01	1.33e-02	5.57e-01	3.25e-01	8.34e-03	8.91e-01
14	1.27	0	-6.985	0	1	3.08e-01	2.40e-02	3.98e-01	2.86e-01	2.99e-03	8.41e-01
15	1.27	5.08	-6.985	5.08	1.24	1.95e-01	1.71e-02	5.15e-01	2.56e-01	2.37e-02	6.44e-01
16	1.3208	6.0452	-6.9342	6.0452	0.931	2.49e-01	1.44e-02	1.72e-01	2.44e-01	1.24e-03	6.97e-01
17	4.7752	-5.08	-3.4798	-5.08	0.771	2.64e-01	1.27e-02	3.93e-01	2.62e-01	3.63e-03	7.44e-01
18	4.7752	0	-3.4798	0	1.1	2.51e-01	1.73e-02	3.60e-01	2.87e-01	3.17e-03	7.63e-01
19	4.7752	5.08	-3.4798	5.08	1.07	2.44e-01	1.61e-02	1.53e-04	2.34e-01	1.48e-06	6.76e-01
20	8.255	-5.08	0	-5.08	0.834	2.73e-01	1.88e-02	5.53e-01	2.79e-01	5.91e-03	7.81e-01
21	8.255	0	0	0	1.08	3.10e-01	4.47e-02	3.65e-01	2.83e-01	7.28e-03	8.39e-01
22	8.255	5.08	0	5.08	1.02	2.20e-01	1.05e-02	-2.05e-01	2.44e-01	1.72e-03	6.57e-01
23	8.89	6.0452	0.635	6.0452	1.12	2.32e-01	1.16e-02	-5.54e-02	2.45e-01	3.60e-04	6.75e-01
24	10.6172	6.0452	2.3622	6.0452	1.18	2.79e-01	1.69e-02	8.05e-01	3.92e-01	2.06e-02	9.62e-01
25	11.7856	-5.08	3.5306	-5.08	0.632	2.84e-01	2.29e-02	5.71e-01	2.57e-01	8.73e-03	7.66e-01
26	11.7856	0	3.5306	0	1.23	2.46e-01	2.61e-02	4.51e-01	2.19e-01	4.64e-03	6.59e-01
27	11.7856	5.08	3.5306	5.08	1.2	2.43e-01	1.03e-02	5.09e-01	3.38e-01	5.15e-03	8.33e-01
28	12.3698	6.0452	4.1148	6.0452	0.95	2.44e-01	1.11e-02	1.50e-01	1.87e-01	7.45e-04	6.15e-01
29	15.2908	-5.08	7.0358	-5.08	0.591	2.42e-01	2.42e-02	4.33e-01	2.28e-01	4.73e-03	6.65e-01
30	15.2908	0	7.0358	0	1.01	2.41e-01	2.48e-02	3.63e-01	2.21e-01	3.38e-03	6.54e-01
31	15.2908	5.08	7.0358	5.08	1.11	2.53e-01	1.20e-02	3.03e-01	2.44e-01	3.22e-03	7.03e-01

APPENDIX D

PARTICLE MEAN AND RMS VELOCITY MAPS

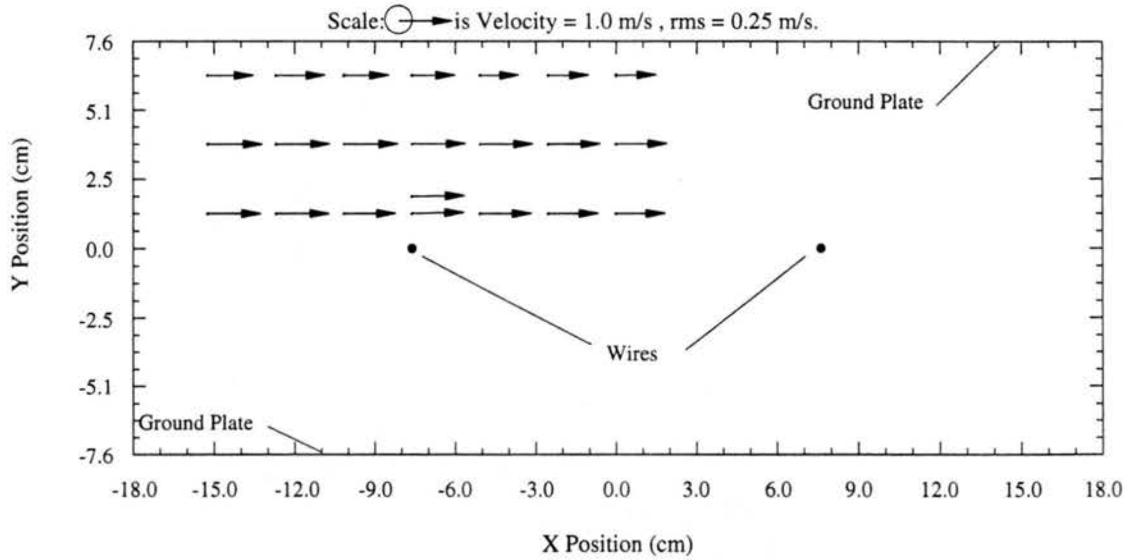

Figure D.1. Particle velocity and RMS magnitude map for the wire-plate precipitator at $N_{EHD} = 0$.

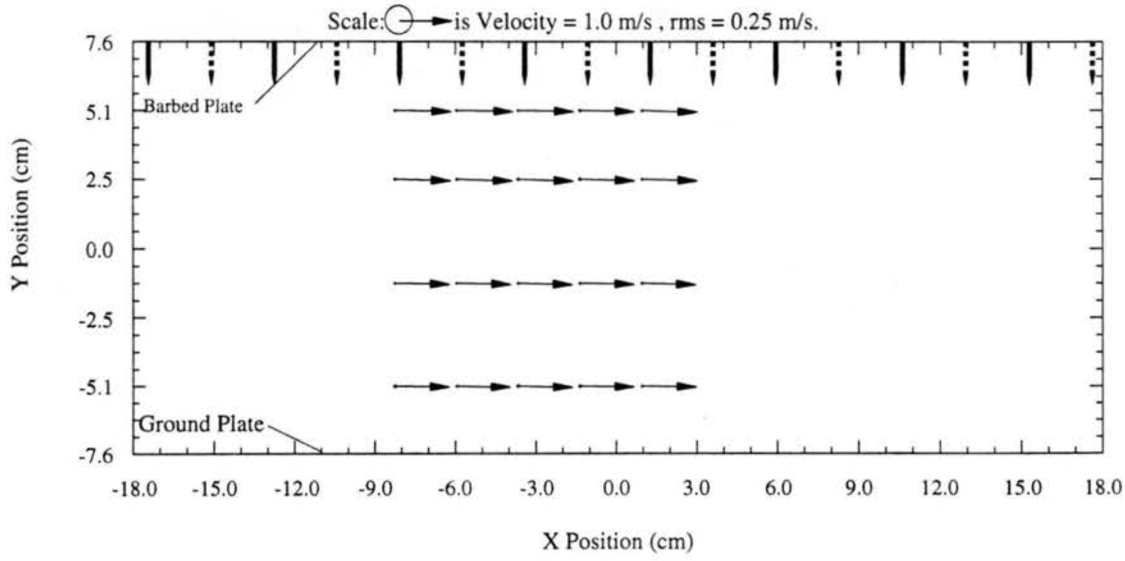

Figure D.2. Particle velocity and RMS magnitude map for the barbed plate precipitator at $N_{EHD} = 0$.

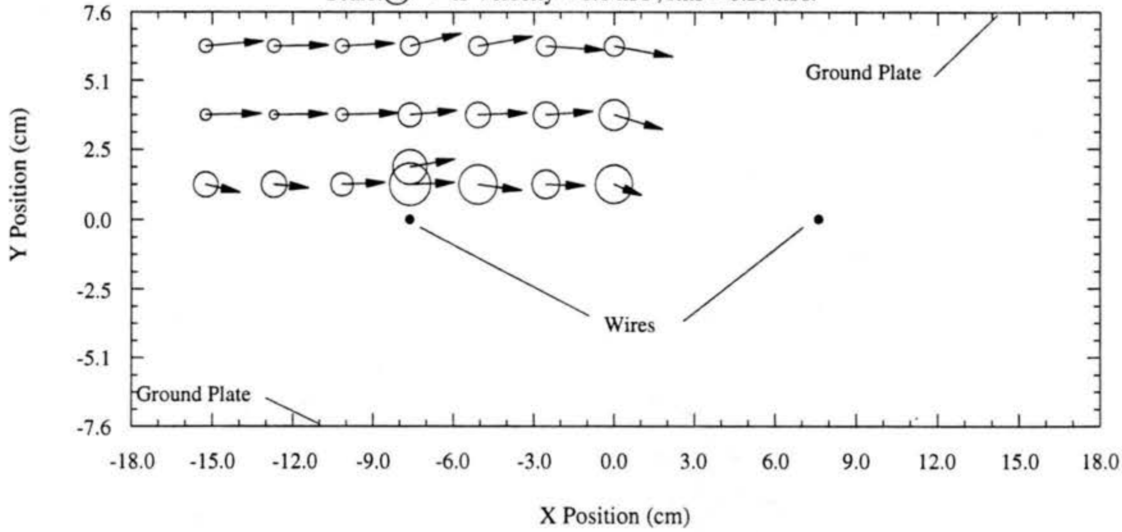

Figure D.3. Particle velocity and RMS magnitude map for the wire-plate precipitator at $N_{EHD} = 1$.

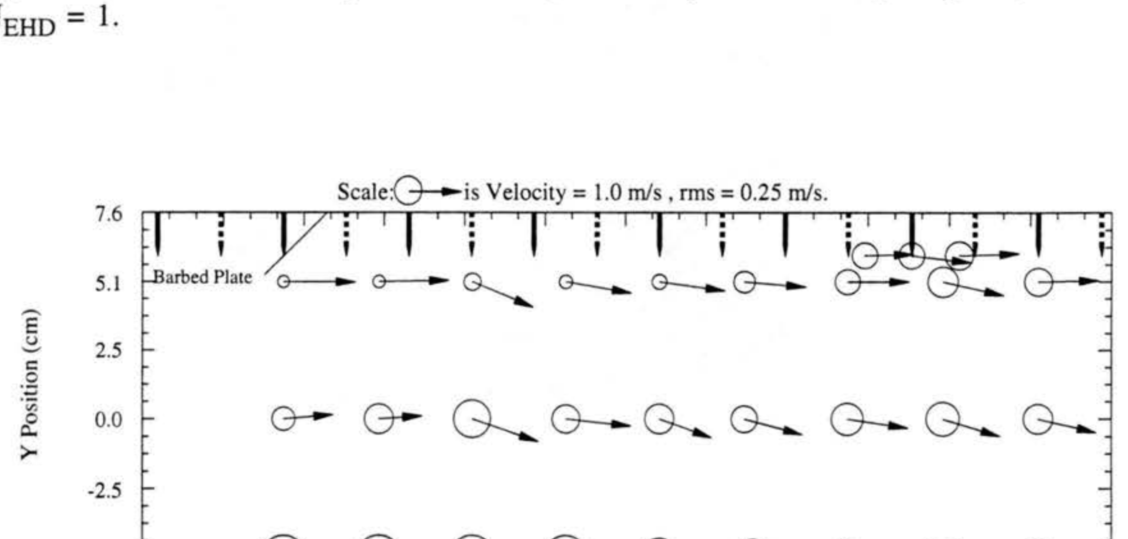

Figure D.4. Particle velocity and RMS magnitude map for the barbed plate precipitator at $N_{EHD} = 1$.

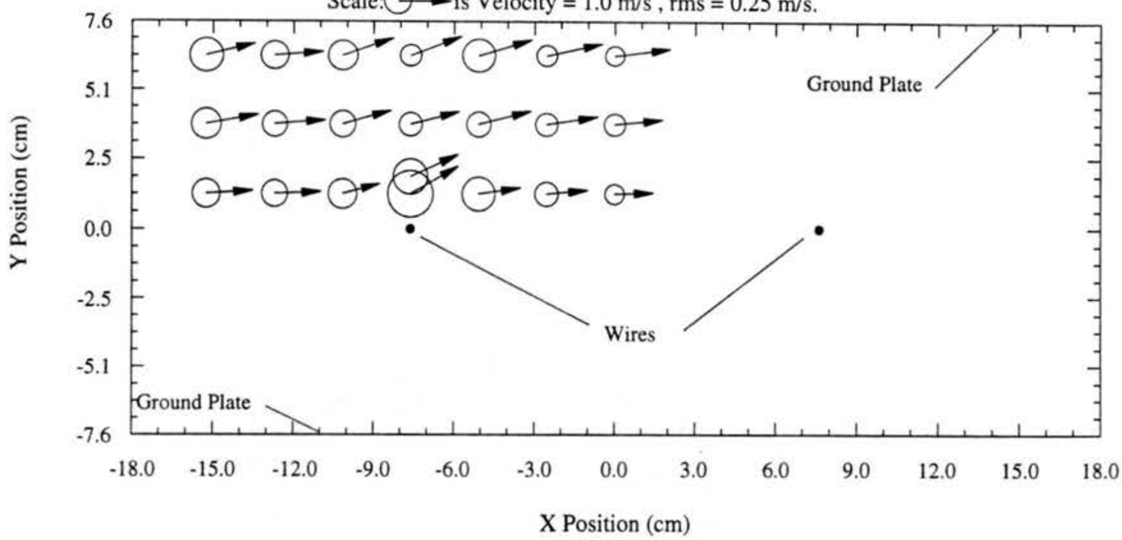

Figure D.5. Particle velocity and RMS magnitude map for the wire-plate precipitator at $N_{EHD} = 2$.

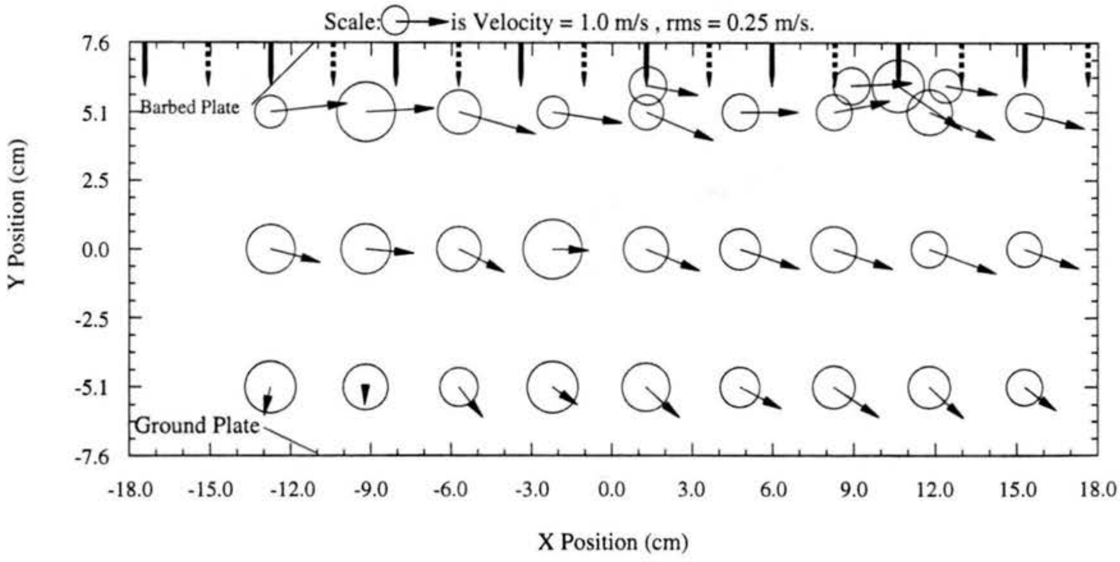

Figure D.6. Particle velocity and RMS magnitude map for the barbed plate precipitator at $N_{EHD} = 2$.

APPENDIX E

PARTICLE VELOCITY INTEGRAL LENGTH SCALES

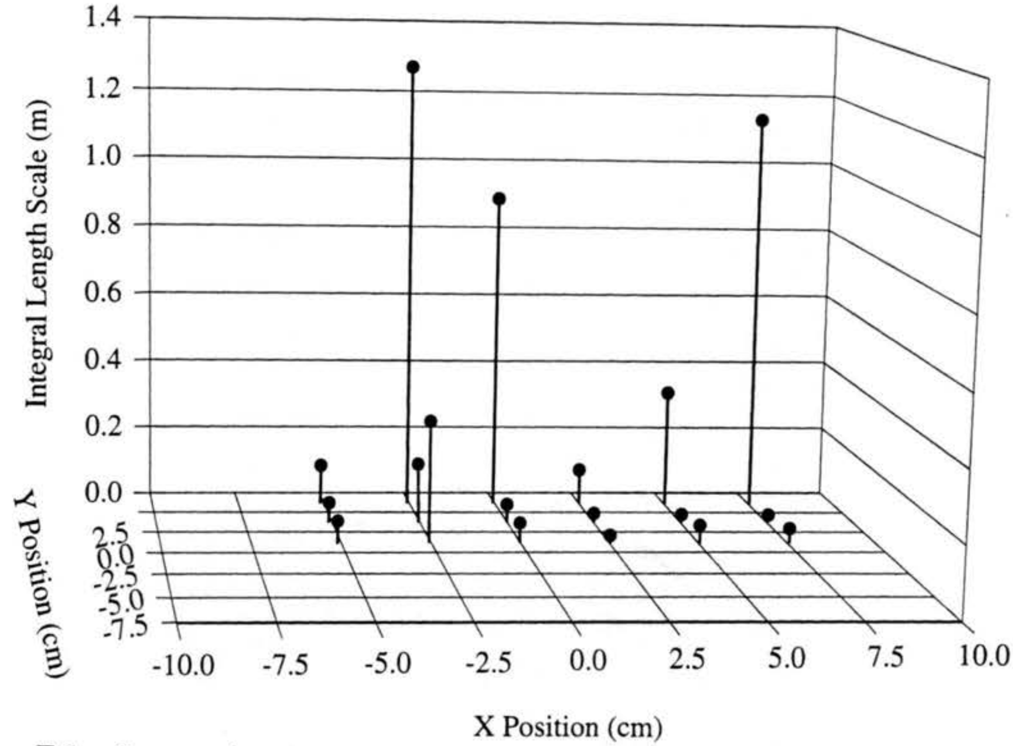

Figure E.1. Streamwise integral length scales for the wire-plate precipitator at $N_{EHD} = 0$.

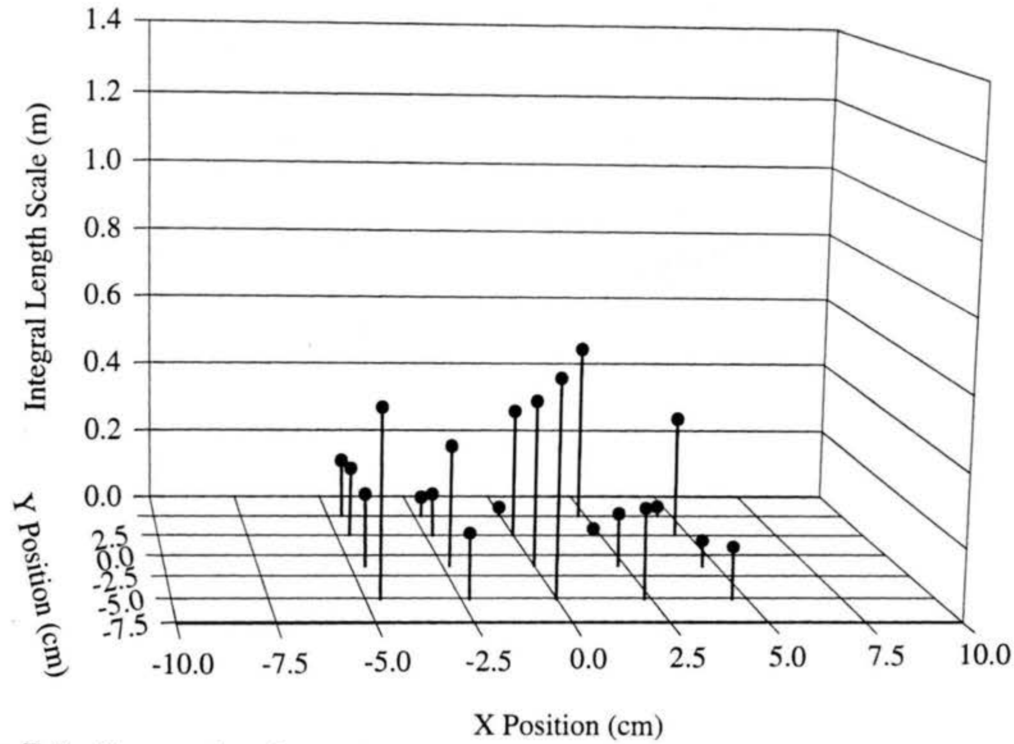

Figure E.2. Streamwise integral length scales for the barbed plate precipitator at $N_{EHD} = 0$.

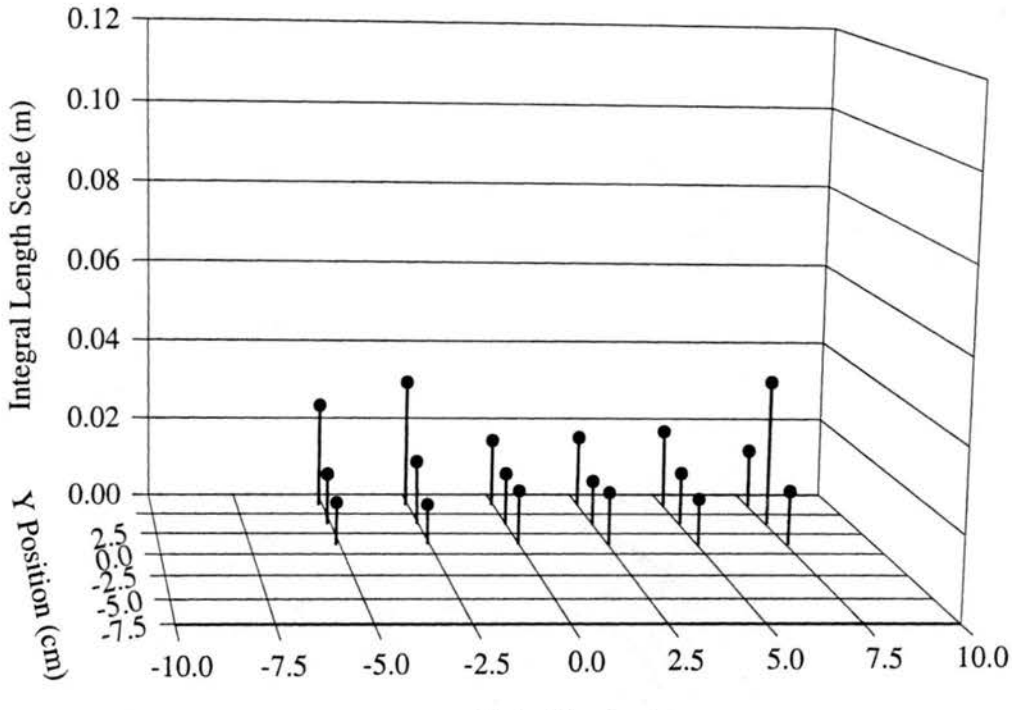

Figure E.3. Streamwise integral length scale for the wire-plate precipitator at $N_{EHD} = 1$.

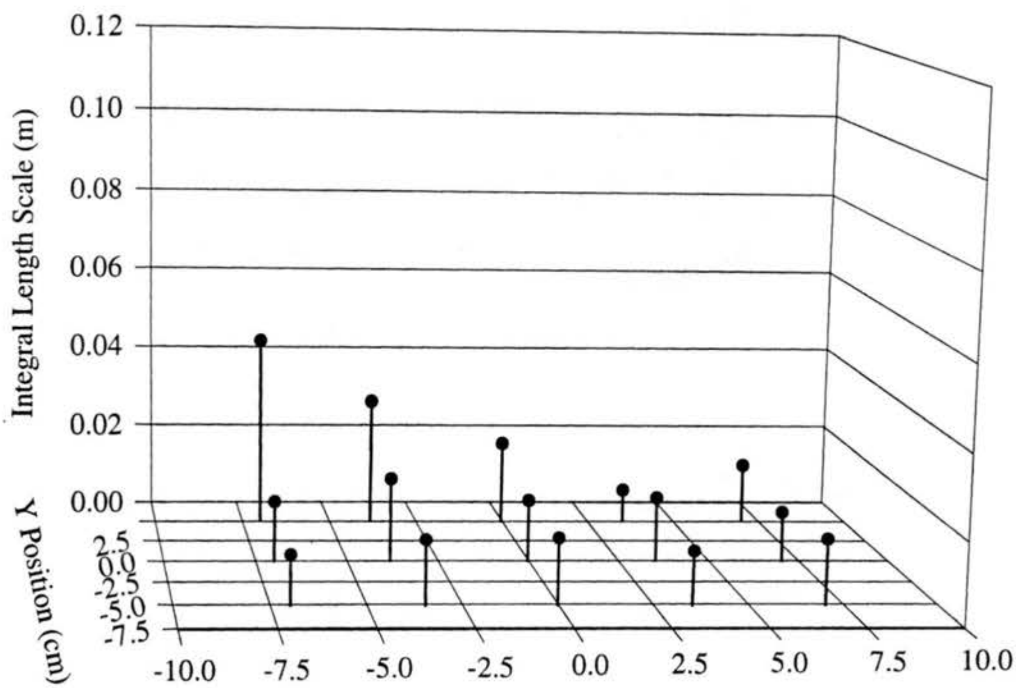

Figure E.4. Streamwise integral length scale for the barbed plate precipitator at $N_{EHD} = 1$.

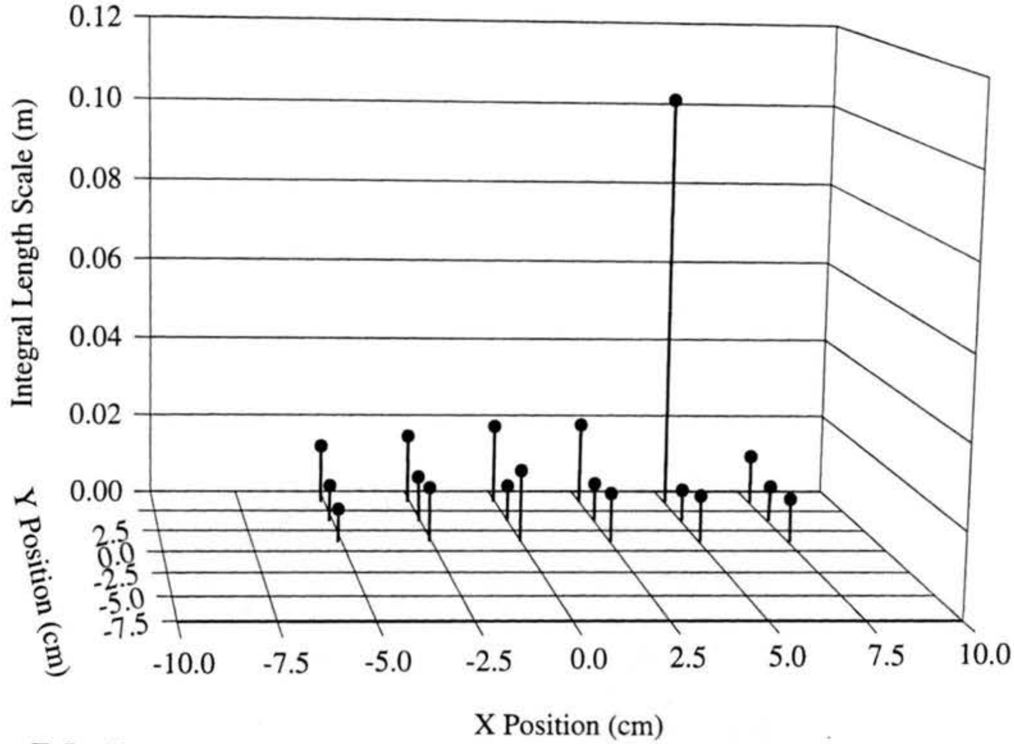

Figure E.5. Streamwise integral length scale for the wire-plate precipitator at $N_{EHD} = 2$.

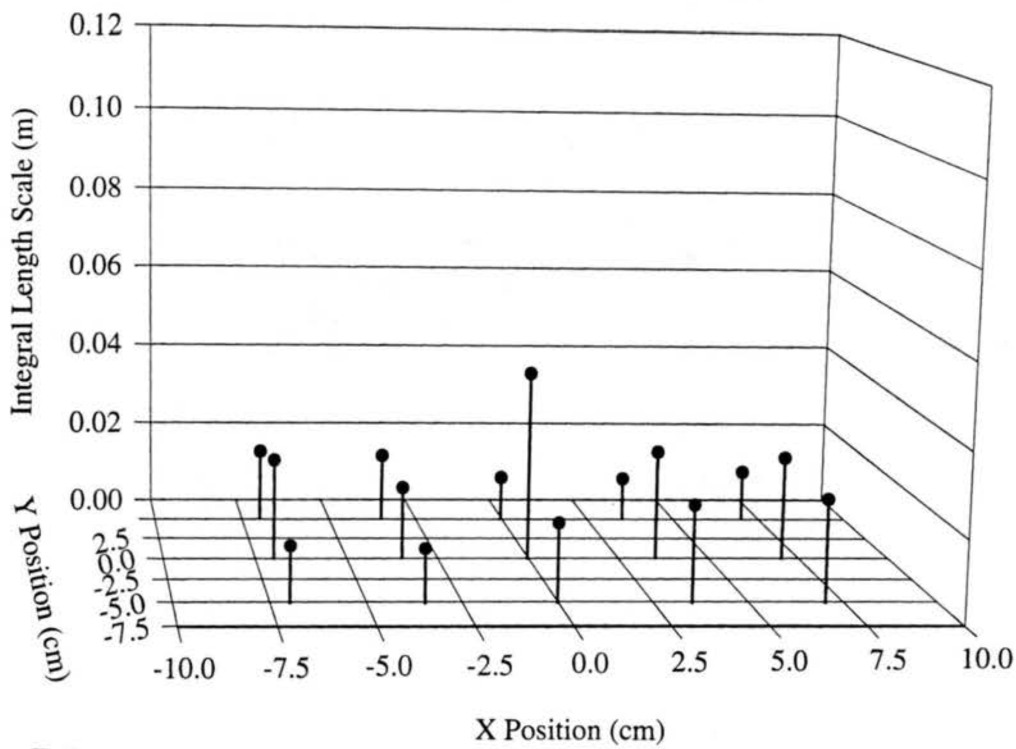

Figure E.6. Streamwise integral length scale for the barbed plate precipitator at $N_{EHD} = 2$.

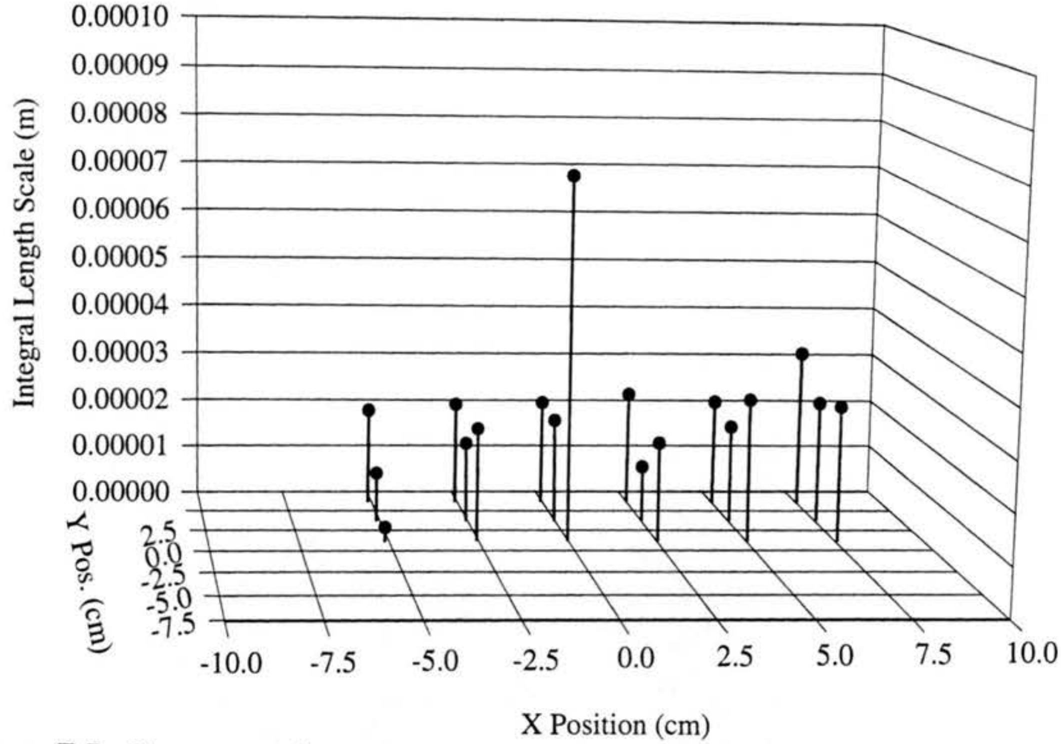

Figure E.7. Transverse integral length scales for the wire-plate precipitator at $N_{EHD} = 0$.

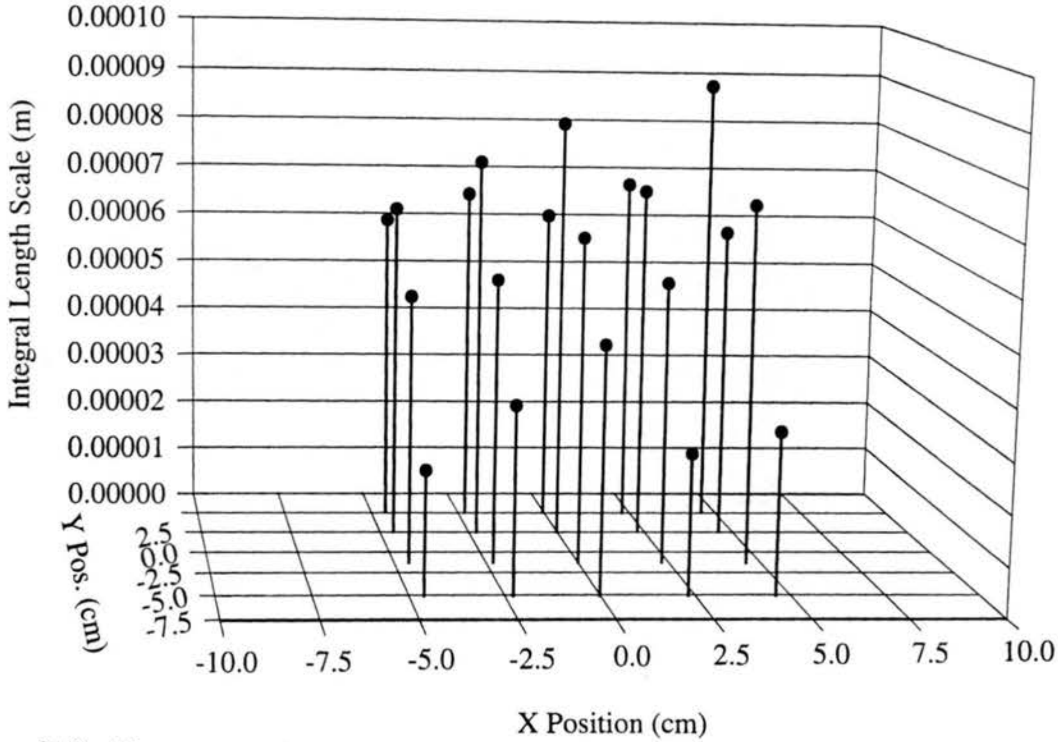

Figure E.8. Transverse integral length scales for the barbed plate precipitator at $N_{EHD} = 0$.

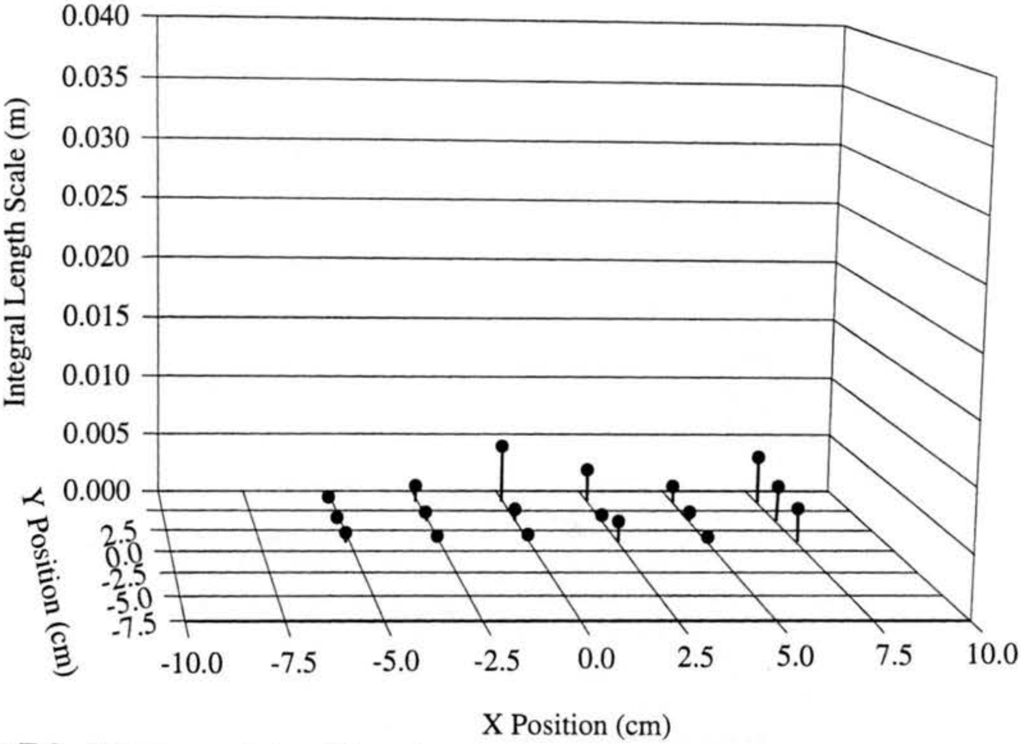

Figure E.9. Transverse integral length scale for the wire-plate precipitator at $N_{EHD} = 1$.

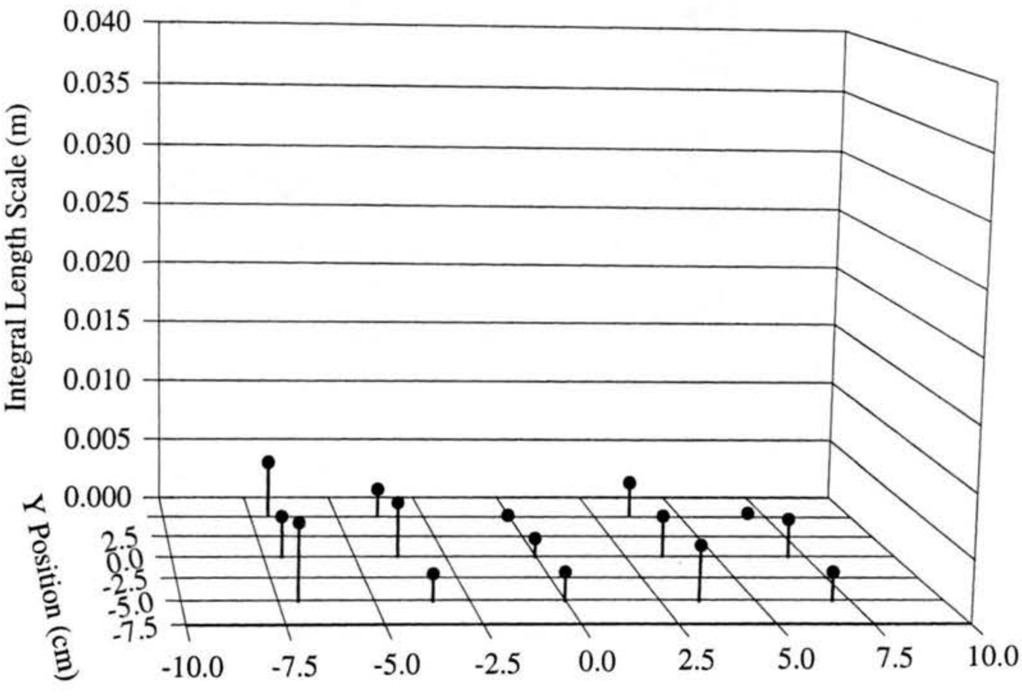

Figure E.10. Transverse integral length scale for the barbed plate precipitator at $N_{EHD} = 1$.

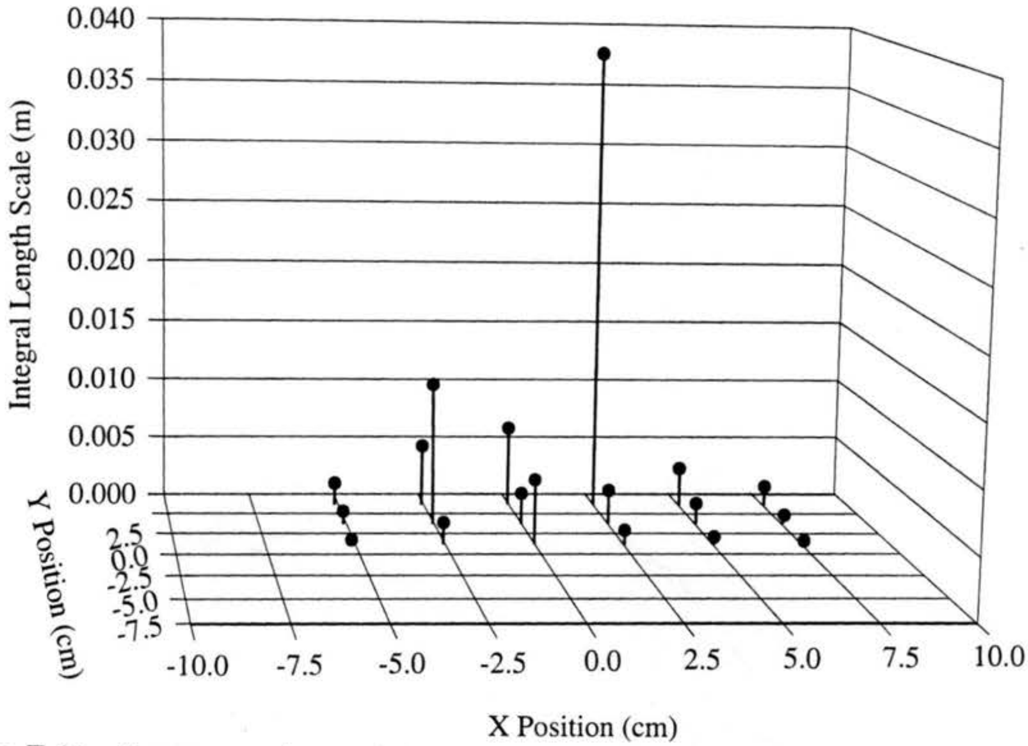

Figure E.11. Transverse integral length scale for the wire-plate precipitator at $N_{EHD} = 2$.

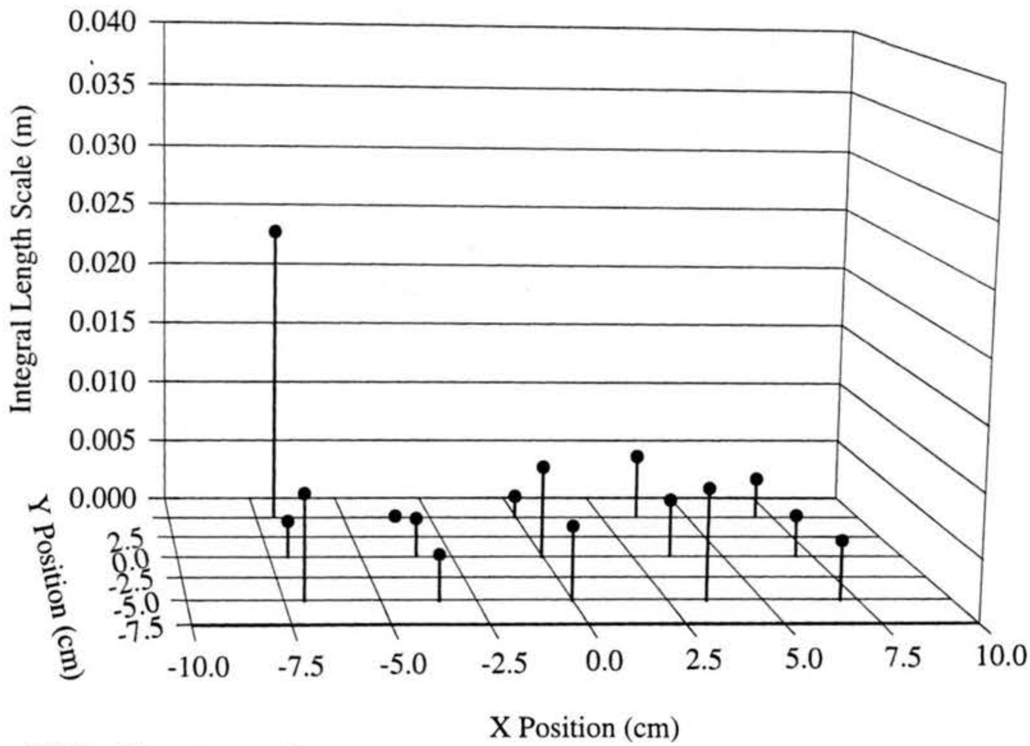

Figure E.12. Transverse integral length scale for the barbed plate precipitator at $N_{EHD} = 2$.

APPENDIX F

MEASUREMENT UNCERTAINTY ESTIMATES

Presented in this appendix are uncertainty estimates for current density and velocity measurements. Precision (random) and bias errors are reported separately because any bias error is consistent throughout all measurements and can be safely ignored when comparing measurements in this text only. The major source of uncertainty in both current density and particle velocity measurements is process unsteadiness. Unsteadiness in both measurements is attributed to corona current density unsteadiness.

The bias error for current density measurements in the wind tunnel (Figures 4.33 through 4.36 and Table 4.4) is estimated to be ±1% of reading and is a function of the ammeter accuracy. Precision error for the same measurements is estimated by computing the rms of the differences in two data sets taken under the same condition. This technique incorporates all precision uncertainties, both due to the process and the instrumentation. The final error estimate is computed as two times the rms of the difference in the data sets and is ±11% for current densities at $N_{EHD} = 1$ and ±8% for current densities at $N_{EHD} = 2$.

The bias error for current density measurements made on the *X-Y* Traverse (Figures 4.1 through 4.28 and Tables 4.1 and 4.3) is estimated to be ±1% and is a function of the accuracies of the picoammeter used for measurements and the microammeter used to calibrate the probe area. Since measurements on the *X-Y* Traverse are made under the same conditions as measurements made in the wind tunnel, the precision uncertainty is assumed to be the same at worst. In reality, measurements made directly under a corona tuft or barb tip are much more accurate than the measurements made in the wind tunnel because the corona is very stable in those regions. Current density is very unstable near the edge of a tuft or barb corona distribution because the distribution shifts slightly about a mean position. The estimate of precision error for X-Y Traverse measurements made directly under a barb or tuft is ±1%. The error in areas with no current at all is assumed to be ±1% as well.

The bias error for particle velocity measurements is a function of laser beam crossing angle, and fringe crossing time. The fringe crossing time is output in volts by the LDA timer digital-to-analog converter and read in by the computer analog-to-digital converter. All other parameters in equation 3.9 have negligible error in comparison to the above. The bias uncertainty is estimated as ±0.05 m/s and is reported in m/s because the value is constant for all velocities in the measurement range.

The precision uncertainty is estimated statistically by obtaining a series of measurements at the same location and conditions. The time series plotted in Figures 4.47 through 4.50 are divided into 92-second long segments and the mean and rms velocities are computed for each segment. The 95% confidence limit is calculated for each set of mean and rms values. The 95% confidence limit is taken to be the total precision uncertainty, encompassing both instrument precision and process unsteadiness errors. The precision uncertainty estimates for the streamwise flow direction are ±9% for the mean velocity and ±5% for the rms velocity. The respective values for the transverse flow direction are ±5% and ±3%. Estimates for the turbulence intensity precision uncertainty is computed from the mean and rms uncertainties using the propagation equation of Kline and McClintock (1953) and is ±8%.

The rms errors are calculated and reported separately from the mean errors because the process unsteadiness occurs on a fairly long time scale (1 minute or more) and the rms is fairly independent of that unsteadiness. It must also be pointed out that the reported error estimates are for the "worst case" flow condition (the barbed plate operating at $N_{EHD} = 2$) and therefore are extremely conservative for all other conditions. Although no repeated series of data were taken for conditions other than $N_{EHD} = 0$, observations of statistical values as the data was collected indicate that the uncertainty estimates for particle velocities at $N_{EHD} = 1$ may be half of the estimates reported above. The $N_{EHD} = 0$ condition is very stable and the precision error may be lower still.